
AMORPHOUS 200nm AND 2 μ m THICK Ga_xSb_{100-x} PHASE-CHANGE FILMS

A THESIS ON THE FABRICATION OF Ga_xSb_{100-x} FILMS USING
ELECTRONBEAM EVAPORATION,
THE ISOTHERMAL CRYSTALLISATION PROCESS OF THE 200nm LAYERS
AND POTENTIAL EVALUATION OF THE 2 μ m THICK LAYER FOR RESEARCH
IN EXPLOSIVE CRYSTALLISATION

GRONINGEN, 2012–2013



AUTHOR: K.B.OVER (S1486799)

SUPERVISOR: PROF. DR. IR. B.J. KOOI

DAILY SUPERVISION: IR. G. EISING

Nanostructured Materials and Interfaces, University of Groningen



university of
 groningen

faculty of mathematics and
 natural sciences

zernike institute for
 advanced materials

Abstract

This report covers the production process of $\text{Ga}_x\text{Sb}_{100-x}$ layers on a glass substrate with various compositions and thicknesses using e-beam evaporation and the subsequent analysis of the crystallisation of these layers by isothermal annealing using the Arrhenius equation and JMAK theory. The kinetic properties of these layers are compared to results of isothermal annealing of layers of $\text{Ge}_x\text{Sb}_{100-x}$ layers obtained by Gert Eising. It will be shown that the composition of the deposited layer is not uniform during the deposition process, but depends on target composition, evaporation speed and target shape. Germanium is shown to have a stronger stabilising effect on the amorphous layer than Gallium. A relaxation effect in the $\text{Ga}_x\text{Sb}_{100-x}$ layers is observed, which causes the observed growth rate of the crystals to increase exponentially in time. Subsequent adjustment of the Avrami equation allows for a reasonably accurate description of the crystallisation process, with the indication that also the nucleation probability n is affected by the relaxation effect. The observed relaxation effect was only observed in layers that were deposited at a rate higher than 0.2 nm/s.

Contents

Introduction	1
1 Introduction	1
2 Theory	4
2.1 The Arrhenius equation	4
2.2 JMAK Theory	4
2.2.1 Relation between Germ Nuclei, Growth Nuclei and Transformed Matter	5
2.2.2 The concept of extended volume (V_{ex}).	7
2.2.3 The volume of an average crystal v in terms of the growth rate G and nucleus activation probability n in the isokinetic range.	8
2.2.4 An explicit function for the extended volume (V_{ex}) and its limit values	9
2.2.5 Relation between the crystal volume V and the extended volume (V_{ex})	10
2.2.6 Determination of kinetic constants using JMAK theory and the Arrhenius equation.	11
3 Experimental Setup & Procedures	12
3.1 Sample creation	12
3.1.1 Target Creation	12
3.1.2 Glass substrate preparation	13
3.1.3 E-beam evaporation	15
3.2 Sample preparation for experiments	15
3.2.1 Checking deposition structure with optical microscope	15
3.2.2 Checking thickness with DEKTAK	16
3.2.3 Checking deposition structure and composition	16
3.2.4 Cutting samples to have identical samples	16
3.3 Isothermal and electron irradiation crystallisation experiments	16
3.3.1 Isothermal crystallisation experiments	16

4	Production of $\text{Ga}_x\text{Sb}_{100-x}$ samples	18
4.1	Target and sample composition analysis using SEM and EDX	19
4.2	Limitations in the use of the Varian 3120 e-beam evaporator	22
4.3	Results of layer deposition using e-beam evaporation	23
4.3.1	The relation between target composition and layer composition.	24
4.3.2	The change of target composition during the evaporation process	25
4.3.3	The influence of layer deposition rate on layer composition.	31
4.3.4	Analysis of Gallium concentration drop during the deposition of the first few hundred nanometres.	32
4.3.5	Discussion of the remaining unresolved observations.	36
4.4	Considerations in the creation of useful samples for isothermal annealing experiments and explosive crystallisation.	39
4.4.1	Compositions useful for isothermal annealing experiments and explosive crystallisation	39
4.4.2	Recommendations for target creation	46
4.4.3	Samples analysed with isothermal experiments.	47
5	Isothermal Heating Experiments	48
5.1	Determination of kinetic constants based on Avrami's theory.	49
5.1.1	Determination of growth energy E_g and nucleation energy E_n	49
5.1.2	A comparison with $\text{Ge}_x\text{Sb}_{100-x}$ samples	52
5.1.3	A comparison with Avrami theory	56
6	Exponential increase in growth rate	63
6.1	Growth rate dependency on crystal size and absolute time	64
6.1.1	Average directional symmetry of growth rate	66
6.1.2	Crystal growth rate invariance of location	71
6.1.3	Crystal size dependence or time dependence	72
6.1.4	Exponential increase in growth rate with respect to time	73
6.2	The influence of latent heat and/or layer relaxation on growth rate	75
6.3	Avrami Theory including relaxation effects	83
7	Discussion	92
7.1	Sample preparation	92
7.2	Annealing experiments and relaxation	93
7.3	TEM experiments for crystal structure analysis and layer excitation	94

8	Conclusions	95
8.1	Sample preparation	95
8.2	Annealing experiments	95

Chapter 1

Introduction

Phase-change materials can exist in two solid phases, amorphous and crystalline. In general the amorphous phase has a higher electrical resistance and lower optical reflectivity, than the crystalline phase. In memory applications the difference in the properties between the two solid states can be used to identify the state of a bit as either 1 or 0.

It is possible to repeatedly switch between the two phases of the material. By adding energy to the amorphous phase, the bonds between the atoms will weaken, this allows the material to make the transition to the energetically favourable crystalline state. The crystalline phase can be converted back to the amorphous phase by means of melt-quenching [1].

Data transfer is limited by the speed at which the material can switch phases. The limiting factor in this process is the step from amorphous to crystalline, therefore the crystal growth rate and growth energy of a material are important factors to consider when investigating the suitability of a material in memory applications.

As was mentioned, above the glass transition and below the melting temperature, glass the crystalline state is a more energetically favourable state. This gives rise to another effect called explosive crystallisation. Normal crystallisation requires the continuous addition of energy from an external source in order to keep the transition process from stalling. During explosive crystallisation enough energy is released during crystallisation to create a chain reaction, where the energy released due to crystallisation is enough to also crystallise the amorphous material surrounding the growing crystals. [2]

One group of phase-change materials that is widely used in memory applications are the chalcogenide glasses. Chalcogenide glasses are chemical compounds consisting of at least one chalcogen ion and at least one more electropositive element. Chalcogenide glasses have found many applications in the semi-conductor industry because of their phase changing properties. One well established application is the use of chalcogenide glasses in rewritable, optical data storage disks, such as DVD and Blu-Ray. A relatively new

application is its use in electrical non-volatile Phase-Change Memory (PCM) [3]. This report will focus on thin films of two types of materials that lay outside the chalcogenide glasses group, namely thin films of GaSb and GeSb.

The research described in this report is meant to complement previous work done by Gert Eising, who had investigated the kinetic properties of films of $\text{Ge}_6\text{Sb}_{94}$, $\text{Ge}_7\text{Sb}_{93}$, $\text{Ge}_8\text{Sb}_{92}$ and $\text{Ge}_9\text{Sb}_{91}$ with various thickness's including 200nm. Gallium is in the same row as Germanium in the periodic table, one column to the left, and explosive crystallisation of GaSb and GeSb films has been observed in literature. [4] [5] [6] Previous work done on explosive crystallisation of GeSb and GaSb had been done by measuring the change of the resistivity of the material. [5] Our goal was to record this process by use of an optical high speed camera. According to literature the typical thickness of GaSb films used to study explosive crystallisation was about $2.5\mu\text{m}$. [7]

This led to three initial goals for sample production. The first goal was to produce samples with compositions matching those of the $\text{Ge}_x\text{Sb}_{100-x}$ samples analysed by Gert Eising with a thickness of 200nm. By keeping the compositions similar to the films investigated by Gert Eising, there might be the possibility to compare the kinetic properties of both samples. The second goal was to produce samples with a thickness in excess of $2.5\mu\text{m}$ with a composition of $\text{Ga}_{50}\text{Sb}_{50}$ in conformance with experiments known from literature [5] [7]. The third goal was to create samples with a thickness in excess of $2.5\mu\text{m}$ with a composition of matching the $\text{Ge}_x\text{Sb}_{100-x}$ samples.

Electron beam (e-beam) evaporation was used to deposit amorphous layers of $\text{Ga}_x\text{Sb}_{100-x}$ and the composition was checked by means of Energy-dispersive X-ray spectroscopy (EDX) connected to a Scanning electron microscope (SEM). It proved difficult to control the composition of the deposited layer. The composition of the target used did not match the composition of the deposited layer. The composition of the target also changed over the duration of the evaporation process, thus the composition of the deposited layer was not uniform over its thickness and finally, the evaporation speed had an influence on the composition of the deposited layer. In order for the layer to be amorphous at room temperature, the Gallium content needed to be higher then 10.5%. Not only the target, but also the deposited layer is slowly heated during the e-beam evaporation process. Attempts to create thick amorphous layers proved to be succesfull, but the layer showed no explosive crystallisation properties. It was possible to create amorphous layers of $\text{Ga}_x\text{Sb}_{100-x}$ with a thickness of 200nm, where x ranged between 10 At% and about 50 At%.

Crystal growth rate measurements, and measurement of the ratio between crystallised material and amorphous material were performed on these samples using a high speed optical camera. To derive the kinetic properties of the material, Johnson-Mehl-Avrami-Kolmogorov (JMAK) theory was applied to these measurements. These experiments were performed at the

University of Groningen in the group of Nanostructured Materials and Interfaces (NMI).

The Arrhenius equation and JMAK theory for constant growth rate G and constant nucleation probability n is described in chapter 2. After description of the experimental setup and procedures in chapter 3, the results will be separated in three chapters. Chapter 4 is meant to give a complete overview of the sample production process, so that any reader with the intention to continue this research is able to avoid many pitfalls in the sample creation process. Results and discussion regarding the isothermal growth experiments will be presented in chapter 5. Chapter 5 will show that growth is not constant during the transition from the amorphous state to the crystalline state. The standard JMAK equation described in chapter 2 are not able to accurately describe the transformation process from amorphous to crystalline. Chapter 6 will show that growth rate increases exponentially in time due to a relaxation effect, and the JMAK equations will be altered to incorporate this exponential increase in growth rate. The adjusted JMAK equation is able to describe the amorphous to crystalline transformation process much more accurately, and seems to indicate that not only growth rate G , but also nucleation probability n is not constant with time. Chapter 7 further discusses the combined results obtained in the three previous chapters and gives some recommendations on how the research presented in the report might be extended. The main conclusions of the report are summarised in chapter 8.

Chapter 2

Theory

This chapter will consist of two parts, the Arrhenius equation and Johnson-Mehl-Avrami-Kolmogorov (JMAK) theory. Both will be used to analyse the isothermal growth experiments presented in chapter 5.

2.1 The Arrhenius equation

The most simple form of the Arrhenius equation is:

$$k = Ae^{-E_a/k_B T} \quad (2.1)$$

which represents: 'The dependence of the rate constant k of chemical reactions on the temperature T (in absolute temperature Kelvin) and activation energy E_a ' [8].

This means that in equation 2.1: k is the number collisions that result in a reaction per second, A is the total number of collisions and $e^{-E_a/k_B T}$ is the probability that any given collision will result in a reaction. The probability that any given collision will result in a reaction $e^{-E_a/k_B T}$ is composed of the activation energy E_a , the Boltzmann constant k_B and the temperature T in Kelvin.

In the case of phase-change reactions, the Arrhenius equation can be used to model crystal growth. In this case the growth rate is the result of atoms jumping across the amorphous crystalline border at the edge of an existing crystal and every jumping atom has a probability to become part of the crystal structure, leading to crystal growth. This is based on an interpretation of the description of grain growth described in [9]

2.2 JMAK Theory

The majority of this section is based on two articles written in 1939 and 1940 by Avrami [10][11]. It will follow the line of these two articles, but

explicit derivation of formula's will be done with the assumption of plate like growth, whereas the articles of Avrami mentions three dimensional growth and generalises the theory for volume growth, plate like growth and linear growth.

First the concept of germ and growth nuclei is introduced and their relation with the transformed volume V is determined. Then the concept of extended volume V_{ex} is introduced. Then an explicit function of the relation between the transformed volume and the kinetic properties of the material is derived. Finally it is shown how to use this relationship to determine the kinetic properties from measurement results.

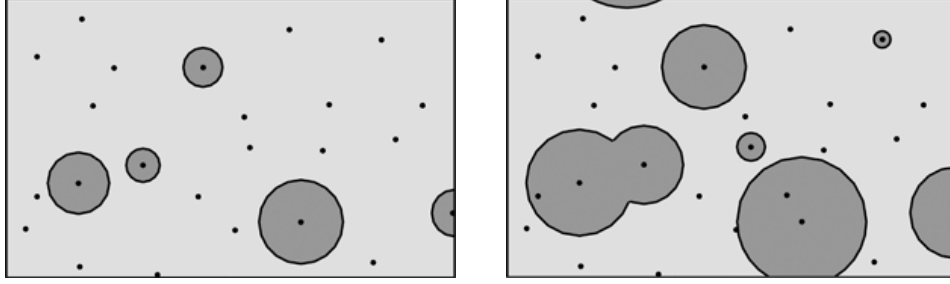
2.2.1 Relation between Germ Nuclei, Growth Nuclei and Transformed Matter

JMAK theory describes the transition of one solid phase to another. It assumes that the new phase starts to grow from random points on the sample, it is thus nucleation based. These points where the new phase starts to grow are predetermined and randomly distributed. These predetermined points are called germ nuclei. If the new phase starts to grow from one of these germ nuclei, it has become an activated germ nucleus, called a growth nucleus. Thus JMAK theory describes the transition from one solid phase to another in the case of a nucleation based transition with germ nuclei.

One example of this is the transition of a thin layer of amorphous phase-change material to a crystalline phase due to annealing. Before the transformation process has started, there exists an amorphous layer with germ nuclei, which are a result of the preparation process of the amorphous layer. When the layer is annealed there is a probability that a germ nuclei will become a growth nuclei and thus that from that point a crystal will start to grow. During the crystallisation process multiple crystals will start to grow. The growing crystals will block each others growth when they impinge each other, and swallow germ nuclei that have not been activated yet. Eventually the entire layer will be covered in crystals.

The amount of germ nuclei present in the material can decrease in two ways: firstly germ nuclei can become activated growth nuclei and secondly germ nuclei can be swallowed by the growing crystals, once a germ nuclei has been swallowed by a growing crystal it can no longer be activated, see Figure 2.1.

Let \bar{N} be the amount of germ nuclei per unit volume, distributed in any manner. Let $N \equiv N(t)$ be the amount of germ nuclei per unit volume at time t . $N \equiv N(t)$ will decrease from \bar{N} by activation of germ nuclei into growth nuclei and swallowing of germ nuclei by growing crystals as time t is increased. Let $N' \equiv N'(t)$ be the amount of growth nuclei at time t per unit volume. Let $N'' \equiv N''(t)$ be the amount of germ nuclei per unit volume that have been swallowed at time t , see Equation 2.2



(a) An amorphous layer with circular crystals and germ nuclei at time t_a .

(b) An amorphous layer with circular crystals and germ nuclei at time t_b .

Figure 2.1: Figures 2.1a and 2.1b depict the transition of an amorphous layer with germ nuclei into a crystalline layer at times t_a and t_b , where $t_a < t_b$. Figure 2.1a: various germ nuclei have transformed into growth nuclei and crystals have started to grow. Figure 2.1b: crystals present in 2.1a have grown, more germ nuclei have transformed into growth nuclei creating more crystals, crystals have impinged on each other, and germ nuclei have been swallowed by the growing crystals.

$$N(t) = \bar{N} - N'(t) - N''(t) \quad (2.2)$$

The average amount of germ nuclei that will be activated at time t to form growth nuclei per unit volume can be represented by $nN(t)$, where $n \equiv n(T)$ is the probability of formation of growth nuclei per germ nucleus per unit time, which will have the general form:

$$n(T) = Ke^{(-Q+A(T))/(k_B T)}, \quad (2.3)$$

where, Q is the activation energy in electron volt (eV), $A(T)$ is the work required for forming a growth nucleus at temperature T , k_B is the Boltzmann constant, and K is a constant independent of temperature.

Since $N \equiv N(t)$ is the amount of germ nuclei per unit volume available for activation at time t , the density of germ nuclei encountered, on average by the growing crystal front is $N/(1 - V)$, where $1 - V$ is the fraction of untransformed volume per unit volume. Let dN be the variation of N over a short time interval dt , dN can be described as:

$$dN = -dN' - dN'', \quad (2.4)$$

where

$$dN' = nNdt, \quad (2.5)$$

and

$$dN'' = \frac{N}{1 - V}dV, \quad (2.6)$$

, where dV is the increase in crystal volume per unit volume per unit time dt . For further analysis it is convenient to write these expressions in a different

unit of time, the characteristic time τ , which is defined as $\tau = nt$. By substituting equation 2.5 and 2.6 into equation 2.4, then using substitution of variables,

$$ndt = d\tau \quad N(t) \rightarrow N(\tau) \quad V(t) \rightarrow V(\tau), \quad (2.7)$$

and integrating over the result, equation 2.4 transforms into,

$$N(\tau) = \bar{N} e^{-\tau(1-V(\tau))} \quad (2.8)$$

which represents the density of germ nuclei over characteristic time τ . This means that the density of growth nuclei $N'(\tau)$ as a function of characteristic time τ becomes,

$$N'(\tau) = \bar{N} \int_0^\tau e^{-z(1-V(z))} dz \quad (2.9)$$

2.2.2 The concept of extended volume (V_{ex}).

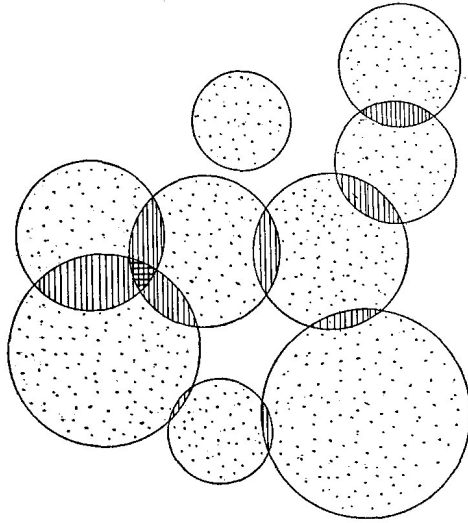


Figure 2.2: A group of spherical overlapping crystals. V_τ is the total crystal volume. Let V'_1 be the sum of the dotted areas, V'_2 the sum of the singly hatched areas, and so on. Figure adopted from [10].

overlap each other. From this reasoning the following relations can be derived.

$$V_{1\ ex} = V'_1 + 2V'_2 + \dots + mV'_m + \dots, \quad (2.10)$$

$$V_1 = V'_1 + V'_2 + \dots + V'_m + \dots \quad (2.11)$$

During the crystallisation process of an amorphous layer, crystals start to impinge on each other, blocking each other's growth. The pattern the crystals of the new phase create can be viewed as collection of overlapping crystals. Figure 2.2 depicts a group of spherical crystals which have impinged on each other. The crystals are drawn as had their growth not been impeded, with the overlapping parts indicated by the singly hatched and doubly hatched areas.

The transformed volume $V(\tau)$, will be represented by adding all the crystal volumes, where the overlapping regions are only counted once $V(\tau) \equiv V_1$. Let V'_1 denote the total transformed volume, where only the non-overlapping parts are added. Let V'_2 then denote the parts of the volume where only two crystals

The general relations for V_k and $V_{k \text{ } ex}$ are

$$V_{k \text{ } ex} = \sum_{m=k}^{\infty} \binom{m}{k} V'_m \quad (2.12)$$

$$V_k = \sum_{m=k}^{\infty} V'_m \quad (2.13)$$

This means that the relation between V_1 and $V_{k \text{ } ex}$ will be

$$V_1 = \sum_{k=1}^{\infty} ((-1)^{k+1}) V_{k \text{ } ex} = \sum_{k=1}^{\infty} ((-1)^{k+1}) \sum_{m=k}^{\infty} \binom{m}{k} V'_m \quad (2.14)$$

and therefore

$$V_{\tau} \equiv V_1 = V_{1 \text{ } ex} - V_{1 \text{ } ex} + V_{1 \text{ } ex} - \dots + (-1)^{m+1} V_{m \text{ } ex} + \dots, \quad (2.15)$$

A more explicit relation between V_1 and $V_{1 \text{ } ex}$ will be derived in section 2.2.5

The extended volume V_{ex} can also be seen in terms of $N(t)$. Let v be the volume of a single crystal, then the extended volume of this crystal v_{ex} , is the volume of the crystal had its growth been unimpeded. Let the volume at time τ of any crystal which began to grow at time z be $v(\tau, z)$. The number of crystals per unit volume that started to grow at time z is given by $N(z)$. Thus the total extended volume per unit volume at time τ , which is the total transformed volume if we neglect overlapping of growing grains, is

$$V_{1 \text{ } ex} = \int_0^{\tau} v(\tau, z) N(z) dz. \quad (2.16)$$

The extended volume $V_{1 \text{ } ex}$ cannot be directly measured, therefore to find the relation between the kinetic constants and total transformed volume $V(\tau)$, it is necessary to find the relation between the extended volume $V_{1 \text{ } ex}$ and the actual transformed volume V_{τ} .

2.2.3 The volume of an average crystal v in terms of the growth rate G and nucleus activation probability n in the isokinetic range.

Let G be the average growth rate of a crystal, then the average radius r at ordinary time t of a crystal which started to grow at ordinary time y will be

$$r(t, y) = \int_y^t G(x) dx, \quad (2.17)$$

then if one applies substitution of variables with characteristic time

$$\begin{aligned} ndx = du, \quad \tau = \int_0^t n(x) dx, \quad z = \int_0^y n(x) dx, \\ G(x) \rightarrow G(u), \quad r(t, y) \rightarrow r(\tau, z), \end{aligned} \quad (2.18)$$

the relation for the average radius of a crystal in characteristic time will be

$$r(\tau, z) = \int_z^\tau \frac{G}{n} du \equiv \int_z^\tau \alpha du \quad (2.19)$$

Avrami [10] notes several articles where for a certain temperature range, both n and G are constant if the temperature remains constant and vary in the same manner with varying temperature. This temperature range is defined as the isokinetic range. In the description of the kinetic properties of the material it is therefore assumed that an isokinetic range exists where $G/n \equiv \alpha$ is a constant. where this relation has been worked out. This means that equation 2.19 can be written as

$$r(\tau, z) = \alpha(\tau - z) \quad (2.20)$$

The volume of plate like crystal $v(\tau, z)$ at characteristic time τ which has begun to grow at characteristic time z will then be

$$v(\tau, z) = \sigma\alpha^2(\tau - z)^2 \quad (2.21)$$

where σ is a shape factor in the case of circular crystals this would be $\sigma = \pi$.

2.2.4 An explicit function for the extended volume (V_{ex}) and its limit values

JMAK theory works for a complete random distribution of nuclei, with complete random activation of germ nuclei. However, equation 2.8 is not completely random, because nucleation will only happen outside the crystal volume. To make sure nucleation is random, the fact that part of the unit volume has been crystallised has to be ignored. In this case the rate of nucleation in characteristic time $N(\tau)$ can be written as

$$N(\tau) = \bar{N}e^{-\tau} \quad (2.22)$$

This assumption leads to the appearance of extra crystals called phantom crystals. Phantom crystals are the crystals that appear in the area which has already been crystallised, thus they will have an influence on $V_{1\ ex}$, but not on $V(\tau)$. These phantom crystals are not a physical reality, but a mathematical construct. Using equations 2.16, 2.21 and, 2.22 and integration by parts, the following explicit function for the extended volume $V_{1\ ex}$ is derived:

$$\begin{aligned} V_{1\ ex} &= \bar{N}\sigma\alpha^2 \int_0^\tau (\tau - z)^2 e^{-z} dz \\ &= -2\bar{N}\sigma\alpha^2 \left[e^{-\tau} - 1 + \tau - \frac{\tau^2}{2!} \right] \end{aligned} \quad (2.23)$$

For very large n $e^{-\tau}$ quickly goes to zero and equation 2.23 can be approximated by

$$V_{1\ ex} = -2\bar{N}\sigma\alpha^2 \left[-\frac{\tau^2}{2!} \right] = \bar{N}\sigma G^2 t^2 \quad (2.24)$$

For small values of τ , by taking the Taylor expansion of $e^{-\tau}$ equation 2.23 can be approximated by

$$V_{1\ ex} = -2\bar{N}\sigma\alpha^2 \left[-\frac{\tau^3}{3!} \right] = \frac{\bar{N}\sigma G^2 n t^3}{3} \quad (2.25)$$

If the transformation has been completed for small value of τ , τ is small compared to $\frac{1}{n}$, and the transformation is growth dominated.

These functions derived above for $V_{1\ ex}$, in combination with the relation of $V_{1\ ex}$ and V can be used to determine the kinetics of the transformation of an amorphous layer to a crystalline layer.

2.2.5 Relation between the crystal volume V and the extended volume (V_{ex})

In his paper Avrami gave a very general mathematical relationship between the transformed volume V_τ and the extended volume V_{ex} . This is not necessary in this report and therefore, from now on the extended volume will be defined as $V_{1\ ex} = V_{ex}$ and the transformed volume will be defined as $V_\tau = V$. Based on a random distribution of germ nuclei, with random activation, Avrami derived the following relationship between an increment of crystallised volume dV and an increment of extended crystalline volume dV_{ex} [11]:

$$\frac{dV}{dV_{ex}} = 1 - V \quad (2.26)$$

Integrating and rearranging this gives

$$V = 1 - e^{-V_{ex}} \quad (2.27)$$

Using equations 2.23, 2.24 and, 2.25, the general relationship between the transformed volume V and the kinetic properties of the material is given by

$$V = 1 - e^{2\bar{N}\sigma\alpha^2 \left[e^{-\tau} - 1 + \tau - \frac{\tau^2}{2!} \right]} \quad (2.28)$$

In the case of n is large

$$V = 1 - e^{-\bar{N}\sigma G^2 t^2} \quad (2.29)$$

and when τ is small compared to $\frac{1}{n}$

$$V = 1 - e^{-\frac{\bar{N}\sigma G^2 n t^3}{3}} \quad (2.30)$$

2.2.6 Determination of kinetic constants using JMAK theory and the Arrhenius equation.

When an amorphous layer is crystallised at temperature T , three things can be directly measured: the growth rate G , the total crystallised volume per unit volume V , and the nucleation rate nN .

To find all individual kinetic constants and to confirm that JMAK theory is applicable to our sample, the following approach is followed. First the growth rate G is measured and the growth energy E_g is derived using the Arrhenius equation. Then the probability of nucleation per unit volume n is derived by means of the incubation time. In the isokinetic range, it is assumed that the nucleation activation energy $E_n = (Q + A(T))$ is constant. From n it is possible to derive the nucleation activation energy E_n , using the same approach as in the case of the growth energy E_g and finally it is possible to derive the original density of germ nuclei per unit volume \bar{N} using the equation for the crystallised volume per unit volume V .

From the the Arrhenius equation 2.1 it follows that

$$\begin{aligned} G &= Ae^{-E_g/RT} \\ \Rightarrow \ln(G) &= \frac{-E_g}{RT} + \ln(A) \end{aligned} \quad (2.31)$$

where E_g is the growth energy required for crystallisation. A plot of $\ln(G)$ vs T^{-1} will give a straight line whose slope will be E_g

In the early stages of the transformation no crystals are visible. It will take a certain time for the first crystals to appear. This time is called the incubation time t_b . From equation 2.30: when $\tau \ll \frac{1}{n}$

$$\begin{aligned} V &= 1 - e^{-\frac{\bar{N}\sigma G^2 n t^3}{3}} \\ &\approx \frac{\bar{N}\sigma G^2 n t^3}{3} = \frac{\bar{N}\sigma \alpha^2}{3} \tau^3 \end{aligned} \quad (2.32)$$

This means that equation 2.32 will tend to increase rapidly when $\tau \geq 1$ or when $t \geq \frac{1}{n}$. Therefore

$$t_{Inc} \cong 1/n(T) \quad (2.33)$$

If the same approach as for the Arrhenius equation is used, the nucleation activation energy in the isokinetic range $E_n = (Q + A(T))$ can be derived using equation 2.3. A double logarithmic plot of $\ln(\ln(1 - V))$ vs $\ln(t)$ gives almost a straight line, whose slope can be used to find \bar{N} , gives information how well JMAK theory describes the transformation process, and whether it is growth dominated or nucleation dominated.

Chapter 3

Experimental Setup & Procedures

This chapter is dedicated to the experimental set-ups and procedures. There are two aims in using these set-ups. One is to create and analyse the crystallisation kinetics of amorphous $\text{Ga}_x\text{Sb}_{100-x}$ films with a thickness of 200nm deposited on a glass substrate, whose composition corresponds with the $\text{Ge}_x\text{Sb}_{100-x}$ samples analysed by Gert Eising. The other is to create amorphous layers of $\text{Ga}_x\text{Sb}_{100-x}$ with a thickness of 2 μm to record explosive crystallisation with a high speed camera. This chapter will only detail set-ups and procedures, thus it will only cover the way samples were created. The composition and thickness's of the samples which were created during the project are described in the Chapter 4. The motivation for creating targets and samples with compositions and thickness's mentioned in chapter 4 will also be covered in that chapter. This chapter itself consists of three main parts: the sample creation process, preparing samples before experimentation, and the experimental part.

3.1 Sample creation

3.1.1 Target Creation

The phase-change films were created using e-beam evaporation. During e-beam evaporation a target is evaporated in vacuum by means of an electron beam. To ensure a smooth evaporation process and to make sure the evaporated layer is as homogeneous as possible, it is important that the target is homogeneous as well. Our target was a mixture of Gallium and Antimony which had been melted in an oven before the e-beam evaporation process. To make sure the target mixture would not gain contaminants by reacting with the atmosphere, it was kept in a quartz vial under light vacuum when melted in the oven. The vial was made of quartz, since it does not react

with Gallium [12] and it can withstand the high temperatures necessary for melting the target mixture, while glass reacts lightly with Gallium and does not have the requisite melting temperature. The vapour pressure of Gallium and Antimony was not high enough to run the risk of cracking the quartz vial in the oven [13]. The structure of the target was checked with the use of a Philips XL30 Environmental SEM FEG, operated in high vacuum mode. The composition was investigated using energy-dispersive X-ray spectroscopy (EDX) by making use of an EDAX Apollo Silicon Drift Detector (SDD) with the Genesis Software Package.

Material mixing

Contamination of the sample with other substances, might have an influence on the crystallisation properties of the material mixture. It is therefore important that the materials used are as pure as possible. The following products were used: Alfa Aesar Gallium Metal with a purity of 99.999%, and Alfa Aesar Antimony Shots with a diameter of 6mm (0.2in) and down and a purity of 99.999%. The scale used to conduct weight measurements was a Mettler AE-160. The range in which the target composition had to lie could be determined with an accuracy of at least 0.01 At%.

Oven heating

The oven used to melt the target mixture in the quartz vial was a Navitherm Controller P320. The phase diagram of the Gallium Antimony System, see Figure 3.1, tells us that in order to be sure that the target mixture melts completely, it is necessary to raise the temperature of the mixture above 705.9°C. To reduce the risk that the quartz container breaks, due to tension build-up caused by a thermal gradient in the quartz between the inside and outside of the container, the temperature was slowly raised to 725°C. The precise oven settings can be found in Table 3.1.

When the temperature in the oven had lowered to 30°C, for targets with a Gallium concentration larger than 50At%, the target mixture had still not completely solidified. To solidify the target, the vial was cooled with running water. After the target had solidified it was removed from the vial by breaking the container wall.

3.1.2 Glass substrate preparation

Amorphous layers were deposited on 30mm × 30mm glass substrates, which have a rough side and a smooth side. The glass substrates were prepared in the following manner. First the glass substrates were scrubbed by hand using a soap mixture for at least one minute on each side. In this step the rough and smooth side would be identified. The amorphous layer would only be deposited on the smooth side. After scrubbing, the glass substrates

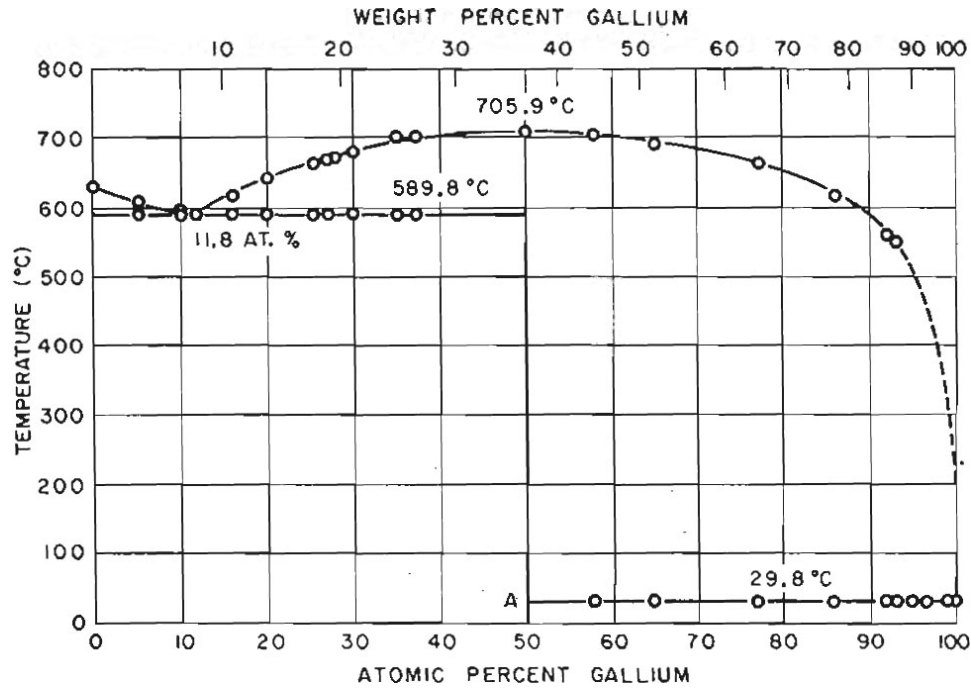


Figure 3.1: Phase Diagram of the Gallium Antimony System. Above 705.9°C the mixture will always be in the liquid state. Figure adopted from [14].

were rinsed for five minutes in demi water. This was followed by a bath in acetone for ten minutes, which is sonicated. Afterwards, again the glass substrates are rinsed with demi water for five minutes. This is followed by a bath in isopropyl alcohol for ten minutes, which is sonicated. The substrates are spin-dried and placed in an oven at 140°C for ten minutes. Up to three glass substrates could be placed in the e-beam evaporator.

Step	Δt	T_{start}	T_{finish}	ΔT
1	6 h	20°C	650°C	630°C
2	1.5 h	650°C	650°C	0°C
3	1 h	650°C	725°C	75°C
4	8 h	725°C	725°C	0°C
5	6 h	725°C	20°C	-705°C

Table 3.1: Process steps for melting the target mixture in the Navitherm Controller P320 oven

3.1.3 E-beam evaporation

The e-beam evaporator used was a Varian 3120. Power supply and gun control were made by Airco Temescal (Gun control model CV-8). To attain rough vacuum a Edwards E2M40 vacuum pump was used. High vacuum was attained using a diffusion pump with cold trap. The minimum vacuum attained before the start of deposition was $5 \cdot 10^{-6} \text{mbar}$.

The deposited layer thickness was estimated by means of a quartz crystal micro balance (QCM). In order for QCM to work, the e-beam evaporator needs to know the density ρ and acoustic impedance Z of the target material. Since various alloys of GaSb were used as a target. The density ρ and acoustic impedance Z of the targets were estimated by linear interpolation of the values for density and acoustic impedance of Gallium, Antimony and Ga₅₀Sb₅₀. Whose values were obtained from literature [15] [16] [17] and can be found in table 3.2.

The deposition rate was controlled by manually increasing and decreasing the current running through the filament of the e-beam evaporator.

	ρ [gm/cm^3]	Z_{ac} [$10^5 gm/cm^2s$]
Gallium (Ga)	5.930	14.890
Antimony (Sb)	6.620	11.490
(GaSb)	5.614	22.3

Table 3.2: Literature values to estimate constants necessary for e-beam evaporation. [15] [16] [17]

3.2 Sample preparation for experiments

3.2.1 Checking deposition structure with optical microscope

A first qualitative check to see whether the deposited layer was amorphous or crystalline, was to observe the sample with an optical microscope. Two microscopes were used: an Olympus BX5, with the Olympus analySIS Docu software package and a Olympus Vangox-T AH2, which was modified with a Olympus U-PMTVC Camera Adapter and used the analySIS software package. Various digital filters were used to enhance the contrast of the recorded image when the Olympus BX5 was used. Various polarization filters were used to enhance the contrast of the recorded image when using the Olympus Vangox-T AH2.

3.2.2 Checking thickness with DEKTAK

Since the values of the density ρ and acoustic impedance Z of the target are based on linear interpolation, and therefore, not exact, the thicknesses of the deposited layers were also measured using a Stylus Profilometer Veeco DEKTAK 150, with the Vision Analysis software package.

3.2.3 Checking deposition structure and composition

SEM was used to check the homogeneous nature of the deposited layer and to check whether crystals could be observed, it was also used to observe the surface structure of the target. EDX was used to determine the composition of the layer. To get the most accurate reading possible, a flat piece of material is required.

The top of the layer is defined as the last deposited part of the layer and is visible by the eye. The bottom of the layer is defined as the first deposited part of the layer and is closest to the glass substrate. Double sided carbon tape was placed on a SEM stub. This was in turn pressed against the deposited layer. In this manner a flat piece of the deposited layer was removed from its glass substrate, with bottom facing upward and the top being connected to the double sided carbon tape.

3.2.4 Cutting samples to have identical samples

A single sample consisting of a 30mm \times 30mm glass substrate with a deposited amorphous layer, was cut into smaller pieces using diamond cutting pen. If the layer is uniform, every small piece should have the same material properties. To prevent damage to the deposited layer it was coated with a PMMA polymer. When the sample had been cut into smaller pieces the PMMA layer was removed by rinsing the pieces multiple times in acetone and isopropanol. Isopropanol is used to minimise the amount of acetone residue. The samples were blown dry using pressurized nitrogen.

3.3 Isothermal and electron irradiation crystallisation experiments

3.3.1 Isothermal crystallisation experiments

The setup to perform isothermal experiments consists of the following elements: a Photron FASTCAM 1024 PCI high speed camera, with a Navitar ZOOM 6000 lens, the sample is heated with a Watlow Ultramic 600 ceramic heater. Camera and heater are controlled using a PID controller and software written by Gert Eising in VB.Net.

JMAK theory assumes a total instantaneous isothermal state. In reality this is not possible. To minimise the impact that heating the sample might

have on its kinetic properties, all samples need to be heated in exactly the same way. To have an estimate of the nucleation probability n , there needs to be an incubation time as well. Isothermal experiments are therefore performed in the following manner. A sample is placed on the ceramic heater and manually put into focus. Then a background image is taken to remove defects in the layer and to reduce noise for the computer analysis of the images afterwards. The sample is heated at a constant rate of $10^{\circ}\text{C}/\text{min}$ to a target temperature T_{goal} . After an incubation time t_b the sample will start to crystallise. When the sample is fully crystallised the sample is cooled down again. For reference a scale of 1mm is photographed afterwards.

Digital analysis of the obtained images is used to identify the boundaries of the amorphous and crystalline state. The images are analysed based on a method described in a article written by Jasper Oosthoek [18]. The general idea is that for every image taken at a certain time, the crystal boundary is detected. This allows for the creation of a boundary time map, which is then converted into a growth rate map. In this manner the growth rate during the entire transformation process and the ratio between the transformed volume V and untransformed volume $(1 - V)$ can be determined.

Chapter 4

Creation of amorphous layers of $\text{Ga}_x\text{Sb}_{100-x}$ using e-beam evaporation

To reproduce the results of the isothermal annealing experiments described in the next two chapters, it would be sufficient to state the exact procedure of how the samples of $\text{Ga}_x\text{Sb}_{100-x}$ were created, but the goal of this chapter is to provide a manual to future researchers for the creation of amorphous $\text{Ga}_x\text{Sb}_{100-x}$ layers using e-beam evaporation for layer deposition and EDX for sample and target composition analysis. Before using the information presented in this chapter, it should be checked if alternative modes of sample creation and analysis provide more accurate and satisfactory results.

A small variation in layer composition can have a large impact on the physical properties of the amorphous layer and that many variables influence the composition of the deposited amorphous $\text{Ga}_x\text{Sb}_{100-x}$ layer. The first two sections of this chapter are meant to show the limitations in controlling these variables, and thus the limitations in controlling of the physical properties of the deposited layer with the current experimental setup. Then it will be shown how each variable influences the amorphous sample composition.

First the relation between the composition of the target and the composition of the deposited layer will be shown. Then it will be shown that when a target is used to create multiple samples, the Gallium concentration increases for consecutive samples. This is caused by a shift in target composition during the evaporation process. Other factors that influence the sample composition are: evaporation speed, target state, target shape and absolute weight.

In the last section the knowledge gained from the previous sections will be combined to give instructions in creating useful samples of $\text{Ga}_x\text{Sb}_{100-x}$ for isothermal heating experiments and explosive crystallisation experiments, based on the limitations of the used experimental setup.

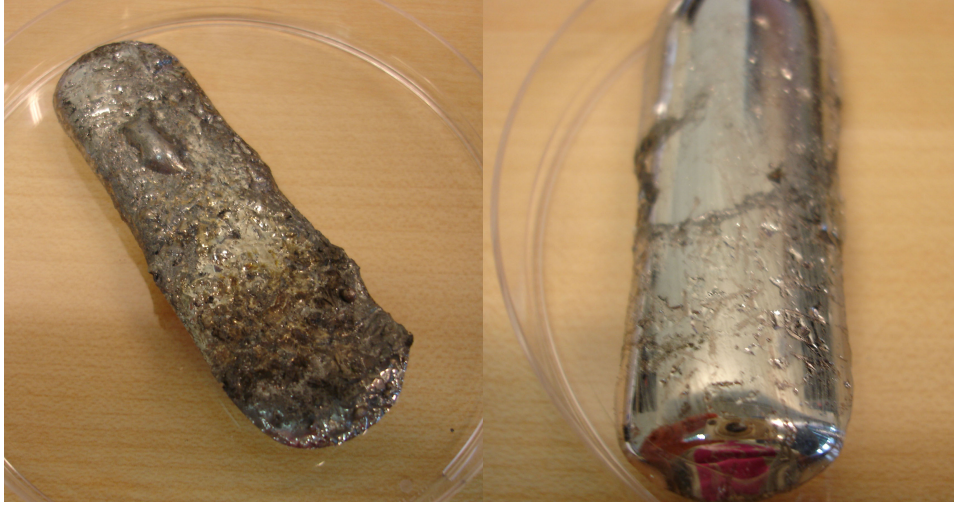


Figure 4.1: A typical target after it has been removed from the quartz container. Target displayed is $\text{Ga}_{78}\text{Sb}_{22}$.

4.1 Target and sample composition analysis using SEM and EDX

To make sure the ratio between Gallium and Antimony deposited on the glass substrate is as equal as possible across the substrate surface, the target ratio between Gallium and Antimony needs to be as equal as possible throughout the target volume as well. To ensure this, the target material is fully liquefied by heating the quartz capsule to 725°C . A typical target removed from the oven is shown in Figure 4.1. It is far from the uniform alloy one would expect it to be. To completely solidify a $\text{Ga}_x\text{Sb}_{100-x}$ target, where $x > 50\%$ it needs to be cooled below the freezing temperature of Gallium of 30°C and below room temperature. This can be done by either cooling the quartz container with running water, or placing the target in the freezer. When the target temperature returns to room temperature, it remains solid.

The rough surface area of the target shown in Figure 4.1, in combination with blister like pockets of liquid which is most likely Gallium, leads to the assumption that the target is not a uniform alloy. This is confirmed in the SEM images shown in Figure 4.2. Figure 4.2a shows a target with composition $\text{Ga}_{50}\text{Sb}_{50}$, most of the target forms an GaSb alloy, with some pockets of Antimony. Figure 4.2b shows a target with composition $\text{Ga}_{80}\text{Sb}_{20}$. A layered structure of GaSb and Ga layers is formed. The target mixture forms GaSb in combination with pockets of Gallium or Antimony, depending on which of the two is in excess. When there is much more Gallium than Antimony in the target, and the target has not been cooled below room temperature, another effect can be observed. Gallium migrates to the surface

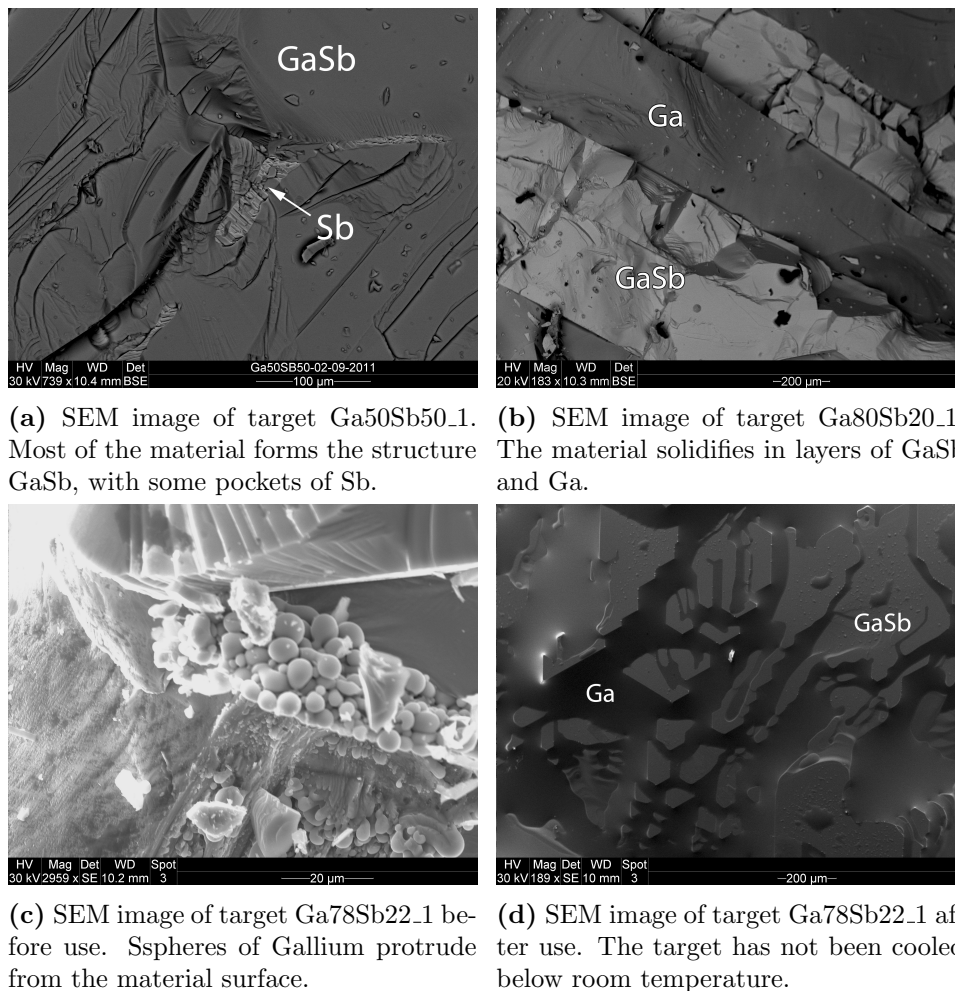


Figure 4.2: SEM images of multiple targets in various composition and states of solidification.

of the target. In Figure 4.2c this effect has been frozen in time in the form of Gallium spheres protruding from the target surface. Figure 4.2d shows a target that has not been cooled below room temperature and shows a moment in time, where islands of GaSb are still visible, during the course of the measurement these islands were submerged in Gallium. This behaviour of the target material and the aforementioned segregation property of the target material makes EDX an unreliable method for target composition determination.

What can be determined to a very accurate degree is the weight of Gallium and the weight of Antimony that has been put into the crystal quartz container. Taking into account all the inaccuracies of the entire mixing process, it is possible to determine a range of compositions, wherein the

Target Name	Ga_{max} %	Sb_{min} %	Ga_{min} %	Sb_{max} %
Ga0Sb100.1	0.00	100.00	0.00	100.00
Ga50Sb50.1	49.17	50.83	48.92	51.08
Ga60Sb40.1	62.00	38.00	58.24	41.76
Ga75Sb25.1 ¹	Unknown	Unknown	75.06	24.94
Ga78Sb22.1	78.08	21.92	77.95	22.50
Ga78Sb22.2 ²	78.08	21.92	77.95	22.50
Ga78Sb22.3	78.03	21.97	77.91	22.09
Ga78Sb22.4	78.03	21.97	77.94	22.06
Ga78Sb22.5	78.02	21.98	77.94	22.06
Ga80Sb20.1 ³	Unknown	Unknown	82.35	17.65

Table 4.1: List of all targets created and composition according to weight analysis. Ratios given are atomic ratios. Ga_{max} means the maximum atomic Gallium percentage based on the weight measurements during the creation of the target. Sb_{min} is the corresponding Antimony concentration to Ga_{max} . Ga_{min} and Sb_{max} have similar meanings.

target composition must lie. This range can be determined with an accuracy of 0.01At%, and is shown for all created targets in Tabel 4.1. Target names have been chosen to represent their desired composition, thus for target Ga78Sb22.1 the desired composition was $Ga_{78}Sb_{22}$. The number 1 indicates it was the first target created with that desired composition.

Fortunately, the deposited layer is fairly homogeneous as can be seen in Figure 4.3. Unfortunately, according to EDX measurements there is some variation in the composition across the sample surface. It is rather difficult to determine the accuracy of the EDX measurement, since there are many factors that could influence it, including the flatness of the sampled material in question. Sample composition is thus determined by taking the average of multiple measurements across the surface. This allows for a qualitative analysis of the effect of increasing Gallium concentration in the sample, but makes a quantitative analysis rather difficult.

¹The funnel used to put Antimony shots into the quartz vial contained Gallium residue, as a result some Antimony shots were trapped and a small amount of extra Gallium ended up in the vial, therefore Ga_{max} and Sb_{min} can not be stated with absolute certainty.

²In general, more target material is created then can be used in the crucible of the e-beam evaporator. Ga78Sb22.1 and Ga78Sb22.2 are made from the same target material.

³The listed composition is the desired one and NOT based on weight analysis. Based on the mixing procedure, it is estimated that this is a good approximation.

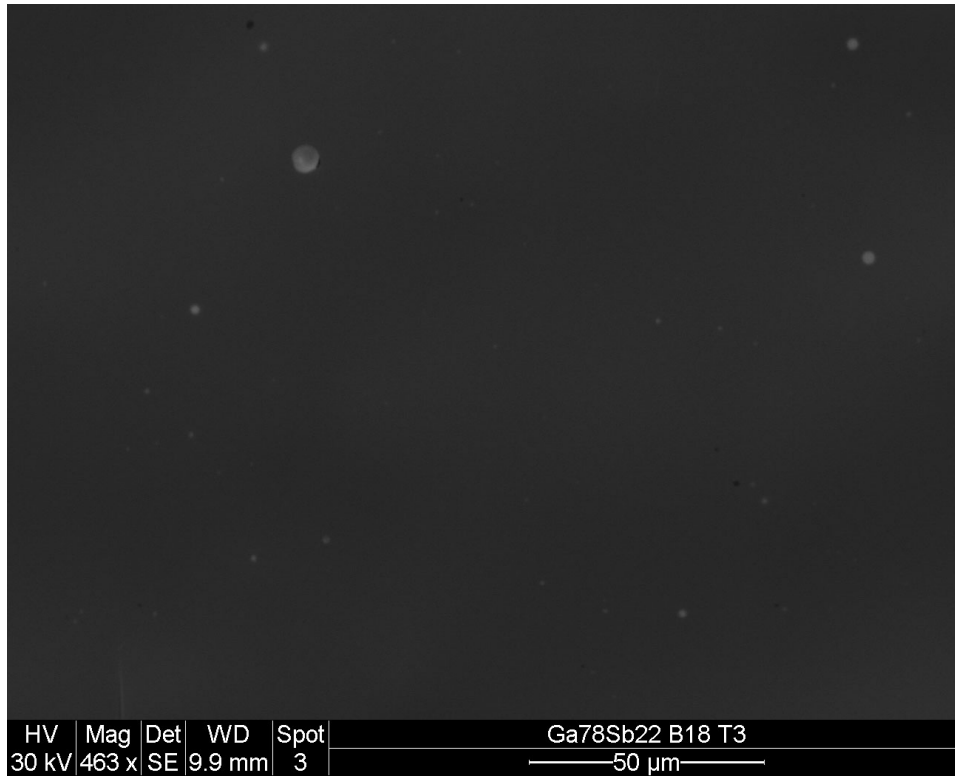


Figure 4.3: SEM image of typical of as deposited Ga_xSb_{100-x} layer. Sample displayed is Ga78Sb22_B18, with composition $Ga_{13.55}Sb_{86.45}$. It is the fourth sample made with target Ga78Sb22_3.

4.2 Limitations in the use of the Varian 3120 e-beam evaporator

In the later sections of this chapter it will be shown that the target composition changes during the evaporation process and that the composition of the as deposited material is dependent on the layer deposition rate. For correct interpretation of these sections it is necessary to know how layer deposition rate varies during the layer deposition process.

The following statements are not all based on hard measurements, but are meant to give the reader an understanding in the accuracy with which evaporation speed can be controlled inherently when using the Varian 3120 e-beam evaporator. Layer deposition rate can be read from a digital display and is controlled by manually adjusting the current running through the filament. For a constant layer deposition rate, this needs to be done continuously. The observed layer deposition rates on the digital display lay on an interval around the desired layer deposition rate. The width of this interval is dependent on the strength of the desired layer deposition rate, see Table

Desired layer deposition rate	Observed range
0.2 nm/s	0.1 - 0.3 nm/s
1.5 nm/s	1.1 - 1.9 nm/s

Table 4.2: The relation between desired layer deposition rate and the range of the observed layer deposition rates.

4.2. If a histogram would be made of the observed layer deposition rates it would form a bell curve around the desired layer deposition rate.

The displayed speed is determined by means of QCM, which is in turn based on the density and acoustic impedance of the material. It turned out that the value for the acoustic impedance found in literature of 22.3 g/(cm²s) [15] [16] [17] did not provide satisfactory results in controlling evaporation speed and was discarded. Instead a linear interpolation between the acoustic impedance of Gallium and Antimony was used. Since density and acoustic impedance are based on linear interpolations for the values of Gallium, Antimony, and GaSb this creates an inherent inaccuracy in the displayed layer deposition rate and thickness of the deposited layer. Furthermore, since target composition changes throughout the evaporation process, this error is not constant.

To gain an insight in these errors, evaporation time was tracked with a stopwatch and thickness of the layer was double-checked using a DEKTAK profilometer. When determining target material properties by mean of the aforementioned linear interpolations based on the target compositions displayed in Table 4.1, layers that were supposed to be 200nm thick were between 10% and 20% thicker. Layers where the desired thickness was higher than 1 micrometer were between 20% and 33% thicker. Thicknesses and evaporation speeds mentioned in later sections are based on DEKTAK measurements and stopwatch time unless mentioned otherwise.

4.3 Results of layer deposition using e-beam evaporation

To effectively control the composition of the deposited layer a couple of factors need to be taken into consideration. The first is that target composition does not match the composition of the deposited layer. The second is that when a target used multiple times, the Gallium content of the deposited layer increases with every use. It will be shown that this can be attributed to the weight loss of the target and its subsequent change in composition, due to the difference in evaporation rate between Gallium and Antimony. The speed with which the amorphous layer is deposited also influences its composition, with a higher evaporation speed increasing the Gallium content of

Target Name	e-beam Settings		Thickness	Deposition Speed	Sample Composition	
	Density ρ (g/m ³)	AZ-Value Z g/(cm ² s)			d (nm)	v (nm/s)
Ga50Sb50_1 ⁴	5.641	14.74·10 ⁵	200	0.2 ⁵	1.92	98.08
Ga60Sb40_1	5.641	14.74·10 ⁵	190	0.19	2.43	97.57
Ga75Sb25_1	5.641	14.81·10 ⁵	850	0.16	4.81	95.19
Ga78Sb22_1	5.782	14.82·10 ⁵	220	0.14	10.42	89.58
Ga80Sb20_1	5.641	14.74·10 ⁵	185	0.2 ⁶	25.94	74.06

Table 4.3: Composition of the first samples created with the aforementioned targets. Since evaporation speed and thickness have an influence on the composition and material properties of the sample they are also listed for clarity. Target properties can be found in Table 4.1

the deposited layer. The Gallium content measured in subsequent samples created with the same target first seems to drop and then continuously increase. An attempt to explain this effect will be given in the last subsection.

4.3.1 The relation between target composition and layer composition.

The composition of the first samples created with targets of different desired composition is given in Table 4.3. It has been attempted to keep all aspects of the evaporation process as equal as possible. To this end, the composition of the second sample created with target Ga50Sb50_1 is shown, since the first sample was deposited with much higher evaporation speeds and had a much greater thickness. Notable exception in sample thickness is the first sample created with target Ga75Sb25_1 which has a thickness of 850 nm. Although composition changes with increasing thickness, it is assumed that in this case this will not pose a great problem since it will be shown that first the gallium content in the deposited layer is decreased before it increases again.

The target Gallium content is plotted against the sample Gallium content in Figure 4.4. There is a sudden increase in Gallium content of the deposited layer, when the Gallium content in the target becomes higher than 75%. The two theoretical points are meant emphasize the suddenness of the increase, by providing a visual reference point in case of pure Antimony and pure Gallium targets.

⁴Not the first sample created, but the second sample. The first sample was 970nm thick and had been deposited with an extremely fast evaporation speed. This makes the second sample a more suitable measurement point.

⁵This is the desired speed, the evaporation time had not been recorded.

⁶This is the desired speed, the evaporation time had not been recorded.

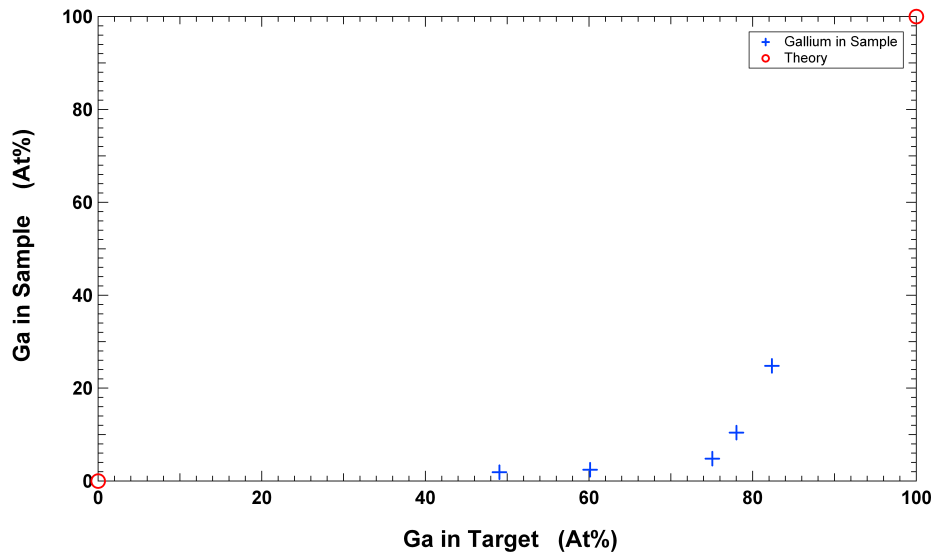


Figure 4.4: The Gallium content in the deposited layer of the first created sample in At% against the Gallium content in the used target in At%. The two theory points indicate cases of a pure Antimony and a pure Gallium target.

4.3.2 The change of target composition during the evaporation process

As a target was sequentially used to create multiple samples, the Gallium concentration in the deposited layer increased with each subsequent sample. Explosive crystallisation has been reported in thick films of GaSb, with a thickness in the order of $2\mu\text{m}$ [5]. It is therefore useful to study how the composition of the deposited layer changes with the continued use of single target to create these thick layers.

The penetration depth of EDX is strongly dependent on the acceleration voltage among other things. All experiments were performed at an acceleration voltage of 30keV, leading to a penetration depth in the order of $2\mu\text{m}$ to $3\mu\text{m}$ for $Ga_{50}Sb_{50}$ according to the Kanaya-Okanaya Depth Penetration Formula [19]. The strength of the signal that reaches the detector changes with depth. The composition signal strength retrieved from deeper layer sections is weaker, than those retrieved from layer sections closer to the surface, these leads to an over representation of the layer composition at the top in the representation of the average layer composition. EDX will give an accurate description of the average layer composition of layers with a thickness of 200nm or 400nm, but in the case of layers of 2000nm or more, EDX will give an underestimation of the Gallium composition of the sample, since bottom of the layer is visible and the top is pressed against the carbon tape, see section 3.2.3.

In determining how the deposited layer composition changes with continued use of the same target, all other variables that might have an influence on deposited layer composition were kept constant as possible. Three targets were used with the same starting composition $Ga_{78}Sb_{22}$: target $Ga_{78}Sb_{22.3}$, $Ga_{78}Sb_{22.4}$, and $Ga_{78}Sb_{22.5}$, henceforth named as target 3, 4 and 5 respectively. Information on the samples created with these targets can be found in Table 4.4. The goal was to create sample with a thickness of 200nm which had been deposited with a speed of 1.5nm/s. Exceptions on this rule are sample 8 from target 3, sample 3 from target 4, and sample 2 from 5. These samples were created to see if continuous deposition changed the effect of increasing Gallium composition and to create thick amorphous layers to study explosive crystallisation.

The actual deposited layer thickness, measured using a DEKTAK profilometer can be found in the third column of Table 4.4. Using this information and the time it took to deposit a certain layer, the average deposition speed can be determined. This can be found in the fourth column of Table 4.4. It takes some time before the evaporation speed is more or less constant. The shutter, separating target from substrate, was opened only when evaporation speed was under control. This means a certain amount of material is already evaporated before the shutter is opened. Using this information and the actual layer thickness as measured with a DEKTAK profilometer, the total layer thickness deposited on the QCM crystal during the creation of a single sample can be estimated and is shown in the second column of Table 4.4 under QCM. s, measured using a DEKTAK profilometer can be found in the third column of Table 4.4. Using this information and the time it took to deposit a certain layer, the average deposition speed can be determined. This can be found in the fourth column of Table 4.4. It takes some time before the evaporation speed is more or less constant. The shutter, separating target from substrate, was opened only when evaporation speed was under control. This means a certain amount of material is already evaporated before the shutter is opened. Using this information and the actual layer thickness as measured with a DEKTAK profilometer, the total layer thickness deposited on the QCM crystal during the creation of a single sample can be estimated and is shown in the second column of Table 4.4 under QCM.

The information regarding the sample composition as shown in the fifth and sixth column of Table 4.4 is shown in Figure 4.5. On the vertical axes the measured Gallium concentration in a sample is depicted and on the horizontal axes the total amount of nanometres deposited with a single target is shown. Every colour in Figure 4.5 represents a different target. Every horizontal stripe is a different sample, with the first sample that was created being the most left horizontal stripe and the last sample created

⁷This is the desired speed, the evaporation time had not been recorded

Target Ga78Sb22_3					
Sample Number	Layer Thickness		Deposition Speed	Sample Composition	
	QCM Total (nm)	Sample (nm)	v (nm/s)	Ga At%	Sb At%
1	440	220	1.59	9.15	90.85
2	450	225	1.54	8.85	91.15
3	285	225	1.53	10.58	89.42
4	470	235	1.74	13.55	86.45
5	230	230	1.80	14.21	85.79
6	560	250	1.68	16.65	83.35
7	430	215	1.53	20.80	79.20
8	3045	2450	1.70	30.50	69.50

Target Ga78Sb22_4					
Sample Number	Layer Thickness		Deposition Speed	Sample Composition	
	QCM Total (nm)	Sample (nm)	v (nm/s)	Ga At%	Sb At%
1	486	215	1.24	12.67	87.33
2	477	205	1.50 ⁷	11.79	88.21
3	698	430	1.64	14.36	85.64

Target Ga78Sb22_5					
Sample Number	Layer Thickness		Deposition Speed	Sample Composition	
	QCM Total (nm)	Sample (nm)	v (nm/s)	Ga At%	Sb At%
1	558	250	1.74	13.04	86.96
2	2759	1950	1.82	12.09	87.91

Table 4.4: Information on samples created with targets Ga78Sb22_3, Ga78Sb22_4, and Ga78Sb22_5. The relationship between the sample composition and the total layer thickness deposited with a single target can be seen in figures 4.5 and 4.9. The initial drop drop in Gallium content and resultant increase as deposition is continued with a single target can be seen in figure 4.7. Information on the targets themselves can be found in Table 4.1

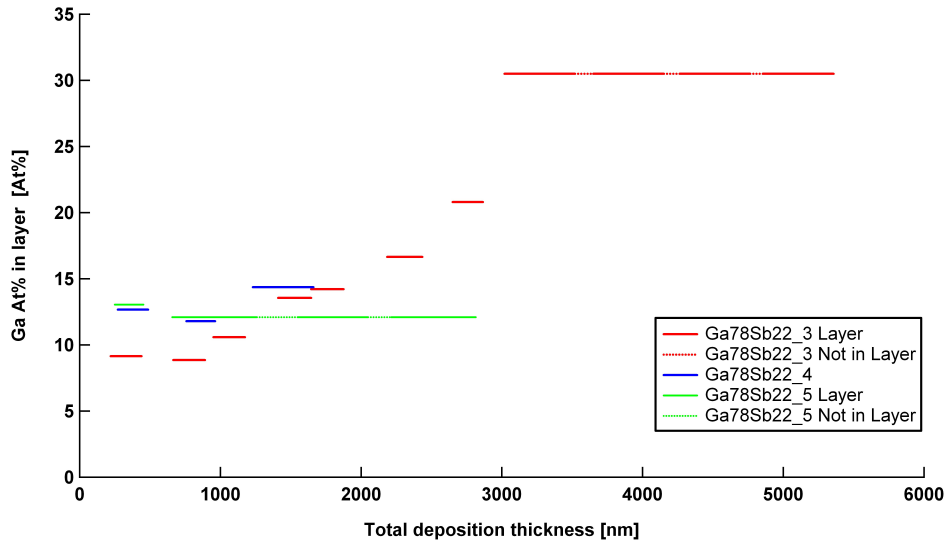


Figure 4.5: Change in composition of the deposited layer as the target is used multiple times. More information on the creation of individual samples can be found in Table 4.4. More information on the individual targets can be found in Table 4.1.

being the most right horizontal stripe. The width of a stripe represents the thickness of the sample. The space between samples is the thickness of the layer which was deposited on the QCM crystal before the shutter was opened. The maximum layer thickness that the e-beam evaporator could keep track of was 1000nm. Therefore, to keep track of the thickness of layers exceeding 1000nm, multiple programs were used. The shutter was closed in between programs, so in between programs, materials was deposited on the QCM crystal, but not on the substrate. The dotted lines represent the thickness of the deposited layer in between programs.

Figure 4.5 shows the following trend for target 3 and 4: with continued use of a single target first the composition in the deposited layer drops and then it rises continuously. Although target 3 and target 4 show the same trend, the measured Gallium content in the samples created with target 4 is higher than those created with target 3. The measured Gallium content of the second sample created with target 5 is lower then one would expect on the basis of the samples created with target 3 and 4. The effect of decreasing and increasing Gallium content in the deposited layer as well as low Gallium content measured in the second sample created with target 5, will be explained in following sections.

Target Ga78Sb22_4					
Sample Number	Weight Target		Weight Reduction		Weight loss per nm of deposition
	Before	After	Evaporated	Removed	
	(gram)	(gram)	(gram)	(gram)	
1	39,25	38,50	0,75	1,18	1,54
2	37,32	36,64	0,68	0,57	1,43
3	36,07	35,13	0,94	1,36	1,35

Target Ga78Sb22_5					
Sample Number	Weight Target		Weight Reduction		Weight loss per nm of deposition
	Before	After	Evaporated	Removed	
	(gram)	(gram)	(gram)	(gram)	
1	40,48	39,69	0,79	0,53	1,42
2	39,16	35,35	3,81	0,60	1,38

Table 4.5: In this table the target weight reduction during during sample creation is shown. Information on the layer thickness that was deposited can be found in Table 4.4. Information on the used targets can be found in Table 4.1.

Target composition change during the evaporation process.

To proof that target composition changes during the evaporation process, and that this in turn causes the change in layer composition with when multiple samples are are created with one target, the weight of the evaporated target material is used. The change in target weight during the creation of samples using targets 4 and 5 is shown in Table 4.5. Columns one and two show the target weight before and after the creation of a sample. Columns three and four show the total weight loss during the entire evaporation process and the weight of a sample removed from the target between evaporation sessions. Column five uses the the total layer thickness deposited on the QCM crystal, as shown in Table 4.4, to determine the average weight loss of the target per deposited nanometre. This information is used to approximate the target composition change during the evaporation process.

The proof consist of three steps, and is based on the fact that layer composition depends on target composition, see Figure 4.4. The first step is to estimate how much the target composition changes during the evaporation procedure. The second step is to use this estimation and the relation between target composition and layer composition to estimate the composition of the next sample that will be made with the target. The third is to compare the this estimated sample composition with the actual measured sample composition.

Since the Gallium concentration in the sample is lower than the Gallium

concentration in the target, it is expected that the Gallium concentration in the target increases. Therefore, it is assumed that the change in target composition due to evaporation can not explain the drop in Gallium concentration for the first few samples, see Figure 4.5 and 4.7. To remove the observed Gallium drop from our estimation, the second sample that was created is treated as if it were the first created sample and it is assumed that the target composition did not change during the creation of the first sample.

The target composition before use is known, see Table 4.1. The total evaporated weight is known, see Table 4.5. The average composition of the deposited layer is known, see Table 4.4. It is assumed that the evaporated material had the same composition as the deposited layer⁸. This will all be used to estimate the change in target composition and the target composition after use.

During the creation of sample 2 using target 4, 0.68 gram of target material has been evaporated, see Table 4.5. The standard atomic weight of Gallium is 69.723, while the standard atomic weight of Antimony is 121.760 [20]. This leads to the following conclusion; out of the 0.68 evaporated target material, 0.048 gram is Gallium and 0.632 gram is Antimony. Before the creation of sample 2, target 4 consisted of 25.00 gram Gallium and 12.32 gram Antimony, see Table 4.5 and 4.1, and had a composition of $Ga_{78}Sb_{22}$, see Table 4.1. Therefore, it is estimated that after the creation of sample 2 target 4 consisted of 24.96 gram Gallium and 11.68 gram Antimony and had a composition of $Ga_{78.86}Sb_{21.14}$.

The composition of sample 2 from target 4 is $Ga_{11.79}Sb_{88.21}$, see Table 4.4. The composition of target $Ga_{80}Sb_{20_1}$ is $Ga_{82.35}Sb_{17.65}$, see Table 4.1. The composition of the second sample created with target $Ga_{80}Sb_{20_1}$ is $Ga_{24.80}Sb_{75.20}$, see Table 4.6. It is assumed that sample composition changes linearly with target composition between these two samples⁹.

Using the linear interpolation between the composition of sample 2 from target 4 and sample 2 from target $Ga_{80}Sb_{20_1}$, it is estimated that the composition of the deposited layer of sample 3 is $Ga_{14.36}Sb_{83.64}$. From Table 4.4 it can be seen that the measured composition of sample 3 of target 4 was $Ga_{14.36}Sb_{83.64}$. The accuracy of up to four digits should be attributed to coincidence, but the calculation above shows that the increase in Gallium composition of the deposited layer with continuous use of the same target is

⁸The measured composition of sample 2 from target 4 is the average composition of the layer which was deposited on the glass substrate. The composition of the layer which was deposited on the QCM crystal before the shutter was opened is unknown. Because the Gallium content in the layer increases with continuous use of a single target, the Gallium concentration for the entire deposited layer (before and after opening the shutter) will be overestimated. This will lead to an underestimation of the change in target composition. This has a compensating effect on the overestimation due to the linear interpolation.

⁹This is an overestimation, but acceptable between these two points, see Figure 4.4

due to the change in target composition, which is caused by the inequality between the target composition and the composition of the deposited layer.

4.3.3 The influence of layer deposition rate on layer composition.

The layer deposition rate was intended to be equal for all samples created using targets 3, 4 and 5, see Table 4.4. This was not the case for samples created using target Ga78Sb22_1 henceforth known as target 1; the desired layer deposition rate varied from sample to sample. Eleven samples were created using target 1. The desired thicknesses of the first 9 samples was 200 nm. The desired thicknesses of sample 10 and 11 was 800nm. The difference in desired evaporation speed in the creation of the samples using target 1 can be used to determine the influence of evaporation speed on the composition of the deposited layer. Unfortunately for most samples created with sample 1 it the thickness of the layer deposited before the shutter is opened is unknown. Therefore the results obtained from the samples created with target 1 is depicted as a bar chart which can be seen in Figure 4.6

The sample number is depicted inside the bar. Samples are numbered in order of creation. The width of the bar represents the thickness of the sample. The layer deposition rate is noted above the bar. For most sample the evaporation time had not been tracked, thus the noted layer deposition rate is the desired layer deposition rate. Evaporation time had been tracked for samples 1, 2 and 10. Average deposition speed was 0.141nm/s, 0.046nm/s and 0.822nm/s respectively. Determination of layer composition using EDX differed with respect to the samples created with targets 3, 4 and 5. Instead of sticking the double sided carbon taped against the deposited layer and removing a piece of layer from the substrate, a scalpel was used to scrape flakes of the deposited layer of the substrate surface.

From Figure 4.6 the same general pattern can be observed as in Figure 4.5. There are, however, deviations from this general trend. The Gallium concentrations measured in samples 2, 4 and 6 is lower than that of their predecessors; samples 1, 3, and 5. It should also be noted that the drop in Gallium concentration for sample 2 is much stronger than observed in the second sample created using targets 3, 4 and 5.

The desired evaporation speed for samples 2, 4, and 6 is lower than the desired evaporation speed of samples 1, 3, and 5, while the opposite is not observed; a sample whose Gallium content is lower than its predecessor, while it was deposited with a layer deposition rate higher than its predecessor. Therefore it is concluded that layer deposition rate has an influence on the composition of the deposited layer; an increase in layer deposition rate leads to an increase in the Gallium content of the deposited layer.

The Gallium concentration in sample 5 is almost equal to the Gallium concentration in sample 7, while the layer deposition rate of sample 7 is half

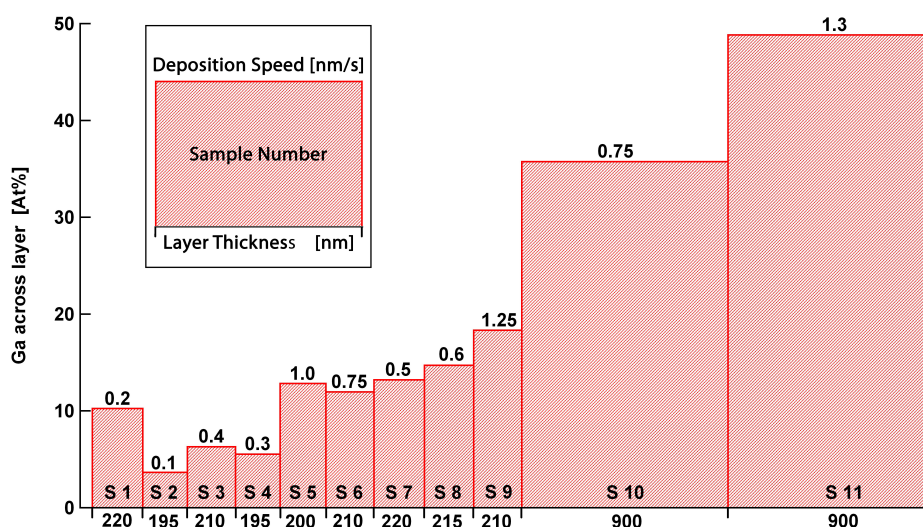


Figure 4.6: Samples were created with target $\text{Ga}_{78}\text{Sb}_{22.1}$. In this bar chart the width of the bar represents the thickness of the sample, while the height of the bar represents the average Gallium content across the layer as measured with EDX. The desired layer deposition rate for a specific sample is indicated above its corresponding bar. Info on target $\text{Ga}_{78}\text{Sb}_{22.1}$ can be found in Table 4.1

that of sample 5. The Gallium concentrations of samples 7 and 8 are higher than the Gallium concentration in 6, although the layer deposition rates for samples 7 and 8 are lower than that of sample 6. This means that, although layer deposition rate influences the composition of the deposited layer, target composition is the dominant factor in determining the composition of the deposited layer.

4.3.4 Analysis of Gallium concentration drop during the deposition of the first few hundred nanometres.

The drop in Gallium concentration in the beginning of layer deposition is most likely caused by a change in the structure of the target.

The claim of a drop in Gallium concentration during the first few hundred nanometres is based on a drop observed in targets 1, 3, 4, and 5. The observed drop is not very strong in target 4 and even less so in target 3. The second sample created with target 5 is much thicker, which makes comparison with the other targets troublesome and the drop in gallium concentration for the second sample in target 1 could be attributed to a reduction in

¹⁰This is the desired speed, the evaporation time had not been recorded

¹¹This is the desired speed, the evaporation time had not been recorded

¹²This is the desired speed, the evaporation time had not been recorded

Target Ga50Sb50_1						
Sample Number	Layer Thickness	Deposition Speed	E-beam Settings		Sample Composition	
	d (nm)	v (nm/s)	ρ (g/m ³)	Z g/(cm ² s)	Ga At%	Sb At%
1	970	N.A.	5.614	22.3	1.56	98.44
2	200	0.2 ¹⁰	5.614	14.74	1.92	98.08

Target Ga75Sb25_1						
Sample Number	Layer Thickness	Deposition Speed	E-beam Settings		Sample Composition	
	d (nm)	v (nm/s)	ρ (g/m ³)	Z g/(cm ² s)	Ga At%	Sb At%
1	850	0.16	5.614	14.74	4.81	95.19
2	850	0.21	5.762	14.81	8.93	91.09
3	3200	1.26	5.762	14.81	21.10	78.90

Target Ga80Sb20_1						
Sample Number	Layer Thickness	Deposition Speed	E-beam Settings		Sample Composition	
	d (nm)	v (nm/s)	ρ (g/m ³)	Z g/(cm ² s)	Ga At%	Sb At%
1	185	0.2 ¹¹	5.614	14.74	25.94	74.06
2	220	0.2 ¹²	5.614	14.74	24.80	75.20

Table 4.6: In this Table the settings for samples created from targets Ga50Sb50_1, Ga75Sb25_1, and Ga80Sb20_1 are listed. Information regarding the composition of the samples is plotted in Figure 4.7. Information on the targets can be found in Table 4.1. The layer deposition rate of the first sample created with Ga50Sb50_1 is not available, because a thick layer of 970nm had been deposited within several seconds with wildly fluctuating layer deposition rates.

layer deposition rate. It is tempting to attribute the observed drop to the inaccuracy of the EDX measurement.

To strengthen the claim that this is not the case, information from samples created with targets Ga50Sb50_1, Ga75Sb25_1, and Ga80Sb20_1, see Table 4.6 and Figure 4.7, is used. Targets mentioned in Table 4.1, but not mentioned in this section have only been used once and are therefore irrelevant for this discussion. Special attention is placed on the layer deposition rates in the third column of Table 4.6, since it has an influence on the composition of the deposited layer. The deposition rate of the first sample created with Ga50Sb50_1 is not available (NA), because a thick layer of 970nm had been deposited within several seconds with wildly fluctuating deposition rates.

The average Gallium concentration in the first two or three samples created with the targets mentioned in Table 4.4, 4.6 and Figure 4.6 are shown in Figure 4.7. The layout of Figure 4.7 is identical to that of Figure 4.5. Samples for which the thickness of the deposited layer prior to opening the shutter is unknown are proceeded with a question mark.

The drop in Gallium concentration was not observed in samples created with targets Ga50Sb50_1 and Ga75Sb25_1. A possible explanation would be that the first samples were rather thick. Since the drop in Gallium content appears to happen during the first few hundred nanometres of deposition use of the target and EDX only measures only the average Gallium content across the entire layer, the drop would simply remain unobserved.

Several shapes and forms of target material in a crucible are depicted in Figure 4.8. In Figure 4.8a target Ga78Sb22.5 is shown before use. The target does not uniformly fill the crucible. Target Ga78Sb22.5 had been cooled below room temperature before removal from the crystal vial. Blister like structures of solidified material were seen on the outside of the target. These structures could also be described as if several rain droplets had agglomerated together on a flat surface and were then frozen. It is assumed that is excess Gallium which has migrated to the target surface, see Figure 4.2 in section 4.1. During the evaporation process the target is completely melted, when it is removed from the e-beam evaporator after use it is no longer a complete solid, but rather has a granular structure like sand mixed with syrup, see Figure 4.8b. To completely resolidify the target it was placed in a freezer. This forces some of the Gallium to the surface creating spheres of Gallium as can be seen in Figure 4.8c.

Unlike the other targets, target 3 had not been cooled with running water before it was removed from crystal quartz vial and its structure can be seen in Figure 4.8d. Its structure was granular like a used target, but the solid flakes in the emulsion were larger than in a used target. After the first use, target 5 and 3 have the same structure as can be observed by comparing Figure 4.8b and 4.8e. If a target is used multiple times after use the target more and more becomes a uniform chunk of material. This can be

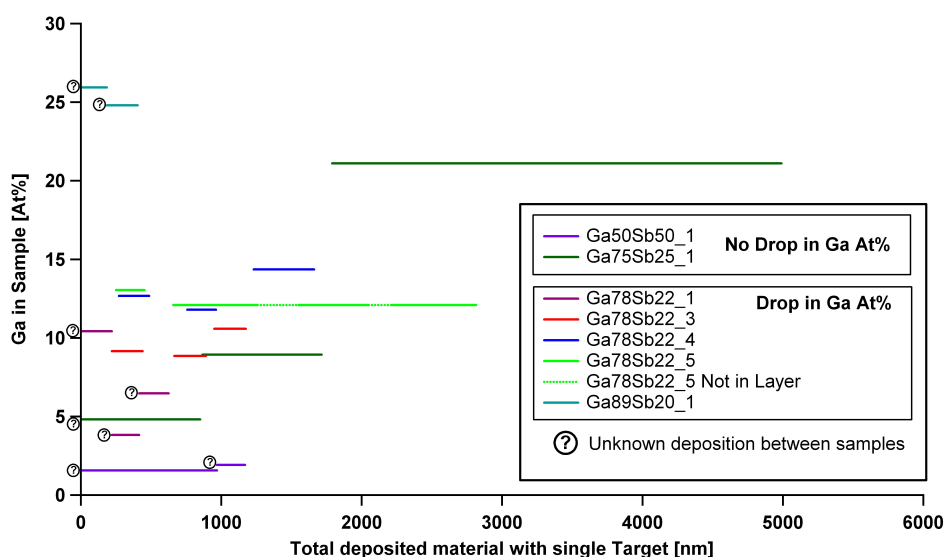


Figure 4.7: The Gallium content for the first two or three samples created with several targets are plotted against the amount on nanometres that have been deposited with said target. When it is unknown how much nm of target material had been deposited on the QCM crystal before the shutter was opened, it is preceded by a question mark.

seen by comparing Figure 4.8e, where there are some blobs of target material visible on the surface and Figure 4.8f. Target 3 has been used eight times in Figure 4.8f and there are almost no protrusions at the surface. This might possibly occur because the target composition changes to a more Gallium richer composition as it is used, See Figures 4.4 and 4.5¹³.

The change in target appearance can be linked to a drop in Gallium concentration in the deposited layer in the following manner. The way the electron beam evaporates the target material is at the heart of the explanation. The electron beam hits the the top or side of the target material in the case of first usage and thus melts and evaporates the target material. It zig-zags across the surface area of the crucible. The first time the target is used, it does not uniformly fill the the entire crucible. Since the outside of this target is rich in Gallium this allows for the creation of a crucible filled with liquid Gallium rich material with the remaining un-molten parts of the targets sticking out like icebergs. The electron beam zigzags over this Gallium rich mixture with un-molten target chunks. In this way more Gallium is evaporated than in the case where the target material uniformly fills the entire crucible i.e. all other occasions the target is used.

¹³As an analog the behaviour of sand and water could be used. When sand is mixed in a bucket with a little bit of water it will settle on the bottom of the bucket, but little chunks of sand can be seen on the surface. When enough water is added to the sand, the mixture will settle as a smooth granular paste



Figure 4.8: Figure 4.8a and 4.8d are targets 5 and 3 before use. Figures 4.8b and 4.8e show target 5 and 3 after use. Figure 4.8c shows the excreted Gallium droplet, which appears if the target is left in a freezer overnight. Figure 4.8f shows how continued use influences target appearance and structure.

The drop in Gallium concentration is less pronounced in the case of the samples created with target 3. Target 3 had not been cooled below room temperature before the first use and was thus better able to uniformly fill the crucible. The relatively large amount of Gallium on the outside of the target as can be seen in Figure 4.8d did allow for a Gallium drop to appear.

4.3.5 Discussion of the remaining unresolved observations.

Low Gallium concentration in sample 2 created with target 5

Sample 2 of target 5 has a thickness of 1950nm. Due to the observed Gallium drop, it is expected that the first few hundred nanometres that were deposited have a Gallium concentration that is slightly lower than the Gallium concentration in sample 1. After the first few hundred nanometres the Gallium concentration in the deposited layer will continuously increase. EDX over represents the first few hundred nanometres, but this does not provide a satisfactory explanation for the following reason. Sample 1 of target Ga78Sb22.2, henceforth known as target 2, has a thickness of 3000nm. The Gallium concentration of sample 1 of target 2 lies somewhere in the middle of between the Gallium concentration of sample 1 of target 3 and sample 8 of target 3, see Figure 4.9.

When the target is frozen after use¹⁴, Gallium is excreted to the surface of the target and forms spheres on the surface of the target, see Figure 4.8c. Small samples were taken from targets 3, 4, and 5 between evaporation sessions for future chemical analysis¹⁵. The granular paste-like structure of the target as it is removed from the e-beam evaporator sticks to tweezers among other things, making it difficult to obtain a representative sample. This is the reasons targets were frozen between evaporation sessions. The Gallium spheres were removed in all samples created with targets 4 and 5, which should result in a small decrease of the average Gallium concentration in the target. In the case of sample 1 made with target 5, the amount of actual target material is small in comparison with the size of the Gallium sphere, the resultant Gallium concentration decrease should therefore be a bit larger than in the other samples. This in turn could have led to a stronger drop in Gallium concentration during the first few hundred nanometres of deposition.

A last difference between sample 2 of target 5 and another thick sample; sample 8 of target 3, is that sample 3 was created with a continuous cycle of evaporation programs as mentioned earlier. In the creation of sample 2 of target 5, the layer and the target were allowed to cool down. Antimony is a notorious contaminant in thin film deposition systems operated in a high vacuum. Some Antimony may have evaporated from the belljar and made its way towards the sample surface during the cooldown sessions in between evaporation programs. All these factors combined might provide an explanation for the low measured Gallium concentration in sample 2 of target 5.

The difference in Gallium concentration in the deposited layers for targets with the same initial composition

The compositions of targets Ga78Sb22 1 through 5 is almost identical, see Table 4.1. The composition of the deposited layer of the first samples created with these targets is not, as can be seen in Figure 4.9. In Figure 4.9 the composition of all samples created with targets 1 through 5 is plotted against the total amount of nanometres that had been deposited with a certain target. Figure 4.9 has the same layout as Figure 4.7.

The composition of the first samples created with targets 4 and 5 is almost equal, although the Gallium concentration of the first sample created with target 5 is a bit higher than the first sample created with target 4. This can either be attributed to the random placements of the target pieces or to the fact that target 5 is was slightly heavier than target 4 before the first use, see Table 4.5.

¹⁴This has only been done for targets 4 and 5.

¹⁵The necessity for these samples was uncertain at the time, but they were taken as a precautionary measure.

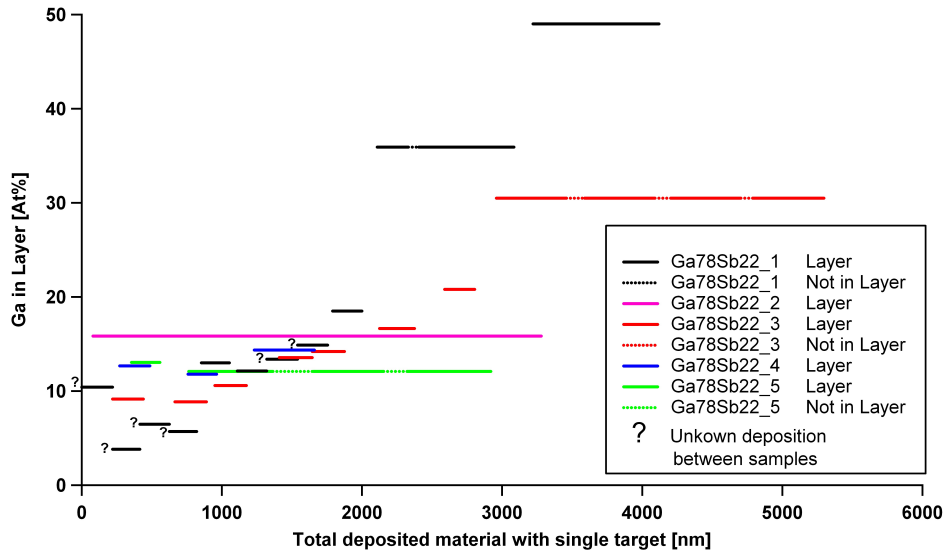


Figure 4.9: All samples created with targets of similar starting compositions. The composition of the first sample varies from target to target.

The first sample created with target 1 has a lower Gallium concentration than the first samples created with targets 4 and 5. Layer deposition rate was much lower in the case of the first sample created with target 1 in comparison with the layer deposition rate of the first samples created with targets 4 and 5. This could explain the difference in composition between these samples.

Layer deposition rate during the deposition of the first sample of target 3 was equal to the layer deposition rate during the creation of the first samples made with target 4 and 5, so this does not explain the lower Gallium concentration in the first sample created with target 3. Target 3 had not been cooled with water. This meant that a lot of target material stuck to the walls of the crystal vial. Since Gallium has the tendency to migrate to the surface of the target, the target material that stuck to the crystal vial could have been much richer in Gallium than the centre of the target.

The measured Gallium concentration in the first sample of target 2 is exactly what one would expect on the basis of comparison with the average of multiple samples created with targets 1 and 3.

4.4 Considerations in the creation of useful samples for isothermal annealing experiments and explosive crystallisation.

Before reading this section, it should be taken into account that some of the following conclusions only apply for the current experimental setup as described in chapter 3. When using different analysis tools these conclusions should be adjusted accordingly. The samples used in this research were made using e-beam evaporation. It has been shown earlier, that if the layer composition needs to be constant throughout the thickness of the layer, e-beam evaporation is not the most appropriate method to be used. Alternative methods could be Magnetron sputtering or pulsed laser deposition (PLD). Of course these methods are prone to have their own drawbacks as well; PLD is rather slow and therefore not suitable for the creation of thick layers and in the case of Magnetron sputtering, the deposited layer will contain impurities in the form of inert sputtering gases. In any future investigation of the kinetic properties of $\text{Ga}_x\text{Sb}_{100-x}$ samples the advantages, disadvantages and availability of the different deposition techniques should be re-evaluated.

4.4.1 Compositions useful for isothermal annealing experiments and explosive crystallisation

Figure 4.10 shows the crystal structures of samples with increasing Gallium concentration starting with pure Antimony crystals in Figure 4.10a up till a Gallium concentration of 25.94% in Figure 4.10f. The colours of the images are not due to the colouring of the crystals, but are the result of the use of various digital filtering techniques to make the crystal structure as clearly visible as possible.

The pure Antimony crystals shown in Figure 4.10a exhibit triangular symmetry. As the Gallium concentration is increased, the overall size to which the crystals can grow before the entire sample is crystallised is decreased, while the total amount of crystals is increased. The triangular structure becomes less and less pronounced, till it eventually disappears and circular crystals are created as can be seen in Figure 4.10f.

It is unclear what is the exact cause of the formed crystal structure. The crystal structure seen Figure 4.10d seems to deviate from a general trend visual in in Figure 4.10a through 4.10c in that circular rings and a separate core are visible. This might be caused by the fact the this particular sample had a thickness of 850nm, about 4 times the thickness of the other samples.

Figures 4.10a through 4.10d show a clear dendritic structure, while Figure 4.10e and 4.10f do not. The samples shown in these images were only partially crystallised, but the crystals shown in Figure 4.10e also seem to be able to grow to a much larger size as the crystals shown in Figures 4.10a

through 4.10d. Incidentally the sample shown in Figure 4.10e was the first sample where the sample had not fully crystallized during fabrication. The samples shown in 4.10a through 4.10d were fully crystallised when removed from the e-beam evaporator.

The sample shown in Figure 4.10e had composition $\text{Ga}_{10.42}\text{Sb}_{89.58}$ and although it was not fully crystallised when removed from the e-beam evaporator, small crystals were visible and they increased in size at room temperature albeit it be at a very slow rate. This means that the original goal of creating $\text{Ga}_x\text{Sb}_{100-x}$ samples with the same composition as the $\text{Ge}_x\text{Sb}_{100-x}$ analysed by Gert Eising is pointless, since they would have been crystallised at room temperature. For the amorphous layer to be effectively stable at room temperature it should have a Gallium concentration of at least 10.42%.

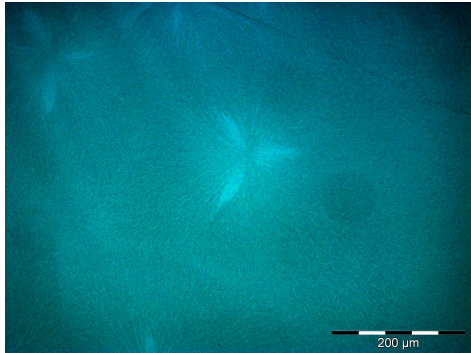
Average eventual crystal size at complete crystallisation of the sample seems to decrease with increasing Gallium concentration as can be seen from Figure 4.10e and 4.10f. Since the analyses of the isothermal crystallisation depends on edge detection techniques, there is an upper limit for the Gallium concentration in the sample in order for it to still be useful for isothermal analyses.

Figure 4.11 shows two images of two samples with different composition, but who are annealed at the same temperature. Not only do the crystals become smaller with increasing concentrations of Gallium, but also the contrast between amorphous and crystalline material seems to weaken. In Practice¹⁶, the upper limit for the Gallium concentration in a sample useful for isothermal analyses is 15%. The sample shown in Figure 4.11b had the highest concentration of Gallium for which it was still possible to analyse the growth process digitally.

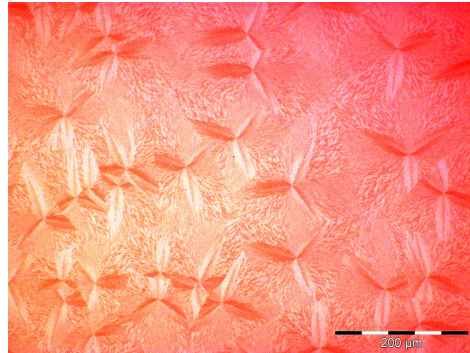
Figure 4.12 shows amorphous layers with ever increasing Gallium concentration. As the Gallium concentration is increased the amount of irregularities in layer is increased as well as can be seen from Figure 4.12a through 4.12c.

It will be shown that the increase in Gallium concentration is the main cause the increase of irregularities in the layer and other variables have little or no influence. Figure 4.12e has a thickness of 3000nm and has less irregularities than than the samples shown in Figure 4.12b and 4.12c. The sample shown in Figure 4.12e has more irregularities than the samples shown in Figure 4.12a, while it has a lower average Gallium concentration. This can be attributed to the fact EDX measures the average Gallium concentration, it is therefore possible that the Gallium concentration at the surface is higher than that of the layer shown in Figure 4.12a, or it could be explained by

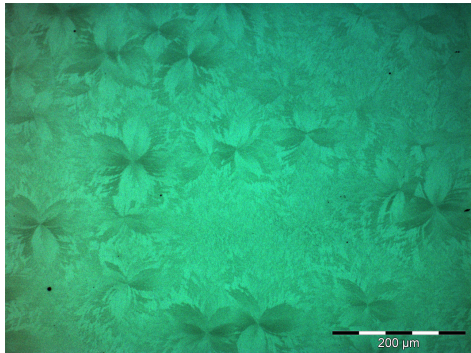
¹⁶Since E_n is larger than E_G [21], one could argue that it is only necessary to decrease the desired measurement temperature T . This allows for the crystals to grow larger in general and thus it should make edge detection possible again. Lowering T , however, will result in an exponential increase of the incubation time t_{Inc} , making this approach not very practical.



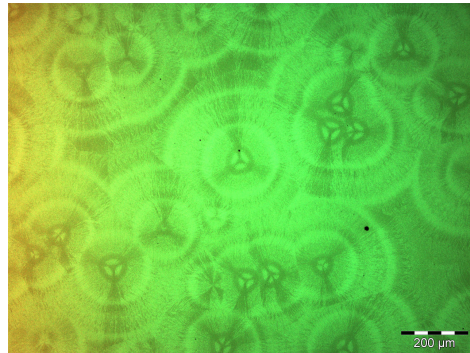
(a) Sample 1 from target Ga0Sb100_1. The sample has a thickness of 240nm and composition $\text{Ga}_0\text{Sb}_{100}$.



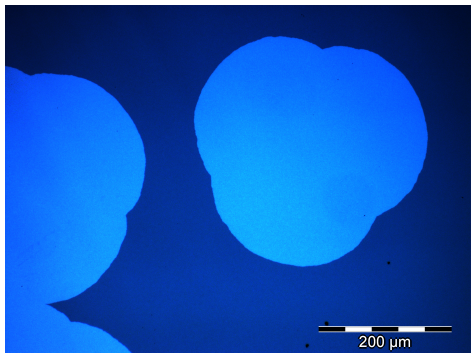
(b) Sample 2 from target Ga50Sb50_1. The sample has a thickness of 200nm and composition $\text{Ga}_{1.92}\text{Sb}_{98.08}$.



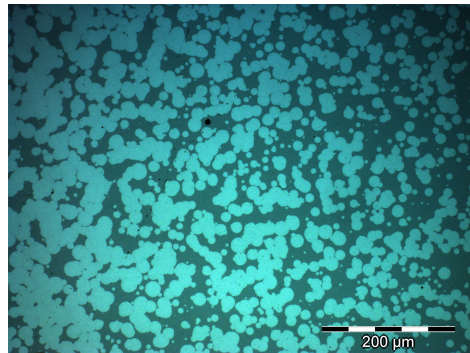
(c) Sample 1 from target Ga60Sb40_1. The sample has a thickness of 190nm and composition $\text{Ga}_{2.43}\text{Sb}_{97.57}$.



(d) Sample 1 from target Ga75Sb25_1. The sample has a thickness of 850nm and composition $\text{Ga}_{4.81}\text{Sb}_{95.19}$.

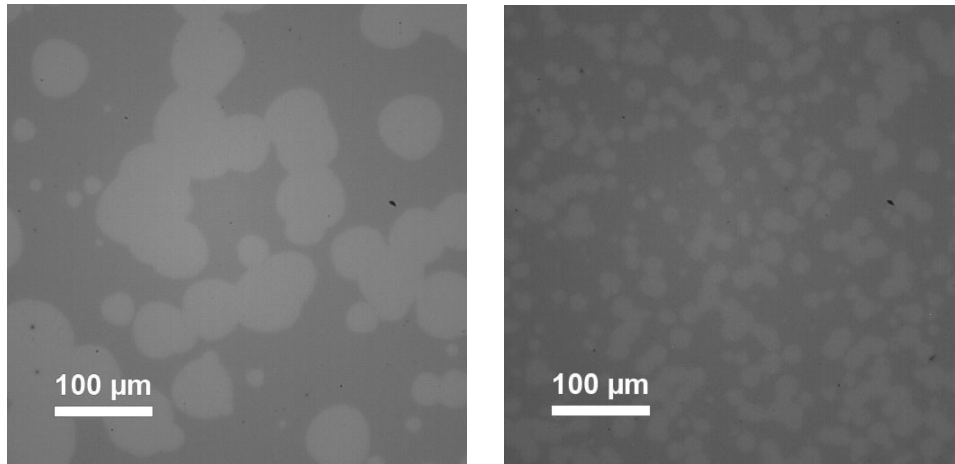


(e) Sample 1 from target Ga78Sb22_1. The sample has a thickness of 220nm and composition $\text{Ga}_{10.42}\text{Sb}_{89.58}$.



(f) Sample 7 made with target Ga78Sb22_1. The sample has a thickness of 180nm and composition $\text{Ga}_{13.38}\text{Sb}_{86.62}$.

Figure 4.10: Images of crystallised samples of $\text{Ga}_x\text{Sb}_{100}$, with various compositions. The sample with composition $\text{Ga}_{13.38}\text{Sb}_{86.62}$ shown in Figure 4.10f had been heated to 180°C and then brought back to room temperature.



(a) Sample $Ga_{11.79}Sb_{88.21}$ annealed at $130^{\circ}C$. Desired layer deposition rate was 1.50 nm/s .

(b) Sample $Ga_{14.89}Sb_{85.11}$ annealed at $130^{\circ}C$. Desired layer deposition rate was 0.60 nm/s .

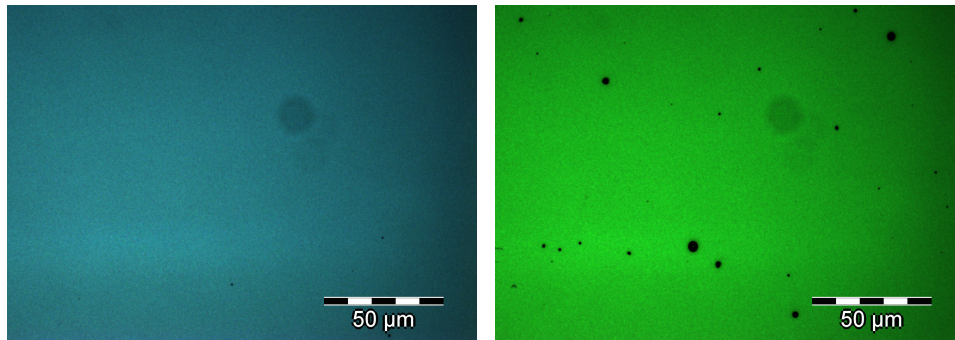
Figure 4.11: Comparison of crystallisation process between samples annealed at the same temperature, but with different composition.

assuming that the amount of irregularities does increase as the surface grows thicker. Figure 4.12f shows a layer with a thickness of 220nm , but with an amount of irregularities is equal to that of the sample shown in Figure 4.12e, higher than that of the surface shown in Figure 4.12a and lower than that of the surface shown in Figure 4.12b. Comparing layer deposition rates between samples, it is observed that the desired layer deposition rate with which the layer shown in Figure 4.12a was deposited is higher than the desired layer deposition rates with which the layers shown in Figures 4.12b, 4.12e, and 4.12f were deposited. This all corroborates to the conclusion that the amount of irregularities in the deposited layer is mainly determined by the composition of the target. Layer thickness and layer deposition rate are only of marginal influence.

The average Gallium concentration of sample 11 of target 1, whose layer is shown in Figure 4.12c, was 49.01% ¹⁷. Gallium droplets were visible on the surface of sample 12 of target 1 when it was removed from the e-beam evaporator as can be seen in Figure 4.12d. Based on the discussion on how the target material behaves, it is possible to assume that it is impossible to create samples with a Gallium concentration much larger than 50%. This puts an upper limit on the Gallium concentration in samples.

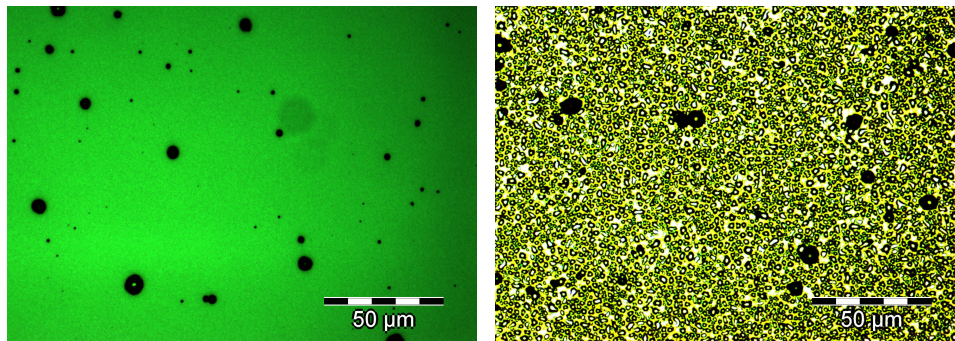
Using all the information presented above, the following conclusions can be made. To create an amorphous layer, the target needs to have a Gal-

¹⁷A scalpel was used to scrape material of the substrate and place it on the double sided carbon tape for EDX analysis in the SEM, so this value need not be an underestimation of the average Gallium concentration in the sample.



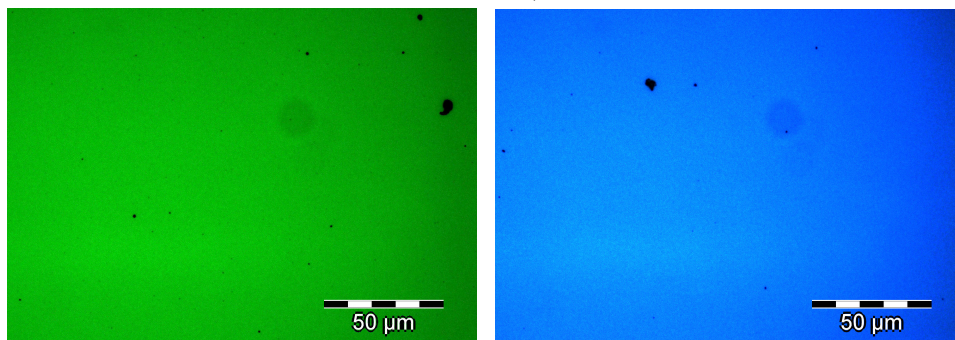
(a) Sample 9 of target Ga78Sb22_1: Sample thickness: 210 nm, composition: $Ga_{18.5}Sb_{81.5}$, desired layer deposition rate: 1.25 nm/s.

(b) Sample 10 of target Ga78Sb22_1: Sample thickness: 900nm, composition: $Ga_{35.92}Sb_{64.08}$ derived layer deposition rate: 0.82 nm/s.



(c) Sample 11 of target Ga78Sb22_1: Sample thickness: 900nm, composition: $Ga_{49.01}Sb_{50.99}$ desired layer deposition rate: 1.30 nm/s.

(d) Sample 12 of target Ga78Sb22_1: Sample thickness: 2400nm, based on Figure 4.6 Gallium concentration was above 50At%, desired layer deposition rate: 1 nm/s.



(e) Sample 1 of target Ga78Sb22_2: Sample thickness: 3000nm, composition: $Ga_{15.84}Sb_{84.16}$ derived layer deposition rate: 0.26 nm/s.

(f) Sample 1 of target Ga80Sb20_1: Sample thickness: 220nm, composition: $Ga_{25.94}Sb_{74.06}$ desired layer deposition rate: 0.2 nm/s.

Figure 4.12: Comparison between layer smoothness of different samples on the basis of composition, thickness and layer deposition rate.

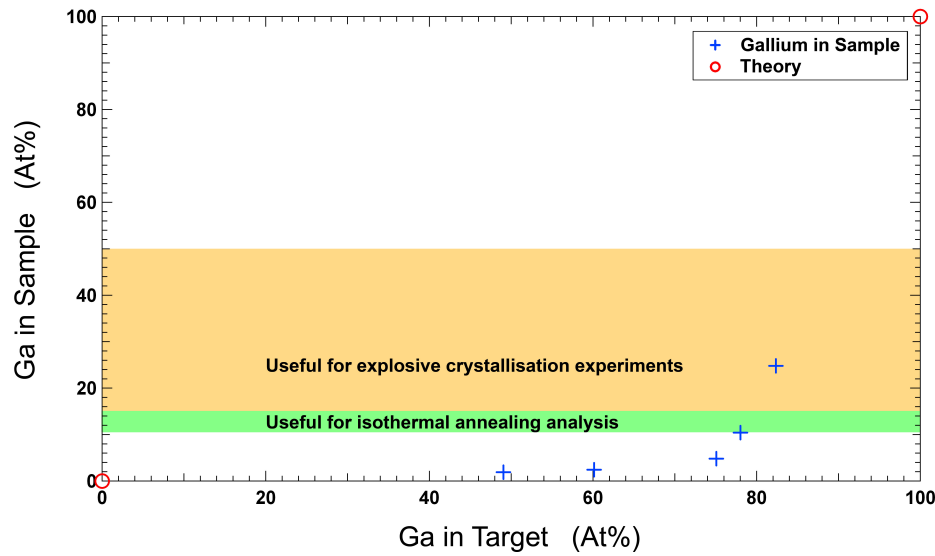


Figure 4.13: Target composition against first sample composition, where the two regions indicate samples that might be used for isothermal annealing analysis and explosive crystallisation experiments respectively.

lium concentration of at least for 78At%. If the sample has a Gallium concentration above 15At%, using the current experimental setup, its kinetic properties can no longer be analysed using isothermal growth analysis. The relation between target composition and sample composition is again plotted in Figure 4.13. This time accompanied with bands indicating the range suitable for isothermal growth analysis and for explosive crystallisation experiments. From Figure 4.13 it can be determined that target composition needs to be between $Ga_{78}Sb_{22}$ and $Ga_{80}Sb_{20}$ in order to create samples useful for isothermal growth analysis using the current experimental setup.

Using the composition of the samples created with target 3 it is possible to make an estimation of the maximum thickness of a sample that can be used for isothermal growth analyses, the maximum thickness of a smooth sample, and the maximum thickness of a sample useful for explosive crystallisation. From Figure 4.14 we can determine that the maximum thickness for isothermal growth analysis lies between 900 and 1000 nm, the maximum thickness for a smooth surface lies between 1500nm and 1600nm, and the maximum thickness of a sample useful for explosive crystallisation analysis lies above 4000nm

Multiple targets can be placed in the Varian 3120 e-beam evaporator, but this would introduce a sudden shift in composition instead of a continuous increase in Gallium concentration. The effect of this sudden shift and for that matter the effect of the continuous increase in Gallium concentration on the crystallisation kinetics of the layer is unknown.

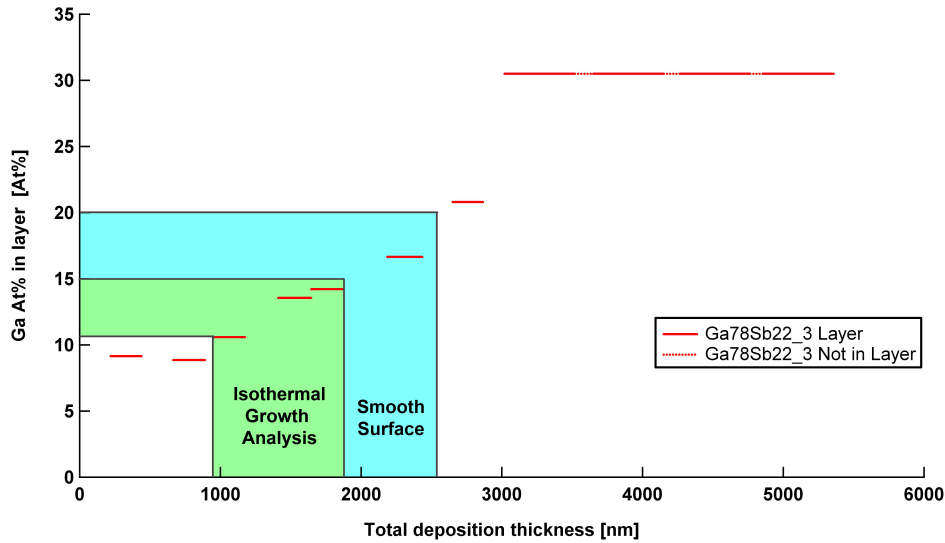


Figure 4.14: Maximum thickness that can be attained for a sample that can be analysed during isothermal annealing experiments is approximately 900nm, based on the information of the samples created with target 3.

During the e-beam evaporation process not only the target is heated, but indirectly the substrate surface is heated as well. The layer shown in Figure 4.12e was crystalline when removed from the e-beam evaporator. There was no thermometer attached to the substrate, but its temperature was approximately 50°C . The derived layer deposition rate for the sample shown in Figure 4.12e was 0.26 nm/s . It was assumed that an increase in layer deposition rate would be able to decrease the temperature of the substrate during the evaporation process. In this manner sample 8 of target Ga78Sb22.3 was created with a derived evaporation speed of 1.70 nm/s . This indeed reduced the temperature of the substrate substantially, but sample 8 of target Ga78Sb22.3 was still crystalline. Sample 2 of target Ga78Sb22.5 was created in a similar manner, but every few hundred nanometres the e-beam evaporator would be turned off. The sample would remain in vacuum and after letting the sample cool for more than half an hour, the next few hundred nanometre would be deposited. This sample was amorphous. It did not show explosive crystallisation behaviour. However, its properties were investigated one year after its creation date.

A tensile strain was observed when sample 1 of target Ga50Sb50.1 was cut into smaller fragments for further analysis. As can be seen in Figure 4.15 the thick 970nm layer with a composition of $Ga_{1.56}Sb_{98.44}$ detached itself from the glass substrate and rolled in on itself. This indicates the existence of tensile stresses across the deposited layers. Layers of 200nm did not detach themselves from the glass substrate, when the larger 3mm x 3mm samples were broken into smaller segments. Since tensile strain had a



Figure 4.15: Attempt at cutting the first sample created with target $\text{Ga}_{50}\text{Sb}_{50.1}$.

large effect on the crystallisation speed in the $\text{Ge}_x\text{Sb}_{100-x}$ samples analysed by Gert Esing [22], it is useful to know that it is there when reading the next two chapters detailing the kinetic properties of the deposited layers.

Using e-beam evaporation for the creation of amorphous thick layers is thus only an option if varying composition throughout its thickness is not a concern, or if this is a desired property.

4.4.2 Recommendations for target creation

To create amorphous samples it is recommended to use a target with a starting composition of $\text{Ga}_{78}\text{Sb}_{22}$, because it produces amorphous layers, whose growth properties can be easily analysed using the current experimental setup (when the films are deposited on Si-nitride membranes growth of much smaller crystals can be monitored and then higher Ga concentrations are allowed). Some recommendations for the creation of future targets are in order. Many irregularities in the obtained sample composition can be traced back to the physical shape of the target as it is placed in the e-beam evaporator. Although the risk for external contaminants is increased, it is recommended to make target pellets with the exact shape of the crucible and with the same starting weight. The change in sample composition is caused by weight loss and targets with different starting weights will be effected differently with the same the same weight loss.

This approach should get rid of the drop in Gallium concentration during the first few hundred nanometres of deposition and should allow for a more accurate prediction of sample composition on the basis of target composition.

¹⁸Only for samples $\text{Ga}_{10.42}\text{Sb}_{89.58}$ and $\text{Ga}_{12.67}\text{Sb}_{87.33}$ show a derived evaporation speed. All other speeds are desired evaporation speeds.

Samples used for isothermal crystallisation analysis						
Sample Composition		Target Name	Sample Number		Layer Thickness	Deposition Speed ¹⁸
Ga At%	Sb At%		From Target	Ga ₇₈ Sb ₂₂ Total	d (nm)	v (nm/s)
10.42	89.58	Ga78Sb22.1	1	1	220	0.14
11.79	88.21	Ga78Sb22.4	2	24	210	1.50
12.14	87.86	Ga78Sb22.1	6	6	210	0.75
12.67	87.33	Ga78Sb22.4	1	23	215	1.24
13.00	87.00	Ga78Sb22.1	5	5	200	1.00
13.38	86.62	Ga78Sb22.1	7	7	220	0.50
14.89	85.11	Ga78Sb22.1	8	8	215	0.60

Table 4.7: Samples used in the isothermal annealing experiments described in the next chapter.

4.4.3 Samples analysed with isothermal experiments.

This research started with two goals in mind. One was the creation of thick amorphous layers of $\text{Ga}_x\text{Sb}_{100-x}$ to record explosive crystallisation using a high speed camera. The second was to create samples of $\text{Ga}_x\text{Sb}_{100}$ with the same composition as the $\text{Ge}_x\text{Sb}_{100-x}$ samples analysed by Gert Eising (Publication submitted 23-07-2013). These had composition $\text{Ge}_6\text{Sb}_{94}$, $\text{Ge}_7\text{Sb}_{93}$, $\text{Ge}_8\text{Sb}_{92}$, and $\text{Ge}_9\text{Sb}_{91}$.

In Table 4.7 the properties of the samples used for isothermal growth analyses described in the next chapter are summarized. Target name and sample number are mentioned for archival reasons. The $\text{Ga}_{78}\text{Sb}_{22}$ sample number is the sequential number with which a sample was created using targets Ga78Sb22.1 through Ga78Sb22.5. This number and other information has been written down on the containers holding the actual samples.

The reasons for analysing these specific samples out of all samples mentioned in this chapter are historic and therefore might not have been the most logical choice from a scientific perspective. The main difference between the samples apart from their composition is the speed with which the layer was deposited on the substrate.

Chapter 5

Isothermal Heating Experiments

In selecting and developing a material that is suitable to be used as non-volatile random access memory, it is important to know the kinetic behaviour of the material across temperature and time. When it is possible to use the Arrhenius relation and isothermal Avrami equations, described in sections 2.1 and 2.2, to describe the kinetics properties of a material, its kinetics can be described in terms of several physical quantities. These are: the growth activation energy E_g , the nucleation activation energy E_n , The growth rate at infinite temperature A , and the dimensionless constant K governing the the relationship between the probability of activation of a germ nucleus per unit time n and temperature T . In practice practice A and K are difficult to determine accurately with isothermal heating experiments. The relation between the growth rate G and temperature T and the relation between the probability of activation of a germ nucleus per unit time n and temperature T , are used to obtain the aforementioned physical quantities. Then the Avrami equations themselves can be used to check if this is a valid approach to determine the kinetic properties of the material. In the last two chapters it was explained how several $\text{Ga}_x\text{Sb}_{100-x}$ with various compositions and a thicknesses of 200nm were created using e-beam evaporation. In chapter 3 it was explained how the $\text{Ge}_x\text{Sb}_{100-x}$ samples used by Gert Eising in isothermal heating experiments were created.

In this chapter the physical quantities mentioned above will be derived using isothermal heating experiments as described in chapter 3 on the basis of the theory described in chapter 2. The growth and nucleation activation energies E_g and E_n are derived for the $\text{Ga}_x\text{Sb}_{100-x}$ samples. The growth activation energy E_g will be derived by assuming that the relation between the growth rate G and temperature T can be described by means of an Arrhenius relation. The nucleation activation energy E_n can be derived by assuming that the transformation process from amorphous to crystalline can

be described in terms of isothermal Avrami equations.

After the kinetic physical quantities for the $\text{Ga}_x\text{Sb}_{100-x}$ samples have been determined, the growth activation energy E_g and the relation between G and T will also be described for the $\text{Ge}_x\text{Sb}_{100-x}$ samples. It will be shown that the Arrhenius relation is able to accurately describe the relation between G and T of the $\text{Ge}_x\text{Sb}_{100-x}$ samples, but that this only applies to a lesser extent for the $\text{Ga}_x\text{Sb}_{100-x}$ samples.

To get a better insight to what extent the isothermal Avrami equations are able to describe transformation process from amorphous to crystalline, the three models for 2 dimensional growth presented in chapter 2 in equations 2.28, 2.29 and 2.30 will be fitted to measurement data obtained of the crystallisation process of $\text{Ga}_{11.79}\text{Sb}_{88.21}$ at 100°C .

5.1 Determination of kinetic constants based on Avrami's theory.

5.1.1 Determination of growth energy E_g and nucleation energy E_n

In chapter 2 it was mentioned that the Arrhenius equation (equation 2.1) can be used to describe the relation between the growth rate G of a growing crystal and the growth activation energy E_g . Plotting $\ln(G)$ against $1/k_B T$ will result in a straight line whose slope results in the growth activation energy E_g and the constant A , representing the growth rate at a theoretical infinite temperature, can be determined by the offset. This is an Arrhenius plot. A is a measure for the amount of collisions per unit of time that occur at the boundary of the crystal and the jump distance that the atoms have to traverse between the amorphous boundary and the crystal boundary that could result in crystal growth, while $e^{-\frac{E_g}{k_B T}}$ is a measure for how many of these collisions are successful.

Growth rate measurements have been performed for samples of $\text{Ga}_x\text{Sb}_{100-x}$ with various compositions at various temperatures. The results of these isothermal growth rate measurements are depicted in an Arrhenius plot in Figure 5.1. The derived values for the growth activation energy E_g and constant A can be found in Table 5.1.

If the relation between growth rate G and temperature T could perfectly be described as an Arrhenius relation, the the measured values for G at various temperatures would lay in a straight line in Figure 5.1. This is the case for sample $\text{Ga}_{10.42}\text{Sb}_{89.58}$, but not for every other sample. The samples that most notably deviate from a standard Arrhenius relation, are samples $\text{Ga}_{11.79}\text{Sb}_{88.21}$ and $\text{Ga}_{12.67}\text{Sb}_{87.33}$. At temperatures of 105°C and lower, the measured growth rates are higher then one would expect extrapolating from a linear fit taken through the measurement points above 105°C . The largest

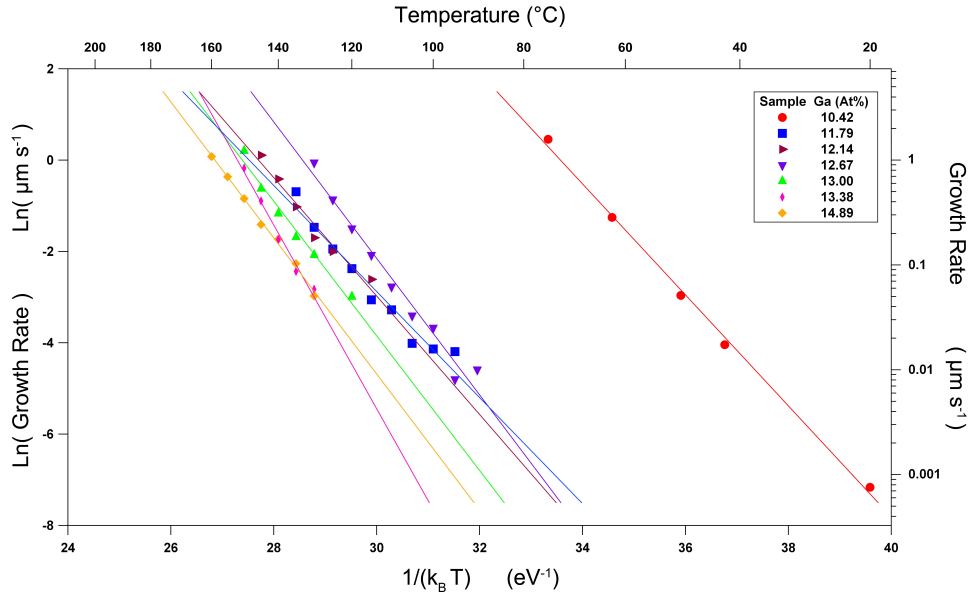


Figure 5.1: Arrhenius plot of $\text{Ga}_x\text{Sb}_{100-x}$ samples with various compositions. The slopes of the linear fits are a measure for the growth activation energy E_g in eV and they can be found in Table 5.1.

discrepancy between measurement and the Arrhenius relation can be seen for the measured growth rates of sample $\text{Ga}_{12.67}\text{Sb}_{87.33}$ at temperatures 95°C and 100°C . The measured growth rate at 95°C is higher than that at 100°C .

The measurements in Figure 5.1 are based on the top of a Histogram of all measured growth rates during the transformation process from amorphous to crystalline. The error is approximated by the full width half maximum (FWHM). A typical example of such a histogram can be found further in this report in Figure 5.11. For clarity's sake, the FWHM values around the measurement points are not shown in Figure 5.1. The linear fits through the measurement points fall within these boundaries, therefore the measurements which seem to deviate from an Arrhenius relation are included in the linear fits shown in Figure 5.1

The probability of activation of a germ nucleus into a growth nucleus per unit time n , was given in chapter 2 in equation 2.3. n can be estimated using the incubation time as shown in equation 2.33. Plotting $\ln(1/t_{Inc})$ against $1/k_B T$ will result in a straight line, whose slope will be equal to $(Q+A(T))$, where Q is the true energy of activation and $A(T)$ is the work required for forming a growth nucleus at temperature T (Not to be confused with constant A of the Arrhenius relation).

It is assumed the measurements are performed in the isokinetic range. In isothermal annealing experiments in the isokinetic range of a material it is impossible to distinguish between Q and $A(T)$ and $(Q+A(T))$ is constant.

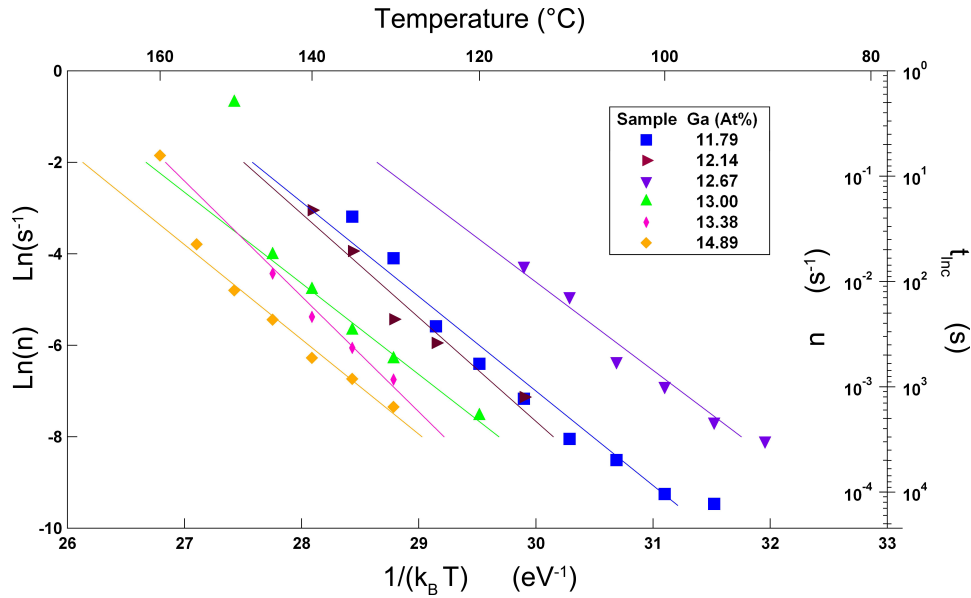


Figure 5.2: $\ln(n)$ is depicted against $1/k_B T$, for samples of $\text{Ga}_x\text{Sb}_{100-x}$ with various compositions. The slopes of the linear fits are a measure for the nucleation activation energy E_n in eV and they can be found in Table 5.1.

Therefore $(Q+A(T))$ is defined in this report as the nucleation activation energy E_n . The offset can be used to determine the constant K . Results of the incubation time measurements are shown in Figure 5.2. The results of the linear fits can be found in Table 5.1.

In theory the incubation time is defined as the time that it takes for the first crystal to appear under isothermal conditions. In practice it is defined as the time it takes from the moment the desired temperature is reached till the first crystal appears. It takes time to heat a sample to its desired temperature. During this time the sample is already influenced, and the measured incubation times are a shorter then they would be in a perfect instant isothermal scenario. Because of this effect, incubation times of less then 10 seconds are not taken into account in the linear fits through the measurement data in Figure 5.2.

Apart from an underestimation of the incubation time at higher temperatures measured for a certain sample, a second thing to notice is that the incubation times for samples $\text{Ga}_{11.79}\text{Sb}_{88.21}$ and $\text{Ga}_{12.67}\text{Sb}_{87.33}$ at temperatures 105°C and less appear to be shorter then expected if one would make a linear fit though the data points of 105°C and above. Since there is no physical reason to ignore these measurement points, they are part of the linear fit presented in Figure 5.2.

Growth and nucleation activation energy; E_G and E_n					
Sample	Symbol	$G = Ae^{\frac{-E_G}{k_B T}}$		$n = Ke^{\frac{-E_n}{k_B T}}$	
	Figure 5.1	E_G (eV)	A (m·s ⁻¹)	E_n (eV)	K (s ⁻¹)
Ga _{10.42} Sb _{89.58}	●	1.21 eV	$5.1 \cdot 10^{11}$		
Ga _{11.79} Sb _{88.21}	■	1.16 eV	$7.5 \cdot 10^7$	2.07 eV	$7.4 \cdot 10^{23}$
Ga _{12.14} Sb _{87.86}	▶	1.29 eV	$3.9 \cdot 10^9$	2.27 eV	$1.8 \cdot 10^{26}$
Ga _{12.67} Sb _{87.33}	▼	1.49 eV	$3.4 \cdot 10^{12}$	1.93 eV	$1.4 \cdot 10^{23}$
Ga _{13.00} Sb _{87.00}	▲	1.47 eV	$3.4 \cdot 10^{11}$	1.99 eV	$1.6 \cdot 10^{22}$
Ga _{13.38} Sb _{86.62}	◆	2.01 eV	$6.7 \cdot 10^{17}$	2.52 eV	$3.4 \cdot 10^{28}$
Ga _{14.89} Sb _{85.11}	◇	1.49 eV	$2.3 \cdot 10^{11}$	2.07 eV	$4.4 \cdot 10^{22}$
	Figure 5.3				
Ge ₆ Sb ₉₄	●	1.7 eV	$9.4 \cdot 10^{15}$		
Ge ₇ Sb ₉₃	■	2.1 eV	$9.3 \cdot 10^{20}$		
Ge ₈ Sb ₉₂	▲	2.7 eV	$1.9 \cdot 10^{57}$		
Ge ₉ Sb ₉₁	▶	5.7 eV	$7.9 \cdot 10^{51}$		

Table 5.1: Table with the derived nucleation activation energies E_n , growth activation energies E_g , and constants A and K for both samples of $\text{Ge}_x\text{Sb}_{100-x}$ and $\text{Ga}_x\text{Sb}_{100-x}$.

5.1.2 A comparison with $\text{Ge}_x\text{Sb}_{100-x}$ samples

Gert Eising has performed growth rate measurements on samples of $\text{Ge}_x\text{Sb}_{100-x}$ (Publication submitted). The Arrhenius plots of these measurements can be seen in Figure 5.3. The determined growth activation energies E_g are depicted next to their respective linear fits and the growth activation energies E_g and constants A can also be found in Table 5.1. For the $\text{Ge}_x\text{Sb}_{100-x}$ samples, the relation between G and T corresponds more to an Arrhenius relation, than the relation between G and T of the $\text{Ga}_x\text{Sb}_{100-x}$ samples.

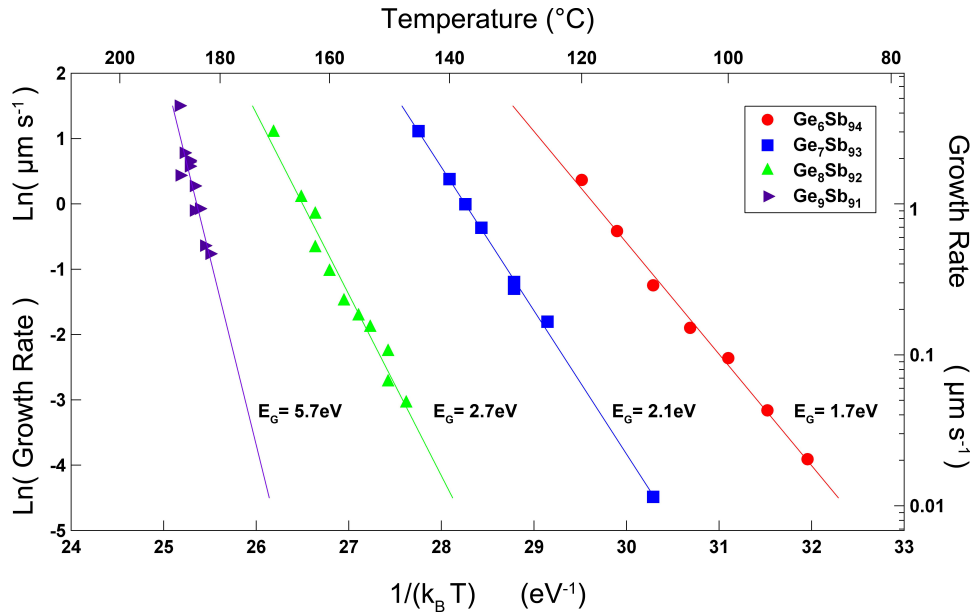


Figure 5.3: Arrhenius plots for samples of $\text{Ge}_x\text{Sb}_{100-x}$ with various compositions. The slopes of the linear fits are a measure for the growth activation energy E_g in eV and they can be found in Table 5.1.

From Figure 5.1 it appears that as the amount of Gallium in the sample is increased, higher temperatures are needed to achieve the same growth rate. This would indicate that increasing the Gallium concentration in the sample makes it more stable. One outlier in the trend is $\text{Ga}_{12.67}\text{Sb}_{87.33}$, which appears to be less stable than $\text{Ga}_{11.79}\text{Sb}_{88.21}$ and $\text{Ga}_{12.14}\text{Sb}_{87.86}$. A same tendency can be seen for the $\text{Ge}_x\text{Sb}_{100-x}$ samples, but it is much more pronounced than in the case of the $\text{Ga}_x\text{Sb}_{100-x}$ samples. To give a better overview of difference of the effect that doping with Germanium has in comparison with doping with Gallium, the isothermal growth rate measurements of both sample types have been plotted in Figure 5.4.

From Figure 5.4 we can see that Germanium has a much stronger influence on the crystallisation growth rate than Gallium. Roughly twice the amount of Gallium is necessary to achieve the same amount of stability shift as for Germanium.

An ideal material for memory applications is very stable up to a certain temperature followed by an abrupt increase in growth rate for a minor increase in temperature. By examining the Arrhenius equation 2.1, one can observe that a change in A will cause a shift in the straight line of a Arrhenius plot, but it will not affect the slope of the line. The slope of the line can only be changed by a change in E_g . The stability of a material can thus be increased by either decreasing A , which is a measure for the amount of collisions that occur that could result in crystal growth, and/or increasing E_g ,

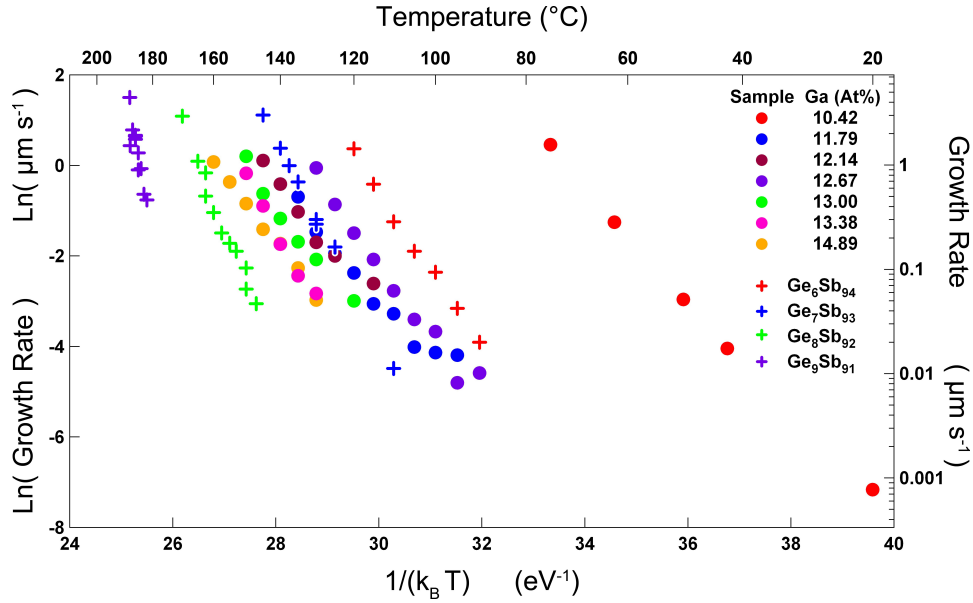


Figure 5.4: $\ln(G)$ is depicted against $1/k_B T$, for films with a $\text{Ge}_x\text{Sb}_{100-x}$ and $\text{Ga}_x\text{Sb}_{100-x}$ composition.

decreasing the probability that any collision would result in crystal growth. In an Arrhenius plot, an increase in E_g can also be interpreted as a rotation around a point on the $\ln(G)$ axis determined by A . Depending on the range of the axis in an Arrhenius plot, a change in E_g can appear not only to change the slope of the plot, but also to a shift to the left. If a material needs to operate in a certain temperature range, it is not enough to simply increase E_g , but A needs to be adjusted accordingly. This means that to make the change in growth rate as large as possible for a small temperature interval, E_g needs to be as high as possible. However, A needs to be adjusted to determine the temperature range in which the material is supposed to operate.

Using the remarks above, the data presented in Figures 5.1, 5.4, 5.3 and Table 5.1 can be used to compare the $\text{Ge}_x\text{Sb}_{100-x}$ with the $\text{Ga}_x\text{Sb}_{100-x}$ samples. A first observation is that when the Germanium content of a sample is increased, E_g is increased as well, while such a strong relationship does not appear to exist for the $\text{Ga}_x\text{Sb}_{100-x}$ samples. To make difference more visible E_g and E_n are plotted against the At% Germanium/Gallium content of the samples in Figure 5.5.

One hypothesis for explaining the increase in stability of the samples with increasing Germanium and Gallium concentrations, could be that an Antimony crystal is formed and that Germanium and Gallium reduce the amount of collisions that occur between the Antimony atoms which could result in crystal growth, effectively decreasing A . In this hypothesis E_g

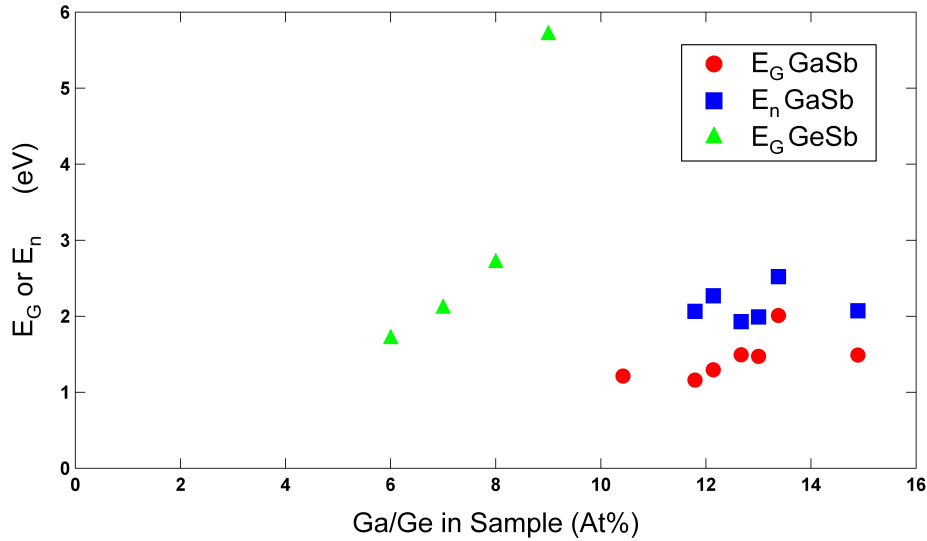


Figure 5.5: Growth activation energies E_g and nucleation activation energies E_n , for samples of $\text{Ge}_x\text{Sb}_{100-x}$ and $\text{Ga}_x\text{Sb}_{100-x}$.

would not be affected, since the same crystal structure would be formed. Only the amount of opportunities for it to form is decreased.

This is in direct contradiction with the data presented for the Germanium samples in Table 5.1 and Figure 5.5, because A increases for the Germanium samples as the Germanium concentration increases. This means that instead of treating Germanium as a simple inhibitor of growth an opposite hypothesis could be raised, namely that Germanium is part of the formed crystal structure. A second observation that supports this hypothesis is the increases in E_g for samples $\text{Ge}_6\text{Sb}_{94}$, $\text{Ge}_7\text{Sb}_{93}$, and $\text{Ge}_8\text{Sb}_{92}$, which could be an indication that different crystal structures are formed.

It is more difficult to compose such an unambiguous hypothesis in the case of the $\text{Ga}_x\text{Sb}_{100-x}$ samples. Figures 5.1, 5.2, and 5.5 provide very little evidence that an increase in Gallium concentration corresponds with an increase in E_g or E_n , nor can the opposite claim be made that an increase in Gallium does not lead to an increase in E_g or E_n . Several things might be the cause of this lack of coherence in the measurement results. EDX measurements across the sample surface indicate that the Gallium concentration is not completely uniform across the sample surface. The evaporation speed was not equal for all created samples. Finally, Arrhenius kinetics seemed to describe the growth kinetics of the material to a much lesser extent as in the case of the Germanium samples.

Considering all these facts, the most likely hypothesis on the basis of Figures 5.1, 5.2, and 5.5 is that Gallium has little influence on E_g , and therefore is not part of the crystal structure, but works as an inhibitor of

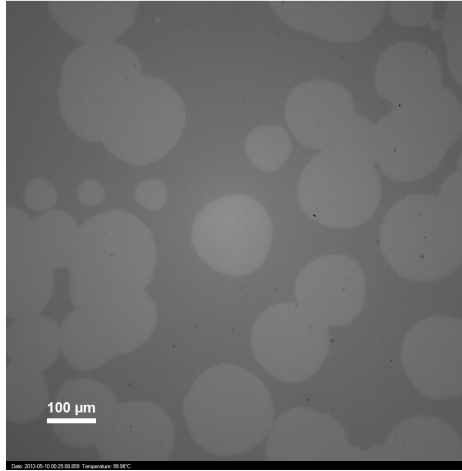


Figure 5.6: Crystals for sample $\text{Ga}_{11.79}\text{Sb}_{88.21}$ at 100°C at time $t = 14655\text{s}$ of the transformation process. The crystals have an almost circular shape.

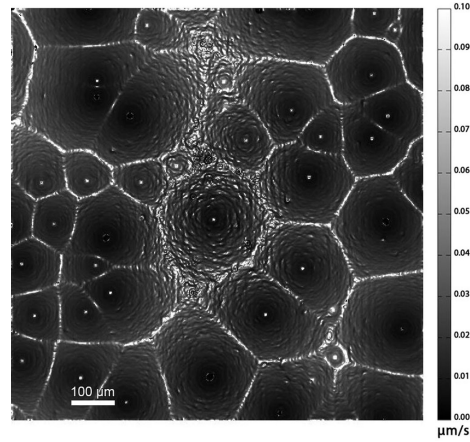


Figure 5.7: Growth rate map of the transformation process of $\text{Ga}_{11.79}\text{Sb}_{88.21}$ at 100°C . Crystal centres are visible as white dots or black circles. There are approximately 40 crystals.

crystal growth. This is not supported by a uniform decrease in A for increasing Gallium concentration, see Table 5.1, but it is based on the unambiguity of the change in E_g and E_n presented in Figure 5.5 and the general trend of the material properties observed in Figure 5.1.

Summarizing the above. Germanium appears to be a better stabilizer of the amorphous phase than Gallium, because there is a strong increase in E_g , but the material still operates in more or less the same temperature range. The hypothesis to explain this difference is that Germanium is part of the formed crystal structure, while Gallium acts as a growth inhibitor. This needs to be verified with future research.

5.1.3 A comparison with Avrami theory

The measured growth of the $\text{Ga}_x\text{Sb}_{100-x}$ films deviates from the predicted Arrhenius relation at the lower end of the measured temperature range. Higher growth rates are measured than would be expected. At this lower end of the measured temperature range, the incubation times seem to be shorter than would be expected from isothermal Avrami relations.

Equations 2.28, 2.29 and 2.30 from chapter 2 presented three relations that could describe the isothermal transformation process from amorphous to crystalline in two dimensions. Equation 2.28 represents a general model, equation 2.29 is an approximation of equation 2.28 for large values of n , and equation 2.30 is an approximation of equation 2.28 for small values of n .

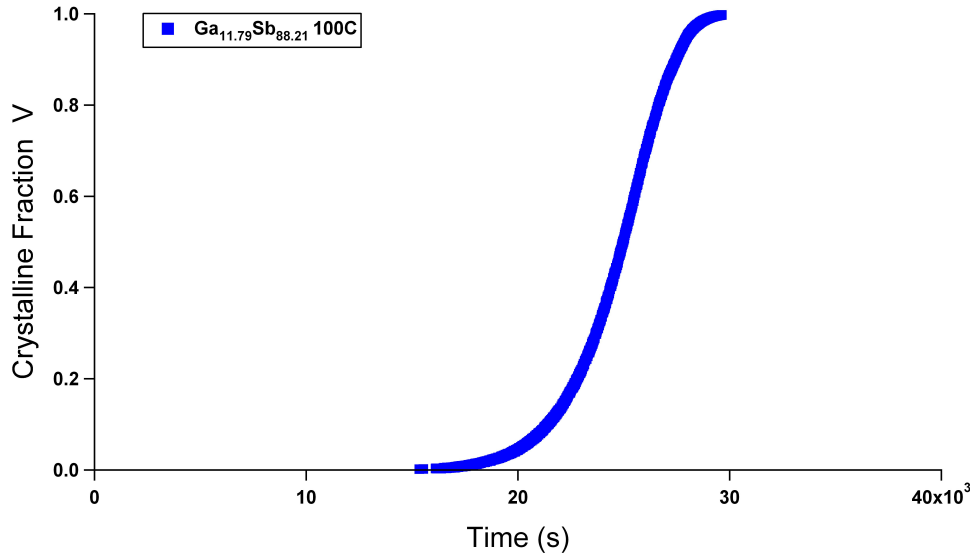


Figure 5.8: Crystalline Fraction V against time (s).

In this section it will be attempted to fit these models to the acquired measurement data obtained at at 100°C from a sample with composition $\text{Ga}_{11.79}\text{Sb}_{88.21}$. The crystals formed in this sample were large in comparison with the crystals formed during the crystallisation process for samples with a higher Gallium concentration, see Figure 5.6. The crystallisation process took a little under 5 hours to complete. The growth of individual crystals could thus be accurately tracked, see Figure 5.7. It is the first measurement point that starts to deviate from the assumed Arrhenius relation. At the end of this section it will be shown that crystallisation process can not be explained with a standard isothermal Avrami relation.

The measured transformation curve is presented in Figure 5.8. The approximations for G , n , σ , and N are based on the measurements presented in the last section. For a sample with composition $\text{Ga}_{11.79}\text{Sb}_{88.21}$ at 100°C the growth rate is equal to $G = 0.016\mu\text{m}\cdot\text{s}^{-1}$.

The approximation used in the previous sections for n was based on the observed incubation time t_{Inc} . This was based on the assumption as the first crystal appears, the crystalline fraction will start to deviate from 0 and that this corresponds with the moment that $\tau = n \cdot t$ starts to deviate from 1. This allows for the approximation $n = \frac{1}{t_{Inc}}$. For sample $\text{Ga}_{11.79}\text{Sb}_{88.21}$ at 100°C $t_{Inc} \approx 10 \cdot 10^4\text{s}$. Figure 5.8 shows that the crystalline fraction starts to deviate from zero 6000 seconds after the first crystal is observed. This behaviour of the material is not expected on the basis of standard isothermal Avrami equations. n will be adjusted based on the data in Figure 5.8. The approximation for n used in the fits below is $n \cong 1/(t_{Inc}+6000) \approx 6 \cdot 10^{-5}\text{s}^{-1}$.

The crystals have an almost circular shape, see Figure 5.6, therefore the

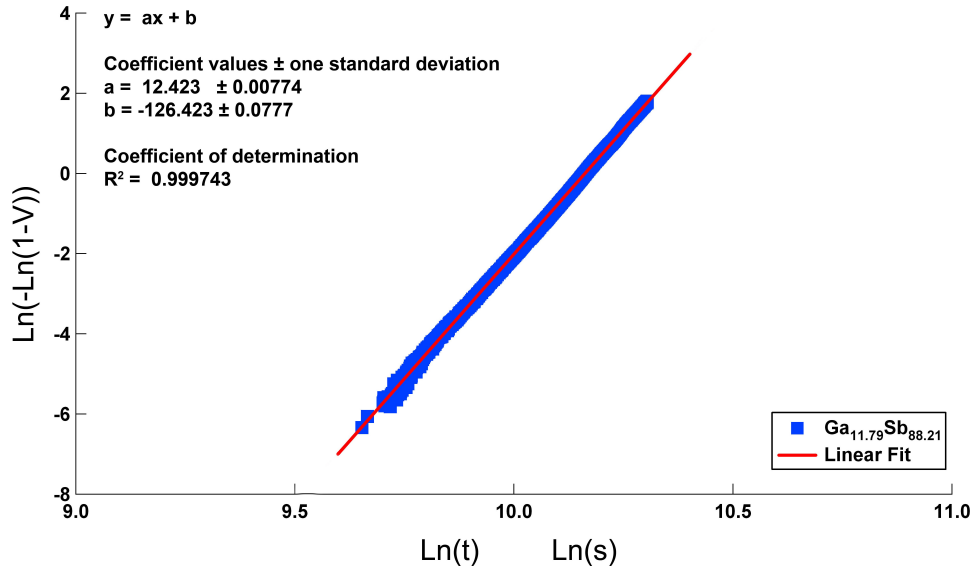


Figure 5.9: Avrami plot and fit for $\text{Ga}_{11.79}\text{Sb}_{88.21}$ at 100°C with linear fit.

shape factor σ is assumed to be π . At the end of the transformation process approximately 40 germ nuclei, see Figure 5.7, had been activated to form growth nuclei. This means although we do not know N , any meaningful fit needs to give a value for N greater than 40.

Using equations 2.28, 2.29 and 2.30 from Chapter 2 and the approximations for G , n and σ given above, the following equations will be fitted to the measurement data. The general relationship between the transformed volume V and the kinetic properties of the material is given by

$$V = 1 - e^{-2\bar{N}\pi \left[\frac{1.6 \cdot 10^{-2} \mu\text{m}/\text{s}}{6 \cdot 10^{-5} \text{s}^{-1}} \right]^2 \left[e^{-6 \cdot 10^{-5} \text{s}^{-1} \cdot t} - 1 + 6 \cdot 10^{-5} \text{s}^{-1} \cdot t - \frac{[6 \cdot 10^{-5} \text{s}^{-1} \cdot t]^2}{2!} \right]} \quad (5.1)$$

In the case of n is large

$$V = 1 - e^{-\bar{N}\pi [1.6 \cdot 10^{-2} \mu\text{m}/\text{s}]^2 t^2} \quad (5.2)$$

and when τ is small compared to $\frac{1}{n}$

$$V = 1 - e^{-\frac{\bar{N}\pi [1.6 \cdot 10^{-2} \mu\text{m}/\text{s}]^2 6 \cdot 10^{-5} \text{s}^{-1} \cdot t^3}{3}} \quad (5.3)$$

N is left as free variable.

The transformation process can be shown in the form of an Avrami plot; that is to plot $\ln(-\ln(1-V))$ against $\ln(t-t_{Inc})$. Figure 5.9 shows the Avrami plot for sample $\text{Ga}_{11.79}\text{Sb}_{88.21}$ at 100°C . The slope of an Avrami plot gives an indication whether the transformation process can be described better by the model for large n or for small n . For a two dimensional transformation

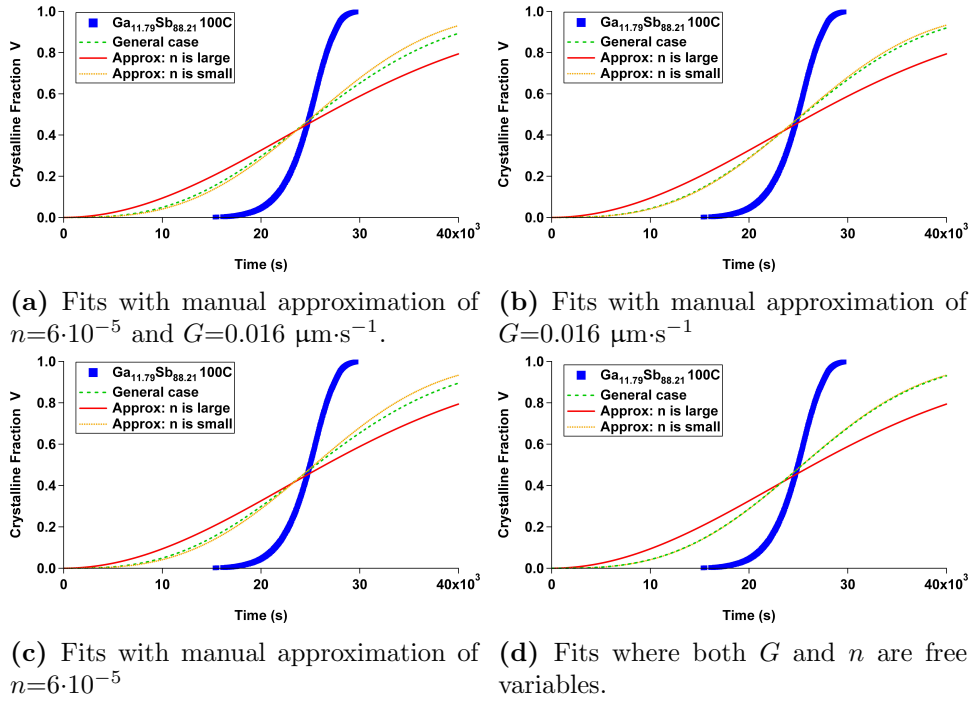


Figure 5.10: Fits of the General model, model when n is large, and the model where n is assumed small, to the transformation data of $\text{Ga}_{11.79}\text{Sb}_{88.21}$ at 100°C

process the slope lies in a range around two to three. If the slope lies around two, n is relatively large. If the slope lies around three, n is relatively small. The slope of the linear fit in Figure 5.9 is 12.423. An unexpected result, which can not be explained at this time, but an attempt will be made later in this report.

The three models (general, n =large, n =small) were tested in the following manner. First the derived approximations for n , G and σ , are inserted into the models and only N will be a free variable. Then N and either n , or G will be free variables. Finally, n , G and N will be free variables.

In Tables 5.2 through 5.5, N is given average amount of germ nuclei per square mm (mm^{-2}), because the area observed during growth measurements was approximately 1 mm^2 , see Figure 5.7). G is given in $\mu\text{m}\cdot\text{s}^{-1}$, to make the derived values easily comparable with those presented in Figures 5.1, 5.3 and 5.4.

The Matlab curve fitting tool was used to fit the different models to the observed data. The results are shown in Figure 5.10. The models do not converge to the measured data on their own, but need to be given starting values near the approximated values. If there is more than one free variable, there are multiple solutions to which the models can converge, as is expected by examining equations 5.1, 5.2 and 5.3. For example; in the equations a

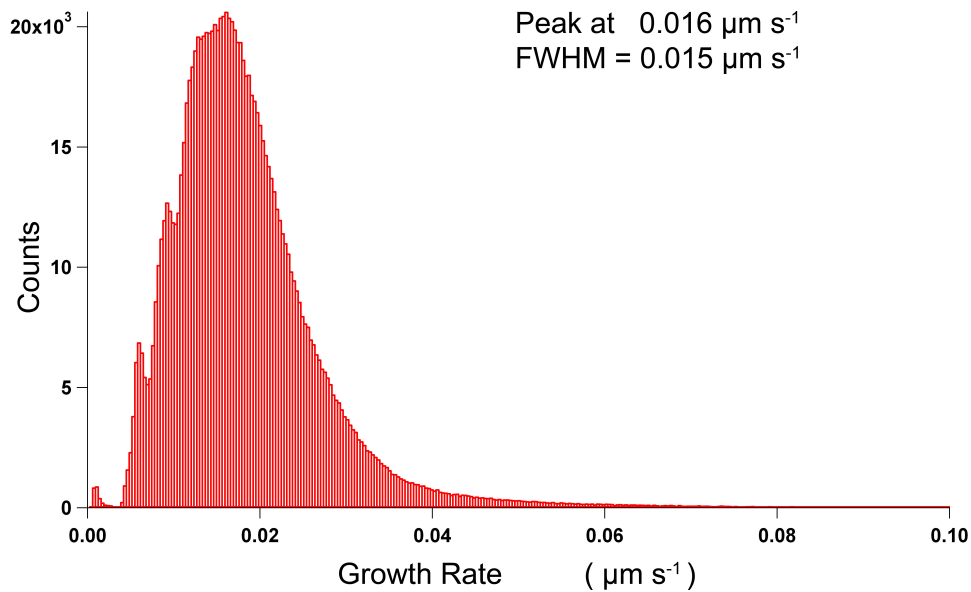


Figure 5.11: Histogram of the measured growth rates during the transformation process of $\text{Ga}_{11.79}\text{Sb}_{88.21}$ at 100°C .

change in G can be compensated by a change in N and vice versa. None of the models is able to accurately fit the measured data. In all cases, first the crystalline fraction is overestimated and then underestimated. The highest value for the coefficient of determination R^2 is 0.6029.

When N is the only free variable, the confidence bounds are close to the derived variable. Adding more free variables does not improve the accuracy of fits and the increase confidence bounds around the derived value of the free variables. In all cases the fitted values for n and G converge to the derived values to within one order of magnitude. However all fitted values for N are below the observed 40 activated nuclei, except for one case and in this case n was a factor 10 lower than the measured value, see Table 5.5.

If the growth rate would be a function increasing with time, at first the amount of crystalline fraction would be lower than derived by the models above, and subsequently as time increases it would be higher. This could explain the observed discrepancy between the presented models and the measurement data.

There are two indications that the growth rate is indeed increasing with time. One, Figure 5.7 shows that G is not uniform over the entire surface and two, the histogram of the observed growth speeds of sample $\text{Ga}_{11.79}\text{Sb}_{88.21}$ at 100°C shown in Figure 5.11 is not symmetrical and has a predisposition for higher growth speeds and its FWHM has almost the same value as the observed peak. If, how and why the growth speed is not constant in time will be investigated in the next chapter.

Model	Physical quantity	Estimate	Fit	(95% confidence bounds)	R ²
General case	N (mm ⁻²)	NA	3.603	(3.447, 3.759)	0.5601
	n (s ⁻¹)	$6 \cdot 10^{-5}$	NA		
	G (μm·s ⁻¹)	0.016	NA		
n is large	N (mm ⁻²)	NA	1.226	(1.167, 1.286)	0.4409
	G (μm·s ⁻¹)	0.016	NA		
n is small	N (mm ⁻²)	NA	2.597	(2.489, 2.704)	0.6027
	n (s ⁻¹)	$6 \cdot 10^{-5}$	NA		
	G (μm·s ⁻¹)	0.016	NA		

Table 5.2: Fits with Manual estimation for both n and G , as plotted in Figure 5.10a.

Model	Physical quantity	Estimate	Fit	(95% confidence bounds)	R ²	
General case	N (mm ⁻²)	NA	9.905	(-18.27, 38.08)	0.5887	
	n (s ⁻¹)	$6 \cdot 10^{-5}$	$1.751 \cdot 10^{-5}$			(-3.792·10 ⁻⁶ , 7.293·10 ⁻⁴)
	G (μm·s ⁻¹)	0.016	NA			
n is large	N (mm ⁻²)	NA	1.226	(1.167, 1.286)	0.4409	
	G (μm·s ⁻¹)	0.016	NA			
n is small	N (mm ⁻²)	NA	10.03	(-343, 345)	0.6029	
	n (s ⁻¹)	$6 \cdot 10^{-5}$	$1.573 \cdot 10^{-5}$			(-0.005378, 0.00541)
	G (μm·s ⁻¹)	0.016	NA			

Table 5.3: Fits with Manual estimation for Growth rate G , as plotted in Figure 5.10b.

Model	Physical quantity	Estimate	Fit	(95% confidence bounds)	R ²
General case	N (mm ⁻²)	NA	20.85	(-1737, 1779)	0.5601
	n (s ⁻¹)	$6 \cdot 10^{-5}$	NA		
	G (μm·s ⁻¹)	0.016	$6.674 \cdot 10^{-3}$	(-0.2748, 0.2881)	
n is large	N (mm ⁻²)	NA	16.02	(-1338, 1370)	0.4409
	G (μm·s ⁻¹)	0.016	$4.427 \cdot 10^{-3}$	(-0.1827, 0.1915)	
n is small	N (mm ⁻²)	NA	21.95	(-1303, 1346)	0.6029
	n (s ⁻¹)	$6 \cdot 10^{-5}$	NA		
	G (μm·s ⁻¹)	0.016	$5.536 \cdot 10^{-3}$	(-0.1616, 0.1726)	

Table 5.4: Fits with Manual estimation for nucleation probability n , as plotted in Figure 5.10c.

Model	Physical quantity	Estimate	Fit	(95% confidence bounds)	R ²
General case	N (mm ⁻²)	NA	96.83	($-7.58 \cdot 10^4$, $7.599 \cdot 10^4$)	0.5992
	n (s ⁻¹)	$6 \cdot 10^{-5}$	$4.38 \cdot 10^{-6}$	($-352.4 \cdot 10^{-6}$, $361.1 \cdot 10^{-6}$)	
	G (μm·s ⁻¹)	0.016	$9.884 \cdot 10^{-3}$	($-4252 \cdot 10^{-3}$, $4272 \cdot 10^{-3}$)	
n is large	N (mm ⁻²)	NA	16.02	(-1303, 1346)	0.6029
	G (μm·s ⁻¹)	0.016	$4.427 \cdot 10^{-3}$	(-0.1827, 0.1915)	
n is small	N (mm ⁻²)	NA	8.757	($-2.23 \cdot 10^7$, $2.23 \cdot 10^7$)	0.6029
	n (s ⁻¹)	$6 \cdot 10^{-5}$	$4.088 \cdot 10^{-5}$	(-119.7, 119.7)	
	G (μm·s ⁻¹)	0.016	0.001062	(-2019, 2019)	

Table 5.5: Fits where there were no constraints on G or n , as plotted in Figure 5.10d.

Chapter 6

Exponential increase in growth rate

In the last section of the previous chapter it was attempted to show that the kinetics of the crystallisation process could be modelled by using the Avrami equations. However, it turned out that this was not possible. The strongest indication on the question why JMAK theory went astray is that the growth rate is not uniform during the crystallisation process. This hypothesis was supported by Figures 5.7 and 5.11

It turns out that growth rate is indeed not constant in time. This does not mean that an Avrami model is unable to describe the kinetics underlying the crystallisation process. Indeed it is true that in his articles[10][11] Avrami explicitly derived his equations in the case where growth rate is constant in time. Nowhere is this presented as a prerequisite. Avrami based his model on the evidence presented in many experimental papers, but his model is built in such a way, that even if one does not understand or knows the underlying physical properties that cause non-constant growth rate, it is still usable as long as the relationship between growth rate and time is known. This will be the end goal of this chapter.

Isothermal measurement results from sample $\text{Ga}_{11.79}\text{Sb}_{88.21}$ will be primarily used to describe how the growth rate changes during the crystallisation process. First a purely empirical equation shall be derived from these measurements. A two dimensional map of the observed growth rates for $\text{Ga}_{11.79}\text{Sb}_{88.21}$ at 100°C is shown in Figures 5.7 and 6.1. From Figure 6.1 one can observe that the growth rate increases as the crystals get larger. The questions that need to be answered are: does the growth rate increase because the crystals grow larger, does growth rate depend on time, or is growth rate a function of crystal size and time? These questions are answered in the first part of this chapter.

The second part of this chapter will start the investigation in the underlying physical causes of changing growth rate. It is known that during

the crystallisation process latent heat is released[3][1][2]. Therefore, the first hypothesis is that heat produced during the crystallisation process increases the temperature of the layer during the crystallisation process and therefore increases the growth rate. The second hypothesis is that the increase in growth rate is caused by relaxation of the layer. The second hypothesis appears to be correct, and at the end of the second section an attempt will be made to describe how relaxation effects the physical properties of the layer.

Finally in the last section the observational equation derived in the first part of this chapter will be used to derive the appropriate Avrami equation. It turns out, that although an Avrami plot still offers little information on itself of the crystallisation process, the modified Avrami equation is able to fit the measurement data to much higher degree then the equation presented in section 5.1.3 of the last chapter.

6.1 Growth rate dependency on crystal size and absolute time

From Figures 5.7, 5.11 and the discussion presented in the last chapter, the image arose that the growth rate is not constant during the crystallisation process. Measurement of two individual points in Figure 6.1 shows us that this indeed the case. The growth rate at point A is $0.0056 \mu\text{m}\cdot\text{s}^{-1}$, while the growth rate at point B is $0.0244 \mu\text{m}\cdot\text{s}^{-1}$. To determine whether the growth rate is dependent on crystal size, time, or a combination of both, additional information is needed. Therefore, first it is determined that growth is uniform in all directions and crystal growth rate does not depend on the location on where the crystal grows on the sample. Once this is established, the aforementioned relation will be established.

A more visual overview on how the relation between growth rate and, time and/or crystal size is established is given in Figure 6.1, several crystals have been selected and colour-coded. Crystal 1a is the very first crystal that appears, and it will be used to determine if growth is uniform in all directions. Crystals 1a through 1e arose at approximately the same time and will be used to establish if crystal growth is independent of location. Crystals 1 through 7 will then be used to determine if growth rate is dependent on time, crystal size, or a combination of both.

With the current software it was not possible to average all growth rates lying on a circle, where the centre of the circle corresponds with the centre of the crystal. It was possible to plot the measured growth rates lying on a line in Figure 6.1 against either time or the length of the line. The lines in each of the selected crystals represent such a line profiles that was used to determine the growth rate function.

The time line of the crystallisation process is given below the growth rate map. As can be seen from this time line, the software used to determine

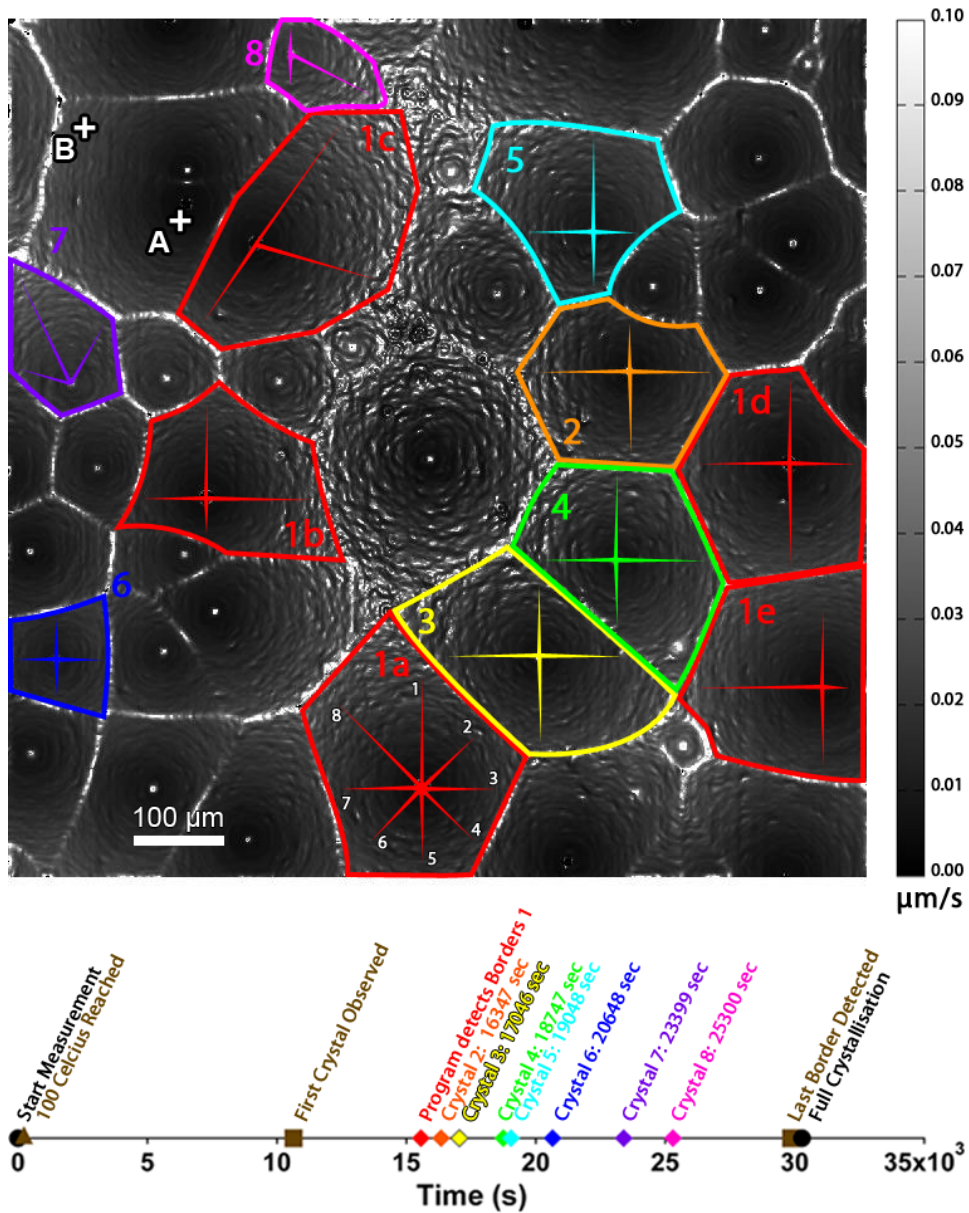


Figure 6.1: Growth rate map of measured crystal growth rates. Growth rate at point A is $0.0056\mu\text{m}\cdot\text{s}^{-1}$. Growth rate at point B is $0.0244\mu\text{m}\cdot\text{s}^{-1}$. Growth rates are represented in a grey colour code whose scale can be seen on the right side of the map. Several crystals have been highlighted. A time line visualisation of the crystallisation process is shown below the growth rate map. Crystals 1 through 7 arose at different moments in time. Crystal 1a is used to show that growth is uniform in all directions. Crystals 1a through 1e are used to show that growth is uniform throughout the sample. Crystals 1 through 7 are used to show that growth is uniform in time, but not with crystal size.

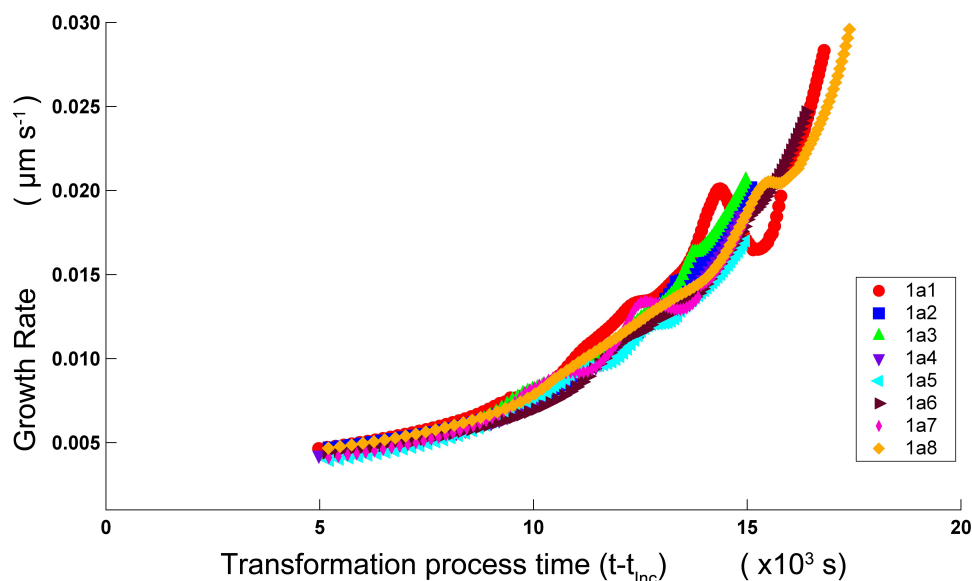


Figure 6.2: Growth rate in $\mu\text{m}\cdot\text{s}^{-1}$ against transformation time in seconds (s) for crystal 1a in direction 1 through 8 (see Figure 6.1 for reference). Growth rates were determined using line profiles.

growth rate can not cover the entire crystallisation process. This happens because of the difference in reflectivity between the amorphous and crystalline state is relatively small. The program also has trouble determining the correct growth rate at the centre of a crystal and in locations where two crystals meet. By not extending measured line profiles all the way to crystal borders and centres, it has been attempted to minimize these errors.

6.1.1 Average directional symmetry of growth rate

Figure 5.6 suggests that growth is uniform in all directions, this is corroborated by the borders shown Figures 6.6a and 6.6b later on this report. Line profiles of the measured growth rate are taken in 8 different directions from the centre of crystal 1a and they are shown in Figure 6.2. If crystal growth is perfectly uniform in all direction, then all line profiles should be equal, if crystal growth has a directional preference, some growth rate line profiles should be observably higher than other line profiles for the duration of the entire measurement. Neither is observed in Figure 6.2. The line profiles cross each other several times and are not perfectly equal. This means that there is no observable directional growth preference, but the statement of uniform growth can not yet be made either.

One explanation for the jolts in the line profiles of crystal 1a could be that during measurement the camera and/or sample are not completely still. If this is true then a jolt of increased growth speed in one line profile, should

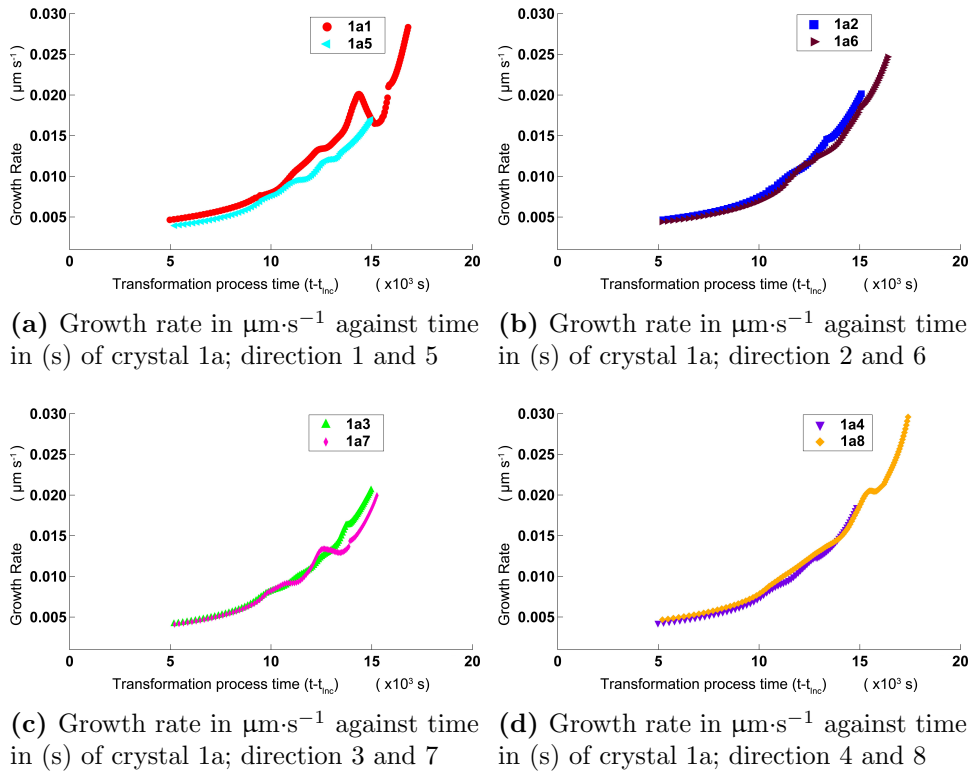
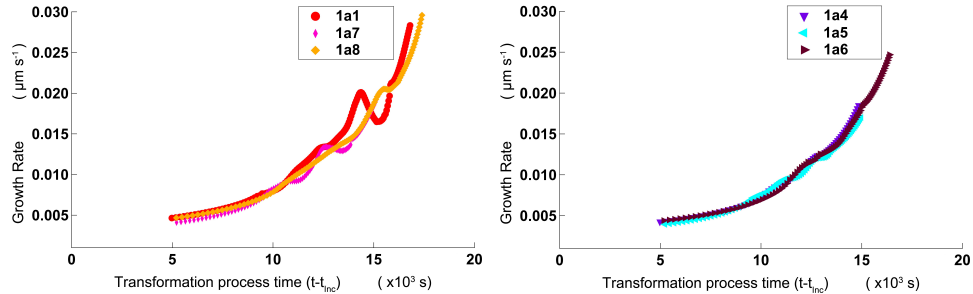


Figure 6.3: Figures 6.3a through 6.3d show Growth rate in $\mu\text{m}\cdot\text{s}^{-1}$ against transformation time in seconds (s) of opposing directions in crystal 1a (see Figure 6.1 for reference). Although there is some overlap in the times that the change in growth rate is less smooth, the jolts in the growth rate change, are more often that not, not in opposite direction.

correspond with a jolt of decreased growth speed in the opposite direction. To test this hypothesis line profiles with opposite direction are plotted in Figure 6.3. Irregularities in the growth rate line profiles occur at the almost the same instances in time, but more often than not, irregularities have the same direction. This leads to the hypothesis that there is some camera movement (irregularities in opposite direction are present in Figure 6.3), but there might also be actual jolts in the growth process of an individual crystal.

If this is the case, then line profiles with almost the same direction should only show irregularities in the same direction. To test this hypothesis, line profiles in directions 1,7,8 and 4,5,6 of crystal 1a are plotted in Figure 6.4. Irregularities occur at almost the same instances in time, but in many cases have an opposite direction. This means that the hypotheses that the irregularities are caused by camera movement, or that they are caused by irregularities in crystal growth, can neither be confirmed nor dismissed.

Another way to test if the irregularities in the growth rate line profiles



(a) Growth rate in $\mu\text{m}\cdot\text{s}^{-1}$ against time in (s) of crystal 1a; direction 1, 7, and 8 (b) Growth rate in $\mu\text{m}\cdot\text{s}^{-1}$ against time in (s) of crystal 1a; direction 1, 5, and 6

Figure 6.4: Figure 6.4a and 6.4b show growth rate in $\mu\text{m}\cdot\text{s}^{-1}$ against transformation time in seconds (s) based on line profiles which are almost in the same direction in crystal 1a (see Figure 6.1 for reference). Although there is some overlap in the times that the change in growth rate is less smooth, the jolts in the growth rate change, are more often that not, in opposite direction.

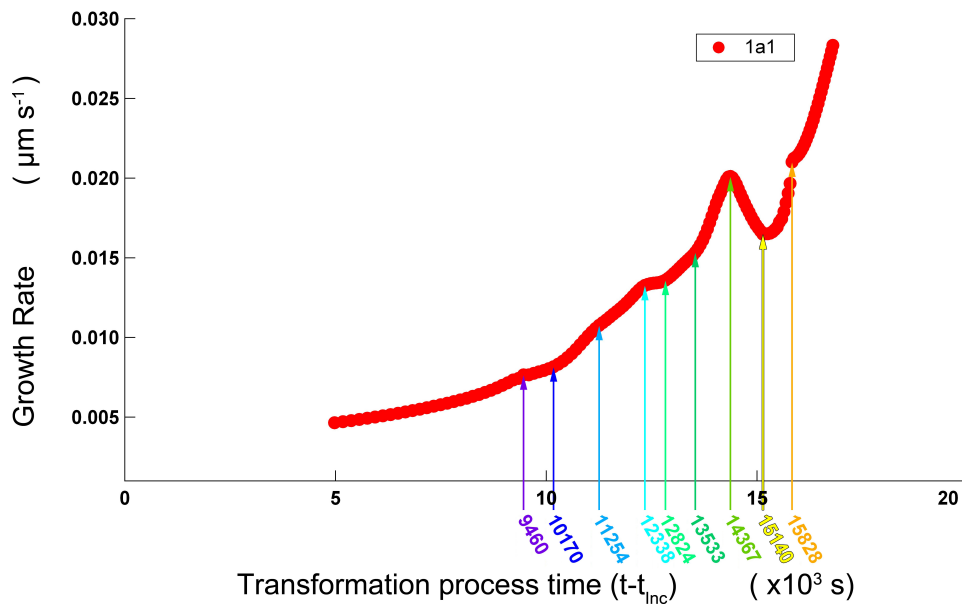
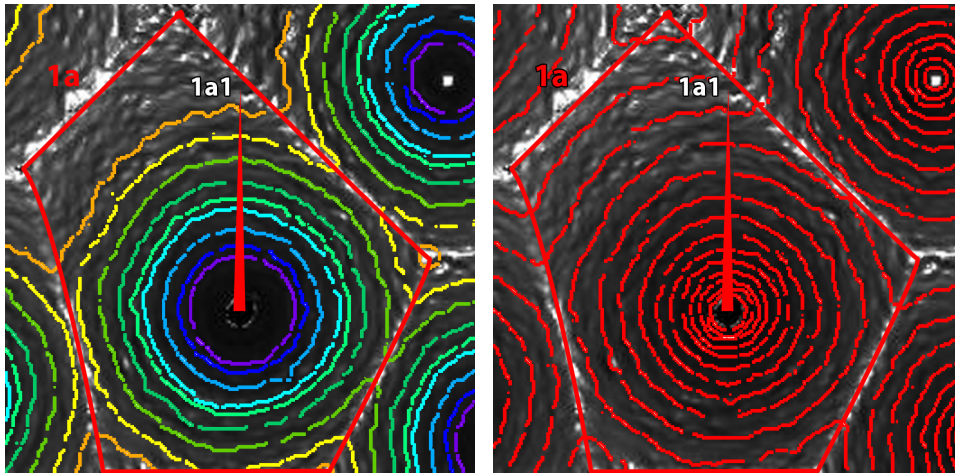


Figure 6.5: Growth rate in $\mu\text{m}\cdot\text{s}^{-1}$ against transformation time in seconds (s) for crystal 1a in direction 1 (see Figure 6.1 for reference). Points where the change in growth rate is not smooth are indicated with coloured arrows. The time when change in growth rate was not smooth is given in seconds after incubation time. The colours of the arrows correspond with the colours of the border in Figure 6.6a.



(a) Borders of crystal 1a corresponding with the moments when the growth rate line profile of direction 1 exhibits jolts. (b) Borders of crystal 1a where the difference between each line represents 1000 seconds.

Figure 6.6: Figures 6.6a and 6.6b measured borders of crystal 1a at specific moments in time. Borders do not appear to be smooth shapes in contrast with Figure 5.6.

are caused by camera movement is to see if the measured crystal edge suddenly shifts at certain moments in time. Figure 6.5 shows the growth rate line profile of crystal 1a in direction 1. The irregularities are indicated by means of coloured arrows. Beneath these arrows are shown the moments in time when these irregularities occur. In Figure 6.6a the detected borders corresponding with moments in time when growth is irregular are plotted over the growth rate map of crystal 1a, a shift for the entire crystal border is not visible. The detected borders are rather irregular and do not form smooth circles. The statement that the camera does not move can not be made, camera movement can not be the main cause of the irregularities in the growth rate line profiles. For comparison, the borders shown in Figure 6.6b are measured 1000 seconds apart.

Based on previous statements and the detected border presented in Figure 6.6a and Figure 6.6b one can draw the conclusion that most of the irregularities from the growth rate line profiles stem from the irregularity of the borders of detected crystals. The next question to be asked is; can the irregularity of the detected border be attributed to the used software, or is the border of the crystal truly irregular. Close inspection of the optical images learns that the crystal border is indeed irregular, but the edge detected by software is more irregular than the actual border.

A highly exaggerated schematic overview of the crystal growth process is shown in Figure 6.7. Bulges of crystalline material emerge at the crystal border, creating gaps between them. These gaps are then in turn crys-

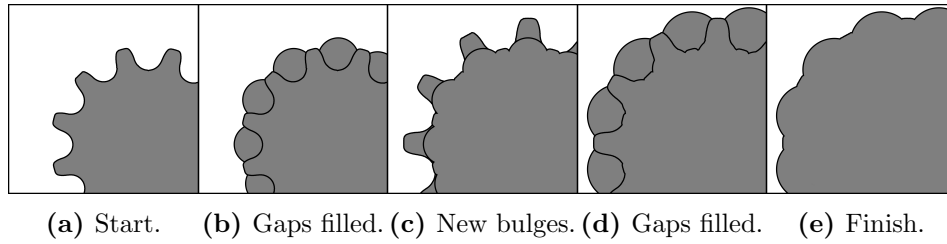


Figure 6.7: Figures 6.7a through 6.7e show the exaggerated growth mechanism of otherwise circular crystals. The lines of the crystal edge of the previous step are shown in the figures to clarify the growth mechanism. These edges are not seen when looking at the photo's. The edge of a crystal is not entirely smooth, gaps between bulges on the crystal edge are filled. New bulges emerge from these filled gaps. Crystal growth is relatively faster when gaps are filled, then when new bulges start to emerge from the crystal edge.

tallised. This happens faster than the creation of a bulge. Based on the semicircular nature of the borders, it appears that there is no preference direction for growth. Growth is thus relatively uniform in all directions and taking the average of all growth rate line profiles of crystal 1a will give the average growth rate in all directions in time. To have a an accurate description of the growth rate of an individual crystal or sample is necessary to use multiple growth rate line profiles and take an average over them.

The average of all eight growth rate line profiles of crystal 1a is given

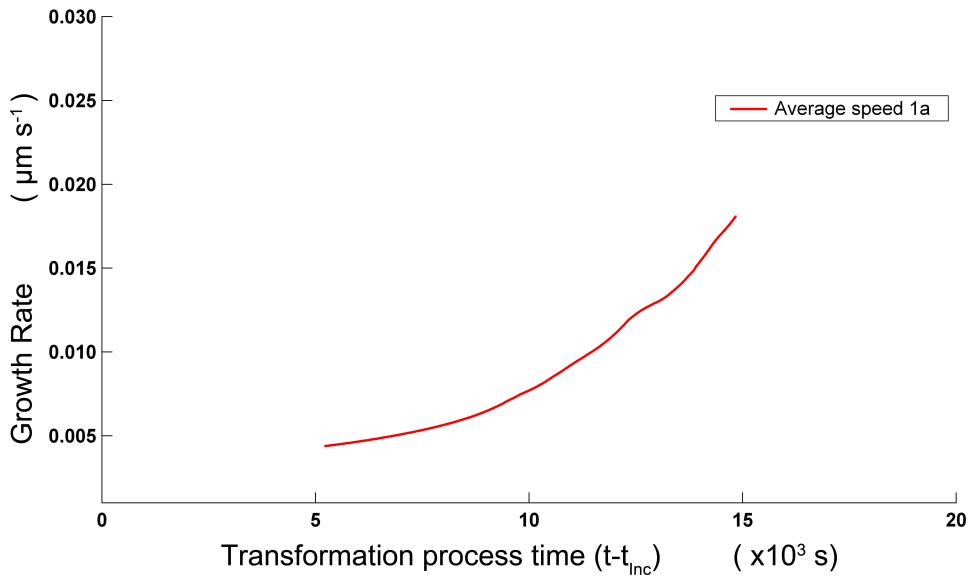


Figure 6.8: Growth rate in $\mu\text{m}\cdot\text{s}^{-1}$ against transformation time in (s) of the the average of all 8 directional growth rate line profiles of crystal 1a (see Figure 6.1 for reference), most of the irregularities are smoothed out.

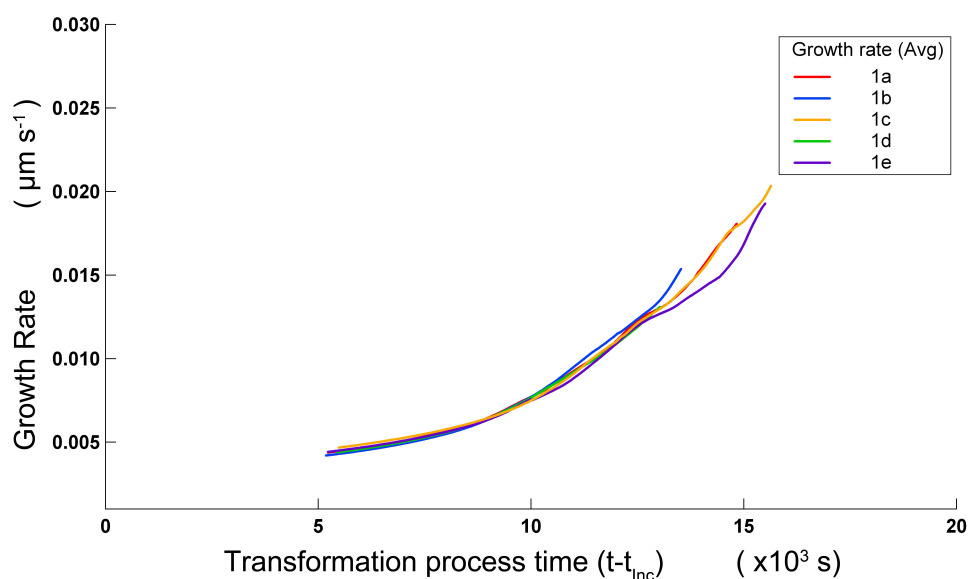


Figure 6.9: Growth rate in $\mu\text{m}\cdot\text{s}^{-1}$ against transformation time in (s) of the the average of all directional growth rate line profiles of crystal 1a through 1e. Crystals 1a through 1e arose at approximately the same time, but at different locations on the sample (see Figure 6.1 for reference). The similarity in the change in growth rate seems to indicate that growth rate does not depend on the location of origin of the crystal on the sample.

in Figure 6.8. The growth rate dependence on time shown in Figure 6.8 is relatively smooth in comparison with Figures 6.2, 6.3 and 6.4. It is uncertain if the remaining irregularities are caused by measurement inaccuracy or that they are caused by jolts in the crystal growth. For the purposes in the report however, it is assumed that growth is uniform in all directions and small irregularities are ignored. A complete quantitative analysis of the growth of an individual crystal is beyond the scope of this report and the accuracy of the measured data.

6.1.2 Crystal growth rate invariance of location

At first glance the logical next step would be to find out if the change in growth rate is dependent on crystal size, time or a combination of both. The first step would be to take two crystals, which nucleate at different moment in time and plot crystal radius against time, where $t=0$ represents the first moment the crystal could be detected with the eye¹. If the two radii are completely equal in size with respect to their times of origin, then it is shown that the change in growth rate is dependent on crystal size and independent

¹as opposed to experimental time where $t=0$ is defined as the moment the desired annealing temperature has been reached. Unless otherwise noted, time will mean experimental time in this chapter

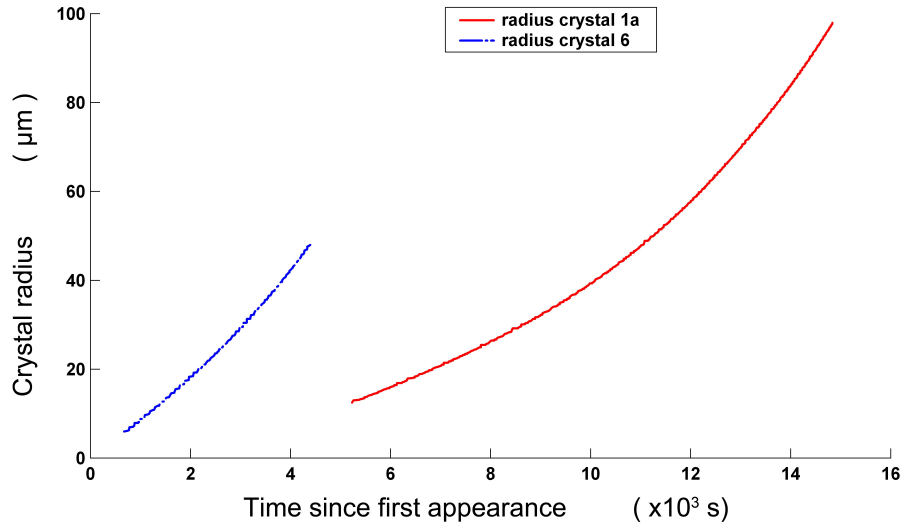


Figure 6.10: Crystal radius in μm as a function of time for crystal 1a and 6. Time $t=0$ represents the moment the crystal became visible with the eye. Measurement points are based on the average of line profiles for both crystals. Crystal 1a and 6 arose at different moments in time (see Figure 6.1 for reference).

of experimental time. When they are not equal, the opposite conclusion can not be made. An explanation could be that growth is also dependent on the location of the crystal on the sample. In this section this option will be ruled out.

Crystals 1a through 1e in Figure 6.1 nucleate at approximately the same moment in time. If crystal growth is independent of sample location, there should be no difference in the plots of growth rate against time of crystals 1a through 1e. The growth rate against time plots of crystal 1a through 1e are shown in Figure 6.9. They are similar during the first part of the crystal growth process. Although there is some difference between the crystal growth rate as time goes on, this can be attributed to the irregularities of individual line profiles and the increased difficulty of the software to accurately determine the boundary between amorphous and crystalline material, due to the lack of amorphous material on the sample. Crystal growth is thus independent of sample location.

6.1.3 Crystal size dependence or time dependence

To determine whether the growth rate is a function of crystal size, time or a combination of both, crystals 1a and 6 are selected for comparison, see Figure 6.1. First the crystal radius of both crystals will be plotted against time, with $t=0$ defined as the moment in time when the crystal is first visible. If the change in growth rate is purely a function of crystal radius, then the

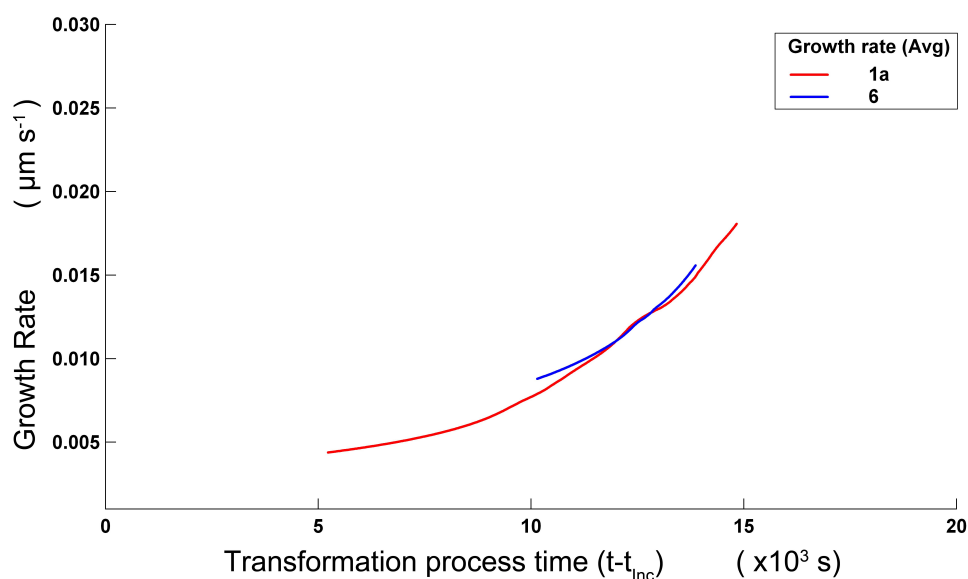


Figure 6.11: Growth rate in $\mu\text{m}\cdot\text{s}^{-1}$ against transformation time in (s). Crystals 1a and 6 arose at different moments in time, but growth at approximately the same speed (see Figure 6.1 for reference).

two lines should be equal even if crystal 1a and 6 appeared at different moments in time. The software is not able to completely cover the entire crystallisation process, because of reasons mentioned earlier in the report. The moment in time when the crystal first appears is manually determined and the measurement data of the software is compensated accordingly. The result can be seen in Figure 6.10

The two graphs in Figure 6.10 are not equal. This means the growth rate can not only depend on crystal size. This leaves the two options that it is dependent on time or a combination of the two. To test if crystal growth is purely a function of time, the growth rate measured at the same moments in time for crystal 1a and 6 is depicted in Figure 6.11. The growth rates in Figure 6.11 are fairly similar in time. This is a strong indication that the increasing growth rate is only dependent on experimental time, but a definite conclusion will be made in the next section.

6.1.4 Exponential increase in growth rate with respect to time

To strengthen the claim that growth rate is purely a function of time, Figure 6.11 has been augmented with the data from crystals 1 through 8 in Figure 6.12. A first guess is that growth rate increases exponentially in time. In Figure 6.13 the average growth rate of all 8 crystals is taken and an exponential fit resulted in the closest match with the measurement data.

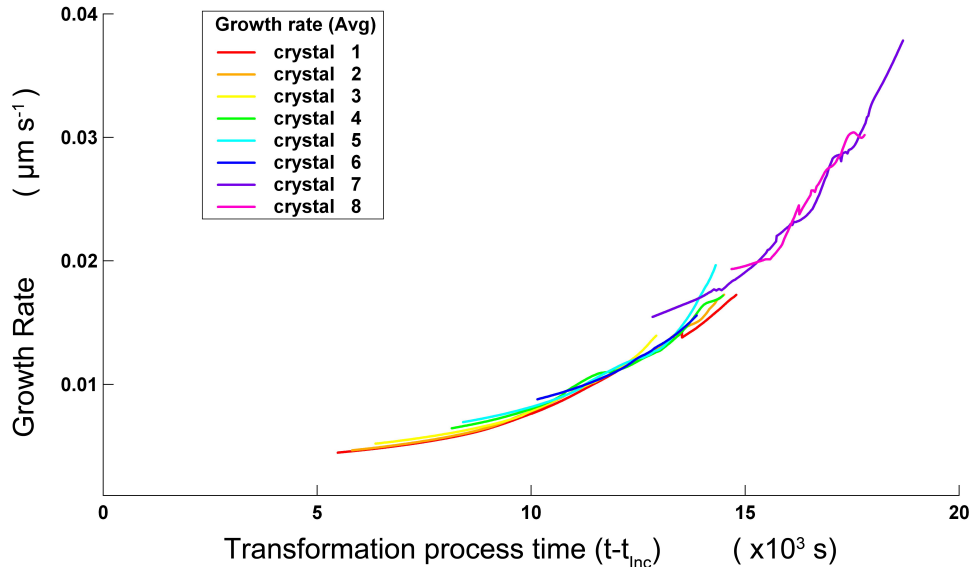


Figure 6.12: Growth rate in $\mu\text{m}\cdot\text{s}^{-1}$ against transformation time in (s) for crystals 1 through 8. The colour of each line corresponds with the colour of the border of the crystal in Figure 6.1. Since crystal 1a through 1e arose at approximately the same moment in time, crystal 1 represents the average of crystal 1a through 1e.

Three observations can be made regarding the growth of individual crystals in comparison with the averaged growth rate of all 8 crystals. The first is that when an individual crystal first appears, the growth rate appears to be higher than one would expect on the basis of the exponential fit or on the basis of the average speed of all 8 crystals. As time increases the growth rate of an individual crystal will conform to the average growth rate. The second is that as the boundary of an individual crystal approaches the boundaries of another crystal, the growth rate starts to increase again in comparison with the the average measured growth rate and its fit. It is known that the software program tends to overestimate the crystal growth rate at the centre of the crystals and at moments when two crystal boundaries approach each other. To compensate for the effect the line profiles were chosen to start a little bit outside the crystal centre and end before two crystal boundaries would meet. A preliminary double check revealed, that these two effects can mostly be attributed to measurement errors, but not in its entirety. A third less obvious observation is a small bump that some crystals exhibit in their growth rate graphs, halfway through their lifespan. This can be seen for crystal 1a in Figure 6.11 and for crystal 4 and 6 in Figures 6.12 and 6.13.

None of these three observations can be dismissed purely as measurement errors, but since the average of many crystals constitutes to a smooth line as can be seen in Figure 6.13, one can make the statement that they contribute relatively little to the crystallisation process as a whole and there-

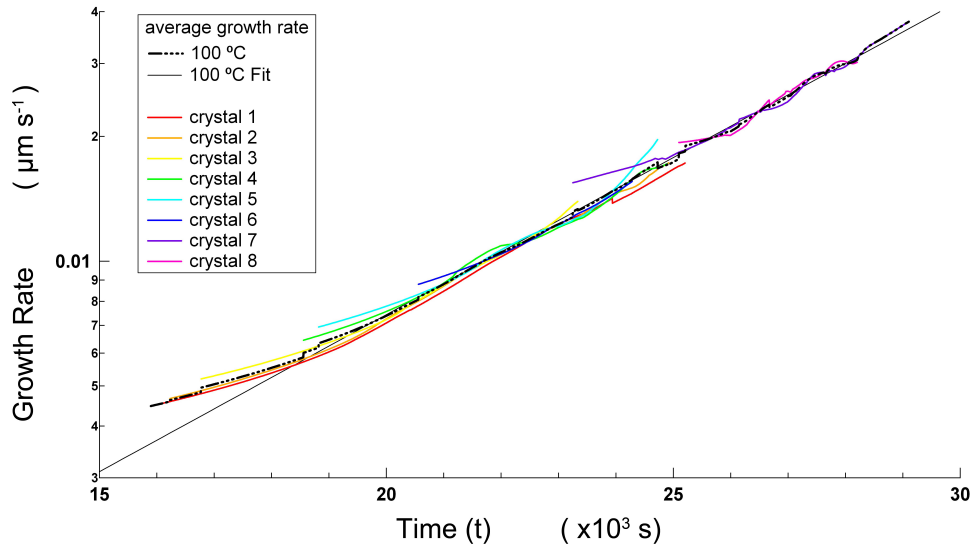


Figure 6.13: Growth rate in $\mu\text{m}\cdot\text{s}^{-1}$ against time in (s) for the average of crystals 1 through 8 and the corresponding exponential fit, the average growth rate of crystal 1 through 8 is also shown in the figure to give an better overview how individual crystal growth deviates from average growth rate against time. Growth rate is given in logarithmic scale.

fore in determining an observational equation for the growth rate during the crystallisation process, these effects (if they exist) are ignored. The deviation of the average of the growth rates of all 8 crystals from the exponential fit at the beginning and end of the curve can thus be attributed to a lack of averaging over multiple crystals. Growth rate is thus treated as an exponential function purely dependent on time.

6.2 The influence of latent heat and/or layer relaxation on growth rate

Now that it has been established that the increase in growth rate can be described by an exponential function dependent on time, it is time to find physics behind this phenomenon. There are two hypotheses for explaining the increase in growth rate. The first is based on the excess heat that is released during the crystallisation process. Since the temperature of the ceramic heater is continuously monitored and compensated to remain constant during the crystallisation process, it is assumed that the heat released during the crystallisation process, slightly increases the temperature in the sample, but is not registered by the thermocouple in the ceramic heater, because it is confined to the deposited layer film. This increase in temperature of the layer, causes the increase in growth rate. The second is that the

layer undergoes a relaxation effect, making the transition from amorphous to crystalline easier.

To apply JMAK theory correctly it is necessary to know which of these two hypotheses is the correct one. If the first hypothesis is correct, Avrami needs to be considered for the non-isothermal case, while if the second hypothesis is correct, The Avrami equation needs to be adjusted with the assumption that growth rate increases exponentially in time. Therefore, determining the correct hypothesis will be the main focus of this section. It will be shown that heat is not the cause of the increase growth rate over time. This will be done in twofold. First it is assumed that heat is the cause of the increase in growth rate, but this will lead to some very unlikely conclusions. Then a relaxation experiment will close the case and show irrefutably that the increase in growth rate is caused by a relaxation effect.

Growth rate does not change with time for all samples discussed in the previous chapter. The growth rate line profiles over the individual crystals of the samples with composition $\text{Ga}_{10.42}\text{Sb}_{89.58}$, see Table 4.7 and Figure 5.1, did not show an increase in speed over time. If heat produced during the crystallisation process was the cause of the increased growth rate, then this effect should also be visible in all samples. Of course, the difference in evaporation speed with which the samples were created and differences in composition could also be an explanation for the difference in crystallisation behaviour, so latent heat may not yet be refuted as a possibility.

If heat is the cause of the increase in crystallisation rate, then at the very moment crystallisation starts the measured growth rate should always be higher then for lower measurement temperatures. However, relaxation affects the sample during the entire experiment, thus also during the incubation time before any crystallisation takes place. Since for lower temperatures the incubation time is much longer then for higher temperatures, it might be possible that the layer is more relaxed then at higher temperatures. This means that it might be possible that at some temperature T , when the first crystal emerges and the growth rate is measured, it is lower then the growth rate measured for the first crystals that emerged at a lower temperature. If this effect can be observed, immediately it is shown that latent heat is not the cause of the increased growth rate. To this end Figure 6.14 has been created.

In Figure 6.14 the change in growth rate has been measured at different temperatures during the crystallisation process. Each temperature is colour-coded and for each temperature between 16 and 28 line profiles (depending on crystal size at a certain temperature) have been taken, to minimize errors and irregularities in the growth rate measurements. Since incubation time changes with temperature, time $t=0$ is defined as the moment that the sample reached its desired temperature. Exponential fits have been made through the measured data, but the formulas are not shown, since the correct representation depends on the underlying physical effect. If relaxation is the

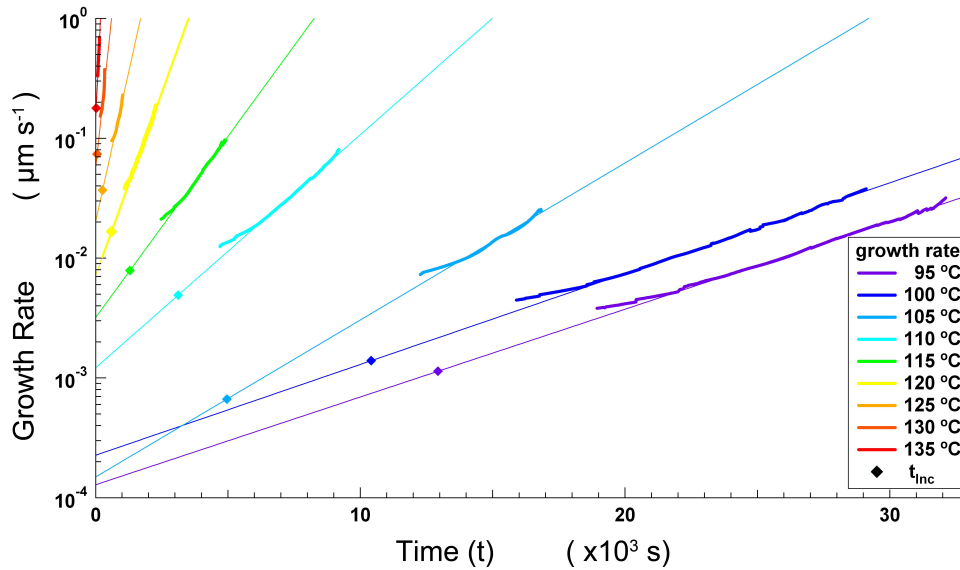


Figure 6.14: Growth rate in $\mu\text{m}\cdot\text{s}^{-1}$ against time in (s) for different temperatures of sample Ga11.79Sb88.21. Growth rate is given in logarithmic scale. An exponential fit has been added to each measurement and the incubation time is indicated on this fit in the form of a rhombus.

cause of the increased growth rate, then the moment the goal temperature for measurement is reached should be taken as time $t=0$. If latent heat is the cause of the increase in growth rate, then the moment of incubation t_{Inc} should be taken as starting point ($t_0=t_{\text{Inc}}$). The first moment the software can detect the crystals is the start of the measurement shown in Figure 6.14, however manually the moment of incubation can be determined much more accurately. The incubation time for each temperature is indicated with a diamond on the corresponding fit.

What should be kept in mind that not at every temperature the sample was fully crystallised at the end of the measurement. The sample was fully crystallised at temperatures: 95°C, 100°C, 110°C, 115°C and, 120°C. As can be seen in Figure 6.14, the growth rate measured at 105°C breaks the general trend of the rest of the graph. At the end of the measurement less than 20% of the sample had crystallised and the growth rate was determined by means of only 2 large crystals who arose at approximately the same time with 8 growth rate line profiles each. This makes the bump in the growth rate measurement of an individual crystal visible in the measurement of 105°C.

The first observation is that the initial growth rate increases with increasing substrate temperature. A second observation is that the start of the measured growth rate lies above the exponential fit. In the previous section this has been attributed to way the measured growth rate changes

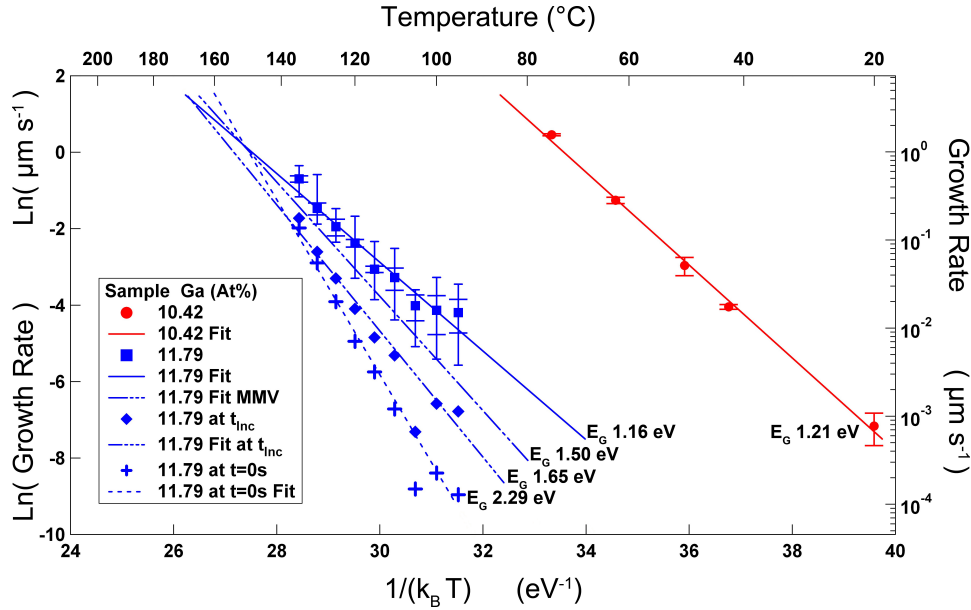


Figure 6.15: Growth rate measurements of $\text{Ga}_{10.42}\text{Sb}_{89.58}$ and $\text{Ga}_{11.79}\text{Sb}_{88.21}$. The first broad stripes connected to each measurement point of $\text{Ga}_{10.42}\text{Sb}_{89.58}$ and $\text{Ga}_{11.79}\text{Sb}_{88.21}$ correspond to the FWHM value of the corresponding growth rate histogram. The outer broad stripes connected to each measurement point of $\text{Ga}_{11.79}\text{Sb}_{88.21}$ corresponds to the minimum and maximum measured growth rate at each measured temperature. The rhombus shaped points corresponds to the theoretical growth rate at the incubation time of each sample based on the exponential fit through the data points of Figure 6.14. The plus shaped points correspond to the theoretical growth rate at the moment the isothermal growth temperature is reached, based on the exponential fit through data points of Figure 6.14. Arrhenius fits have been made the original measurement points first shown in Figure 5.1, through the minimum measured growth rate values (MMV), through the theoretical growth rates at t_{inc} and at $t=0$, see Figure 6.14, to obtain the growth activation energy E_G for different scenarios.

with time for individual crystals, but an alternative explanation could be that when the first crystals appear, the extra heat produced has little influence on the growth rate and that only later, when it becomes possible to discern the crystal borders heat becomes an influence on the crystallisation process. Thirdly, in the last chapter the material properties like the growth activation energy E_G were determined by means of the peak of a histogram of all measured growth speeds during crystallisation and this might be a distorted representation of the actual material properties, because it does not compensate for extra heat production or relaxation effects.

Figure 6.14 is used to create Figure 6.15. If heat production during the crystallisation process only effects the layer temperature sufficiently after a certain amount of the layer has been crystallised, then an Arrhenius fit

through the minimum measured growth rates should give the correct representation the actual growth activation energy E_G . In this case $E_G = 1.50\text{eV}$ (see Figure 6.15 for reference). If heat production immediately affects the crystallisation process, then an Arrhenius plot through the growth rate at incubation time based on the exponential fits in Figure 6.14 gives the best representation of the growth activation energy E_G . This is the fit through the diamond points in Figure 6.15. Because the sample crystallized at 105°C was not fully crystallized at the end of the measurement and because it breaks the trend portrayed by the other growth rate measurements this measurement is excluded for the Arrhenius plot through the diamond points in Figure 6.15. If heat production immediately affects the crystallisation process then the actual growth activation energy would be more in the range of $E_G = 1.65\text{eV}$. If latent heat is not the cause for the increased growth rate, but relaxation is, then an Arrhenius plot through the growth rates at time $t=0$ based on the exponential plots in Figure 6.14 gives the growth activation energy E_G , before the material has undergone any relaxation effects, however no conclusions can be made about the growth activation energy during the crystallisation process. Again in the case of relaxation the growth rate measurement at 105°C is discarded and the growth activation energy would be more in the range of $E_G = 2.29\text{eV}$. A heating effect distorts the observation of the growth activation energy E_G , since the actual temperature at the edge of the crystal is unknown, while a relaxation effect affects E_G , since relaxation changes the inherent material properties.

What the most accurate description of the activation growth energy E_G would be, will of course depend on which of these scenarios is true. The information in Figure 6.14 and 6.15 can be combined to determine the theoretical temperature increase ΔT . This is done by using the Arrhenius fits for the heat possibilities in Figure 6.15 and the Arrhenius fit through maximum measured growth rates in Figure 6.14. Since the amount of latent heat produced should not depend on temperature, it stands to reason that when the layer is fully crystallised, then the temperature increase should be the same for all measurements. Therefore, the temperature increase is only calculated in the cases where the entire sample had been crystallised. This is shown in Figure 6.16.

From Figure 6.16, it becomes apparent that not only is the temperature increase not equal for all measurements, it is extremely large. Combining the information from Figure 6.14 and 6.16 the statement would have to be made that if latent heat production is the cause of the increased growth rate, then during a period of 12000 seconds a layer of 200nm has a temperature increase of more than 20°C . Furthermore, this temperature increase would have been undetected by the thermocouple in the ceramic heater, or the controller would have compensated for the latent heat production, by reducing the power fed into the thermocouple. This is a very unlikely scenario and the

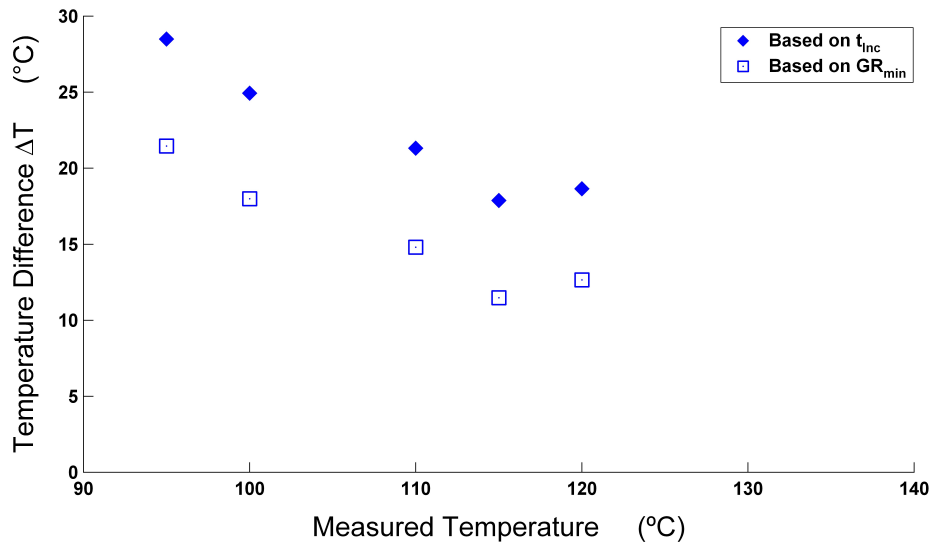


Figure 6.16: Theoretical temperature difference based on the assumption that the isothermal temperature measurement at the start of crystal growth is correct, and all energy released through crystallisation is evenly distributed throughout the layer. GR_{min} represents the case where it is assumed that the temperature difference caused by crystallisation only starts to have a significant affect, some time after t_{Inc} , thus ΔT is based on the Arrhenius fit through the minimum measured growth rate values (MMV). t_{Inc} represents ΔT based on the Arrhenius fit through the theoretical growth rates at t_{Inc} , see Figures 6.15 and 6.14.

hypothesis that latent heat production is the cause behind the increase in growth rate starts to look very unlikely as well.

If relaxation is the cause of the increased temperature effect, then it should affect the amorphous material before it has been crystallised. From Figure 6.14 it can be seen that the incubation at 95°C was over three hours. Therefore, a sample would be pre annealed for three hours at 95°C and then be cooled down to room temperature. Then an isothermal annealing experiment would be conducted with the pre annealed sample at 120°C. For comparison a second sample would be heated to 120°C without pre annealing. This experiment has been performed by Gert Eising 1 year after the original experiments and the results can be seen in Figures 6.17 and 6.18.

The physical properties of the material have changed over the course of 1 year as can be seen in Figures 6.17 and 6.18. From Figure 6.17 it is clear that pre annealing increases the growth rate at 120°C. The moment of time equals zero t_0 is defined as the moment that crystals are present on the sample and the sample has reached 120°C. In the case of the original measurement at 120°C and the measurement conducted one year later, this would be the incubation time ($t_{Inc}=t_0$), in the case for the sample that had

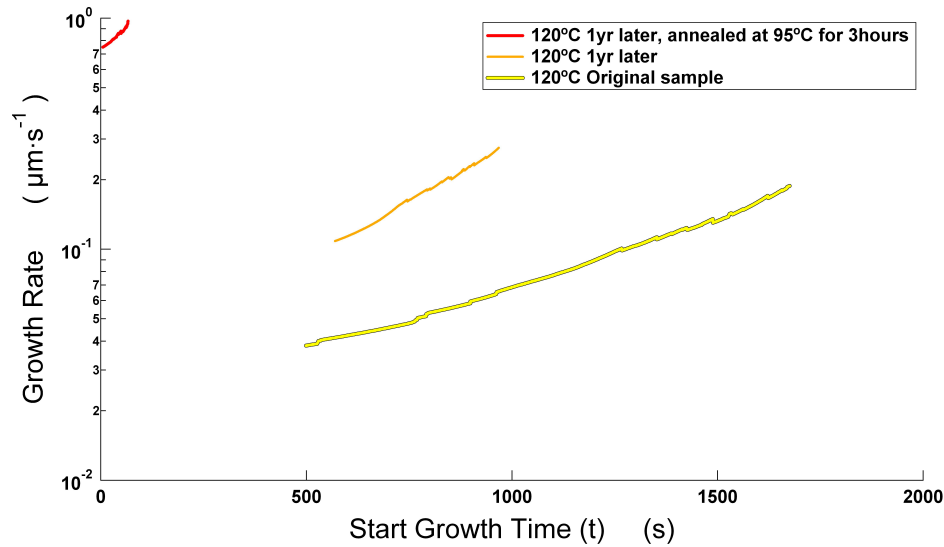


Figure 6.17: Growth rate in $\mu\text{m}\cdot\text{s}^{-1}$ against time in (s) for sample Ga11.79Sb88.21 at 120°C , again at 1 year later, and the growth rate at 120°C of a sample that has been pre annealed for three hours at 95°C . Time $t=0$ corresponds when growth at 120°C starts as observed with the eye.

been pre annealed at 95°C for three hours this is not the case since crystals were already present when the sample was reheated to 120°C . As soon as the temperature was increased again for the pre annealed sample, the crystals started to grow. At no point did it take time for the crystals to start growing. This means the crystallisation process has no inherent incubation time.

The pre annealed sample shows growth rates larger than three times the maximum growth rate normally measured at 120°C . If the measured growth rates for the pre annealed sample were in the range of all growth rates measured during the crystallisation process of the other two samples, this might have been attributed to the fact that the sample was halfway through the crystallisation process, but the fact that the pre annealed sample shows much higher growth rates than the maximum growth rate measured during normal crystallisation process at 120°C , irrefutably shows that the increased growth rate is caused by a relaxation effect.

The growth rate measurements shown in Figure 6.17 were measured at the same temperature, but have different slopes. This indicates that although both time and temperature have an influence on relaxation, they are not freely interchangeable and it is probably nonholonomic. This means pre annealing at 95°C , not only changes the measured growth rate when the sample is reheated to 120°C , but also changes the rate at which the growth rate changes in time once 120°C has been reached.

When the growth rates measured at 120°C one year after the original measurement and the growth rates of the original measurement done at

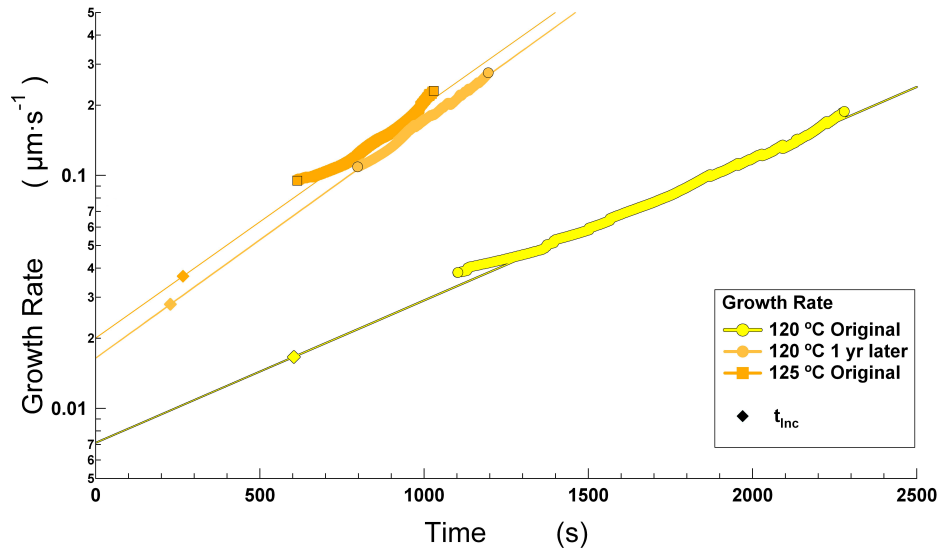


Figure 6.18: Growth rate in $\mu\text{m}\cdot\text{s}^{-1}$ against time in (s) for sample Ga11.79Sb88.21 at 120°C and 125°C , again at 1 year later at 120°C , with their corresponding exponential fits. Incubation time t_{Inc} is indicated on the fit with a rhombus shape.

120°C are extrapolated, they appear to almost meet each other at time $t=0$ in Figure 6.17. Since time $t=0$ equals t_{Inc} for these to samples in Figure 6.17, one might be tempted to state that the theoretical growth rate at the moment the first reaches 120°C , the actual time $t=0$, has decreased over the course of a year. This statement is incorrect, because not only has the slope of the measured growth rates changed over the course of a year, the incubation time t_{Inc} has changed as well. When the theoretical growth rate at time $t=0$ is retrieved correctly as done in Figure 6.18, one can clearly see that the theoretical growth rate at time $t=0$ has increased over the course of a year. The fact the potential growth rate at time $t=0$ has increased over the course of a year corroborates not only that relaxation is the cause behind the increase in growth rate, but also that extrapolating an exponential fit through the data to find the original material properties before relaxation occurs, the material properties at time $t=0$, is a valid approach.

The information presented in Figures 6.15, 6.17 and 6.18 shed a new light on the conclusions presented in the previous chapter. In the previous chapter it was stated on the bases of Figure 5.5 that in all probability Gallium did not have a major influence on the formed crystal structure and acted more as a growth inhibitor, while Germanium was a vital part of the crystallisation process. This was done on the bases that there seemed to be no a major change in the growth activation energy E_G for different Gallium concentrations.

There seemed to be no relaxation effects for sample with composition

$\text{Ga}_{10.42}\text{Sb}_{89.58}$ and therefore the derived value for the growth activation energy, $E_G = 1.21\text{eV}$ presented in Figures 5.5 and 6.15, remains accurate. In contrast, if the approach of extrapolating an exponential fit through the measured data to find the material properties at time $t=0$ is valid, then value of the growth activation energy E_G for the as deposited layer for sample $\text{Ga}_{11.79}\text{Sb}_{88.21}$ is not $E_G = 1.16\text{eV}$, see Figure 5.5, but $E_G = 2.29\text{eV}$, see Figure 6.15. This means that any conclusions or hypothesis made in chapter 5 should be re-evaluated. An increase in Gallium concentration in the deposited layer, might actually increase the growth activation energy E_G in the same way that Germanium does, but is simply unobserved due to the relaxation effect.

A second observation that came from the relaxation experiment is that there seems to be no inherent incubation time. This important when applying JMAK theory on the crystallisation process. The Avrami equation does not take into account inherent incubation time. This could, for instance, be a sample with crystals that is heated to 120°C and it takes a certain amount of time before the crystals start to grow. No such observation has been made, so the possibility that this effect interferes when trying to fit a modified Avrami equation for exponential growth can be discarded.

Although it has been shown that the best way of constructing an modified Avrami equation for the transformation process of the $\text{Ga}_{11.79}\text{Sb}_{88.21}$ is to consider growth rate as a exponential increasing function dependent on time, caused by a relaxation effect of the layer, the question remains if there are no heating effects at all. In the previous section it has been mentioned that for crystals with a small diameter or crystals that approach each other, the measured growth rate starts to deviate from the exponential fit. Although this effect was expected because of software inaccuracies, it could not be completely explained. An hypothesis might be that heat is indeed produced, but is quickly dissipated through the layer. For crystals of intermediate size with sufficient room between them this excess heat can be dissipated in both the direction of the amorphous layer and back into the crystal layer. For small crystals it might be more difficult to dissipate the heat in back to centre of the crystal, while crystals that approach each other might be influenced by each others heat dissipation. The study of this potential effect is beyond the scope of this report and therefore not further pursued.

6.3 Avrami Theory including relaxation effects

In his paper, Avrami gave a very general description of the transformation process from one solid state to another. He emphasized that his model was a generalisation of many other models including a transformation model that is not based on predetermined nuclei ([10] p1104-p1105), nucleation

probability n that is dependent on time ([10] p1107), a wide variation of random distributions for the predetermined nuclei ([11] p216), among other things. He explicitly derives equations for the case of growth rate constant in time, but his model is valid for any continuous time dependent growth rate function $G(t)$ ([10] p1109-p1110).

In the last section it was shown that growth rate could be described by an exponential function of the form:

$$G(t) = Ce^{a \cdot t} \quad (6.1)$$

where C is the theoretical growth rate for the sample at time $t=0$, or the growth rate at temperature T for the sample, would it not be affected by a relaxation effect, and a is a constant with dimension s^{-1} . The physical interpretation of a is unknown at this moment, for all practical purposes it can be viewed as the strength of the relaxation effect.

Equation 6.1 is used as a general description of how growth rate depends on time, following the same derivation steps as described in chapter 2 and in [11], the Avrami equation for the transformation process from amorphous to crystalline in the case of exponentially increasing growth rate $G(t)$ and constant nucleation rate n can be derived, and is found to be:

$$V = 1 - e^{-\left(\frac{\sigma C^2 N}{a^2}\right) \left(\left(\frac{-2a^2 e^{-nt}}{(a-n)(2a-n)} + 1\right) e^{2at}\right) \left(+ \frac{2ne^{at}}{(a-n)} - \frac{n}{(2a-n)}\right)}$$

$$\begin{aligned} \sigma &\approx \pi, & N &> 40 \text{ mm}^{-2}, & n &\approx 6 \cdot 10^{-5} \text{ s}^{-1} \\ C &\approx 2.2661 \cdot 10^{-4} \text{ } \mu\text{m/s}, & a &\approx 1.7452 \cdot 10^{-4}, \end{aligned} \quad (6.2)$$

where information regarding the approximations of N , n , and σ can be found in section 5.1.3 and the approximations for C , and a are based on the fits through the data shown in Figure 6.14, whose derived values can be found in Table 6.1.

To gain an insight in how well equation 6.2 is able to describe the transformation process from amorphous to crystalline, it will be fitted to the crystalline fraction V data obtained from the isothermal annealing experiment of sample $\text{Ga}_{11.79}\text{Sb}_{88.21}$ at 100°C . First, the only free variable will be N . In the second scenario both N , and C will be free variables, keeping the strength of the relaxation effect a fixed. The third scenario describes the case where the the exponential growth rate function $G(t)$ is unconstrained, thus N , C , and a are free variables. Then the effect keeping the growth rate

T (°C)	C ($\mu\text{m/s}$)	a
95°C	$1.2857 \cdot 10^{-4} \pm 2.41 \cdot 10^{-6}$	$1.6866 \cdot 10^{-4} \pm 6.42 \cdot 10^{-7}$
100°C	$2.2661 \cdot 10^{-4} \pm 2.40 \cdot 10^{-6}$	$1.7452 \cdot 10^{-4} \pm 4.31 \cdot 10^{-7}$
105°C	$1.4929 \cdot 10^{-4} \pm 1.51 \cdot 10^{-5}$	$3.0170 \cdot 10^{-4} \pm 6.37 \cdot 10^{-6}$
110°C	$1.2139 \cdot 10^{-3} \pm 2.23 \cdot 10^{-5}$	$4.4815 \cdot 10^{-4} \pm 2.25 \cdot 10^{-6}$
115°C	$3.1924 \cdot 10^{-3} \pm 5.29 \cdot 10^{-5}$	$6.9630 \cdot 10^{-4} \pm 3.80 \cdot 10^{-6}$
120°C	$7.1232 \cdot 10^{-3} \pm 1.29 \cdot 10^{-4}$	$1.4065 \cdot 10^{-3} \pm 9.21 \cdot 10^{-6}$
125°C	$2.0045 \cdot 10^{-2} \pm 8.57 \cdot 10^{-4}$	$2.2990 \cdot 10^{-3} \pm 4.71 \cdot 10^{-5}$
130°C	$5.5469 \cdot 10^{-2} \pm 4.55 \cdot 10^{-3}$	$4.7967 \cdot 10^{-3} \pm 2.77 \cdot 10^{-4}$
135°C	$1.3799 \cdot 10^{-1} \pm 4.13 \cdot 10^{-3}$	$1.0621 \cdot 10^{-2} \pm 2.34 \cdot 10^{-4}$

Table 6.1: Variable values of a standard exponential function $Ce^{a \cdot t}$ fitted to the observed change in growth rate G during isothermal annealing experiments of sample $\text{Ga}_{11.79}\text{Sb}_{81.21}$. Fit coefficient confidence intervals are at 99.73% confidence level, see Figure 6.14.

$G(t)$ constrained, but both N , and nucleation probability n are free variables. In the last two scenario's N , C , a , and n are all free variables, to find a perfect fit to the acquired data. It will be shown that this is only possible if the retrieved fit variables are in conflict with the retrieved fit variables from the growth rate measurements described in the last section and shown in Figure 6.14. This approach first tests the initial strength of the model, then when an even better fit is found by increasing the amount of variables, it is possible to check if the difference between the derived variable values from the fit and the derived variable values from the measurement can be attributed to a measurement error, or that the retrieved variable values of the model no longer represent reality.

Again there are many solutions that fit the measured data using equation 6.2. However, choosing the approximations mentioned in the last paragraph as the starting values results in a stable convergence.

The derived fit variable for the different scenarios mentioned above can be found in Table 6.2 and the resulting fits are plotted in Figure 6.19.

First the accuracy of the model is tested, by fixing all variables to be the approximations derived earlier in this report, only N is a variable. It stands to reason that N should be above zero and less than infinity, so those are used as boundary conditions. This leads to fit that is much more accurate than the fits described in section 5.1.3, where the coefficient of determination R^2 equals 0.9829. The derived value of N equals 31.24 mm^{-2} ,

Physical Quantity	Starting Value	Lower Bound	Upper Bound	Fit Value	Confidence Level 95%
Best fit based on estimations					R ² 0.9829
N (mm ⁻²)	10	0	Inf	31.24	(30.87, 31.6)
Starting growth rate C as free variable					R ² 0.9844
N (mm ⁻²)	52	40	10 ⁴	50.36	(39.9, 60.83)
C (μm/s)	$2.27 \cdot 10^{-4}$	$1.29 \cdot 10^{-4}$	$1.21 \cdot 10^{-3}$	$1.832 \cdot 10^{-4}$	($1.634 \cdot 10^{-4}$, $2.03 \cdot 10^{-4}$)
Exponential increasing growth rate as a free variable					R ² 0.994
N (mm ⁻²)	50	40	10 ⁴	40	(fixed at bound)— at bound)
C (μm/s)	$2.27 \cdot 10^{-4}$	$1.29 \cdot 10^{-4}$	$1.21 \cdot 10^{-3}$	$1.29 \cdot 10^{-4}$	(fixed at bound)
a	$1.75 \cdot 10^{-4}$	$1.50 \cdot 10^{-4}$	$3.02 \cdot 10^{-4}$	$1.974 \cdot 10^{-4}$	($1.974 \cdot 10^{-4}$, $1.974 \cdot 10^{-4}$)
Nucleation probability n as a free variable					R ² 0.9862
N (mm ⁻²)	50	40	10 ⁴	42.59	(42.14, 43.05)
n (s ⁻¹)	$6 \cdot 10^{-5}$	$4 \cdot 10^{-5}$	$1.2 \cdot 10^{-4}$	$4 \cdot 10^{-5}$	(fixed at bound)
All physical quantities as a free variable: boundaries					R ² 0.9958
N (mm ⁻²)	60	40	10 ⁴	40	(fixed at bound)
C (μm/s)	$2.27 \cdot 10^{-4}$	$1.29 \cdot 10^{-4}$	$1.21 \cdot 10^{-3}$	$1.29 \cdot 10^{-4}$	(fixed at bound)
a	$1.75 \cdot 10^{-4}$	$1.50 \cdot 10^{-4}$	$3.02 \cdot 10^{-4}$	$2.033 \cdot 10^{-4}$	($2.032 \cdot 10^{-4}$, $2.035 \cdot 10^{-4}$)
n (s ⁻¹)	$6 \cdot 10^{-5}$	$4 \cdot 10^{-5}$	$1.2 \cdot 10^{-4}$	$4 \cdot 10^{-5}$	(fixed at bound)
All physical quantities as a free variable: best fit					R ² 0.9998
N (mm ⁻²)	1000	40	10 ⁴	286.6	(-6789, 7362)
C (μm/s)	$2.27 \cdot 10^{-4}$	$1.29 \cdot 10^{-5}$	$1.21 \cdot 10^{-3}$	$2.225 \cdot 10^{-5}$	($1.52 \cdot 10^{-4}$, $1.965 \cdot 10^{-4}$)
a	$1.75 \cdot 10^{-4}$	$1.50 \cdot 10^{-5}$	$3.02 \cdot 10^{-3}$	$2.378 \cdot 10^{-4}$	($1.61 \cdot 10^{-4}$, $3.146 \cdot 10^{-4}$)
n (s ⁻¹)	$6 \cdot 10^{-5}$	$4 \cdot 10^{-5}$	$1.2 \cdot 10^{-4}$	$4.24 \cdot 10^{-5}$	($-3.784 \cdot 10^{-4}$, $4.632 \cdot 10^{-4}$)

Table 6.2: Variable values derived from fitting the adjusted Avrami equation to the measured crystalline fraction V during isothermal annealing at 100°C of sample Ga_{11.79}Sb_{81.21}.

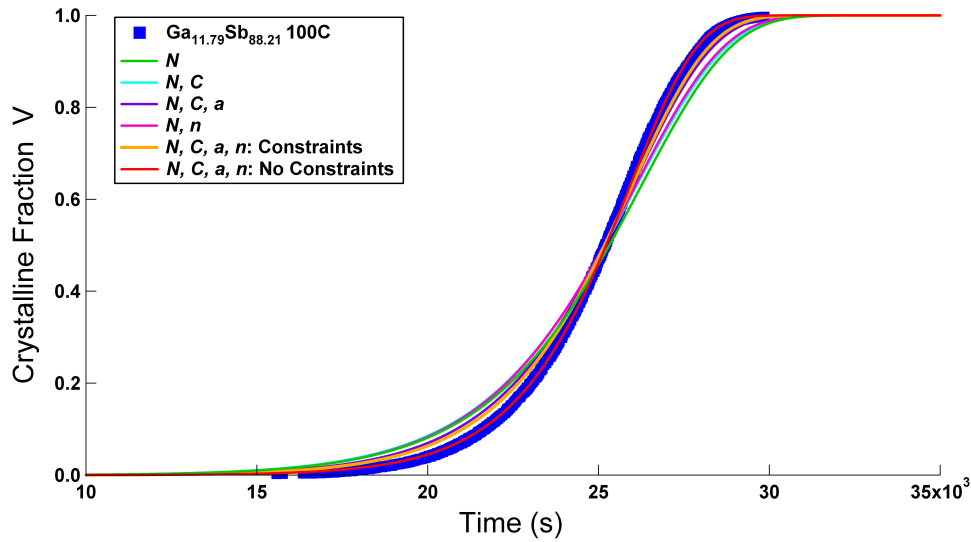


Figure 6.19: Fits using the adjusted Avrami equation, see Equation 6.2, to the measured crystalline fraction V during isothermal annealing at 100°C of sample $\text{Ga}_{11.79}\text{Sb}_{88.21}$. How many and which variables were free is indicated in the legend.

below the observed more than 40 crystals. Figure 6.20 shows a still of the crystallisation process for sample $\text{Ga}_{11.79}\text{Sb}_{88.21}$ at 135°C . Based on Figure 6.20, and the assumption that N does not depend on temperature it is possible to estimate that N should have a value in the order of 400 mm^{-2} .

The question that now needs to be answered is. If more variables are free, but with boundary conditions that are in acceptable limits based on measurements described earlier in this report, is it possible to retrieve a more accurate fit, with a derived value for N that lies more in the range of 400 mm^{-2} instead of 40 mm^{-2} .

First both N and C are free variables, where the boundary values for C are based on the derived values for C at 95°C and 110°C , see Table 6.1 and Figure 6.14. This does not lead to a significant improvement in the accuracy of the fit, as is to be expected when examining equation 6.2, but the retrieved value for N is greater than forty, see Table 6.2.

Systematically increasing the amount of free variables, always choosing boundary conditions on the basis of results shown in Figure 6.14, and Table 6.1 for C and a and Figure 5.8 for n , the accuracy of the fit increases, see Figure 6.19, but retrieved value for N is not significantly increased, see Table 6.2. Only when the boundary conditions are significantly increased is it possible to obtain a larger value for N , see Table 6.2, but this leads to a prediction for $G(t)$ that is conflict with the measurement of $G(t)$, see Figure 6.21.

When N is the only free variable, and all other variables are fixed based on the approximations mentioned earlier, the crystalline fraction V is first

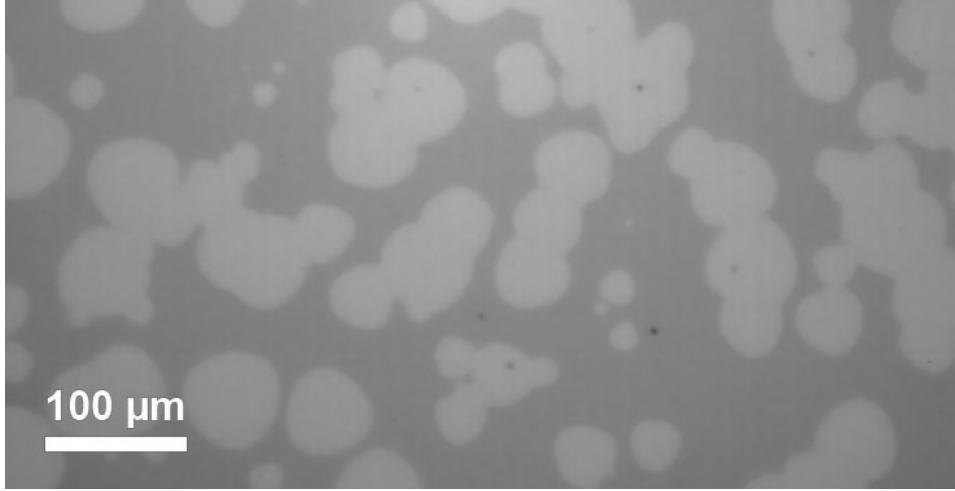


Figure 6.20: Still of the crystallisation process of sample $\text{Ga}_{11.79}\text{Sb}_{88.21}$ at 135°C . The approximate surface area shown is 0.25 mm^{-2} . Over ninety crystals are observed in Figure 6.20.

overestimated and then underestimated. One possibility to explain this is that nucleation probability n is not constant, but an increasing function of time $n(t)$.

A attempt to include the time dependence of n in the adjusted Avrami equation is made, based on the assumption that relaxation affects n in exactly the same manner as G . That is, $n(t)$ can be written as:

$$n(t) = Pe^{b \cdot t} \tag{6.3}$$

where P is the probability of nucleation of a single predetermined nuclei per unit time before any relaxation effect occurs, and b is a constant with dimension s^{-1} that describes the strength of the relaxation effect. This leads to an adjusted Avrami equation of the form:

$$V = 1 - e^{- \left(\left(\frac{\sigma C^2 N}{a^2} \right) \left(\left(\frac{-2a^2 e^{-Pe^{bt}t}}{(a - Pe^{bt})(2a - Pe^{bt})} + 1 \right) e^{2at} \right) \right) + \frac{2Pe^{bt}e^{at}}{(a - Pe^{bt})} - \frac{Pe^{bt}}{(2a - Pe^{bt})} \right)}$$

$$\begin{aligned} \sigma &\approx \pi, & N &> 40 \text{ mm}^{-2}, \\ C &\approx 2.2661 \cdot 10^{-4} \text{ } \mu\text{m/s}, & a &\approx 1.7452 \cdot 10^{-4}, \\ P &\approx ??? \text{ s}^{-1}, & b &\approx 1.7452 \cdot 10^{-4} \end{aligned} \tag{6.4}$$

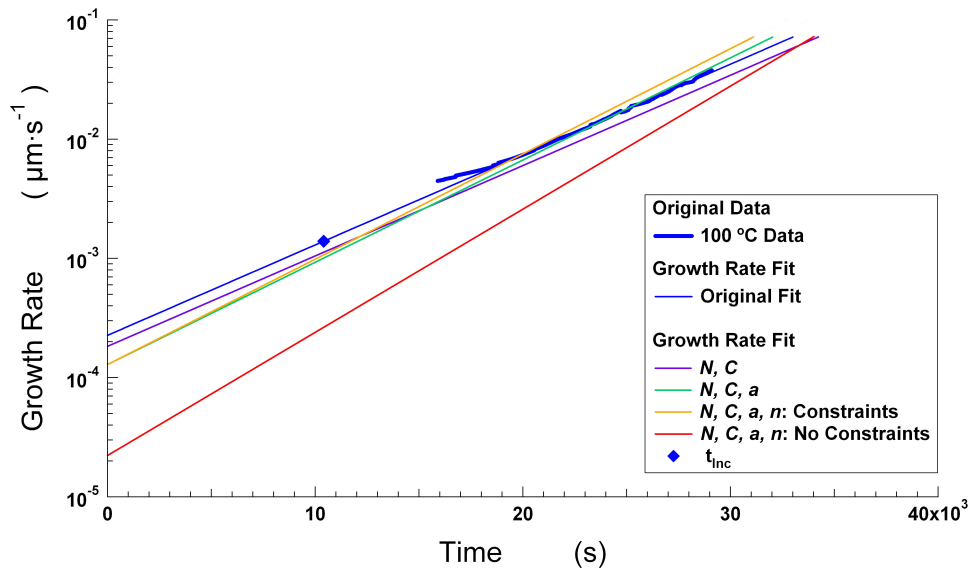


Figure 6.21: Predicted growth rate variation with time based on the fit variables, see Table 6.2, retrieved from the fits of the adjusted Avrami equation, see Equation 6.2, to the measured crystalline fraction V during isothermal annealing at 100°C of sample $\text{Ga}_{11.79}\text{Sb}_{81.21}$, see Figure 6.19. How many and which variables were free is indicated in the legend.

were the approximation value for b is based on the assumption that relaxation affects n in the same manner as G and the value for b is therefore equal to the derived value of a , see Table 6.1.

Of course equation 6.4 does not need to be valid, but even if it is, b need not to be equal to a . It is attempted to fit equation 6.4 to the acquired data of sample $\text{Ga}_{11.79}\text{Sb}_{88.21}$ at 100°C . Only N , P , and b , or only N , and P are free variables. Starting values and boundaries are chosen to represent nucleation that is independent on time. The starting value for N is 3000, to increase the chance of finding a stable fit with a value for N that is higher than forty, see Table 6.3.

The resultant fit describes the obtained data extremely well, the coefficient of determination R^2 is rounded to 1, indicating a perfect fit. To give some indication of error the sum of squared errors is shown in Table 6.3 as well.

When b is a free variable, it is possible to find some fits that have a higher value for N , but these are not as accurate as the retrieved fits shown in Table 6.3 and Figure 6.22. They are also less stable, in the sense that a slight variation in boundary conditions or starting values causes that model either not to converge or to converge to values shown in Table 6.3.

The retrieved value for b is almost equal to the retrieved value for a based on growth rate measurements, see Table 6.3 and 6.1. This provides

Physical Quantity	Starting Value	Lower Bound	Upper Bound	Fit Value	Confidence Level 95%
Relaxation effect $n \neq$ relaxation effect G					R ² : 1 SSE: $6.16 \cdot 10^{-3}$
N (mm ⁻²)	3000	-Inf	Inf	40.69	(40.16, 41.23)
P (s ⁻¹)	$6 \cdot 10^{-5}$	0	Inf	$4.74 \cdot 10^{-7}$	($4.607 \cdot 10^{-7}$, $4.873 \cdot 10^{-7}$)
b	0	-Inf	Inf	$1.783 \cdot 10^{-4}$	($1.764 \cdot 10^{-4}$, $1.801 \cdot 10^{-4}$)
Relaxation effect $n =$ relaxation effect G					R ² SSE: $6.233 \cdot 10^{-3}$
N (mm ⁻²)	3000	0	Inf	41.72	(41.54, 41.84)
P (s ⁻¹)	$6 \cdot 10^{-7}$	0	Inf	$5.008 \cdot 10^{-7}$	($4.976 \cdot 10^{-7}$, $5.04 \cdot 10^{-7}$)

Table 6.3: Variable values derived from fitting the adjusted Avrami equation including exponential increase of nucleation with time to the measured crystalline fraction V during isothermal annealing at 100°C of sample Ga_{11.79}Sb_{81.21}.

credibility to the notion that relaxation affects nucleation probability n in the same manner as growth rate G . When b is set equal to a , the only value of N that results in an accurate fit lies in a range around 40 mm⁻². The retrieved value for P lies two orders of magnitude lower than the retrieved value for n , in the same manner as the retrieved value for C lies two orders of magnitude lower than the retrieved value of G , see Tables 6.3 and 6.1, section 5.1.3, and Figures 5.1 and 6.14. This again lends credibility to the idea that relaxation affects nucleation in the same manner as it affects crystal growth.

The retrieved value for N is nearly equal to the amount of observed crystals, which could be translated as: every predetermined nucleus in the layer has been activated when the transformation process is complete. Based on Figure 6.20 N should not equal 40 mm⁻². One hypothesis that could explain this discrepancy is that the crystallisation mechanism is not based on predetermined nuclei, but on the spontaneous emergence of crystals in the amorphous layer. Avrami mentions that his model incorporates this way of nucleation as a special case ([10] p1104-p1105).

Any theoretical proof, or the introduction for experimental set-up, to show that this hypothesis based on one retrieved value for N , which was in turn based on the assumption that relaxation affect nucleation probability n in the same way as it affects G , is correct is beyond the scope of the report. At this moment it becomes increasingly difficult to improve our understanding of the kinetic properties of the Ga _{x} Sb_{100- x} samples, without

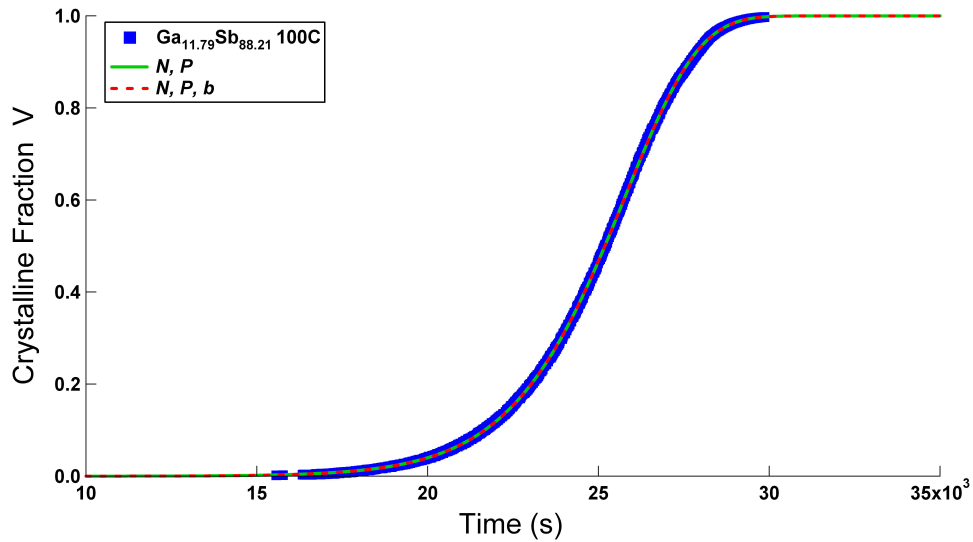


Figure 6.22: Fits using the adjusted Avrami equation including exponential change of nucleation probability n , see Equation 6.4, to the measured crystalline fraction V during isothermal annealing at 100°C of sample Ga_{11.79}Sb_{88.21}. How many and which variables were free is indicated in the legend.

further literature study or experiments. Therefore this moment will end our treatment of the observed exponential increase of growth rate in time and our attempts to test the validity of using JMAK as a way to describe the crystallisation process of the Ga _{x} Sb_{100- x} samples.

The only thing left to do is to use the findings presented in this chapter and discuss its implications on the findings regarding the isothermal annealing experiments presented in chapter 5 and the sample creation process described in chapter 4.

Chapter 7

Discussion

7.1 Sample preparation

In section 6.2 it was mentioned that relaxation was observed in sample $\text{Ga}_{11.79}\text{Sb}_{88.21}$, but not in sample $\text{Ga}_{10.42}\text{Sb}_{89.58}$. The main difference between these two samples lies in the speed with which they were deposited on the glass substrate. The layer of sample $\text{Ga}_{11.79}\text{Sb}_{88.21}$ was deposited at a rate of 1.50 nm/s and the layer on sample $\text{Ga}_{10.42}\text{Sb}_{89.58}$ was deposited at a rate of 0.14 nm/s, see Table 4.7. It is known that there is a tensile stress in the as deposited layer, see Figure 4.15. The layer shown in Figure 4.15 was deposited at a layer deposition rate in the order of 10nm/s. Tensile strength applied to the $\text{Ge}_x\text{Sb}_{100-x}$ samples analysed by Gert Eising affected the crystallisation kinetics of the material[22]. Therefore, a higher layer deposition rate might result in a higher tensile stress across the deposited layer. The observed relaxation effect might therefore be related to the reduction of this tensile stress due to thermal annealing. At any rate, a higher deposition rate will result in thin films deposited with a less equilibrated structure and therefore it can be expected that more relaxation (of the structure) is possible in these films.

Relaxation effects were not observed for the $\text{Ge}_x\text{Sb}_{100-x}$ samples, while they were created using magnetron sputtering. Magnetron sputtering is known to cause internal stresses in the as-deposited layer [23]. It is known that these stresses can be reduced by relaxing the amorphous layer by means of thermal annealing [24]. Thermal annealing had an adverse effect on the explosive crystallisation properties of sputter deposited GaSb films [5], thus layer relaxation has an adverse effect on the explosive crystallisation properties of sputter deposited GaSb films.

An underlying cause of these effects could be that layer relaxation causes the energy barrier between the amorphous phase and the crystalline phase to decrease, but that also reduces the Gibbs free energy difference between the amorphous and crystalline state. Thus undermining the underlying mecha-

nism for explosive crystallisation process [9]. Repeated switching of a phase-change material has shown to cause structural relaxation [25].

Therefore, if the goal of a research is to find a material that is suitable for as a non-volatile memory application it is advised to create sample at a slow deposition rate of 0.2 nm/s, but if the goal of the research is to induce explosive crystallisation a higher layer deposition rate including and above 1.5 nm/s is advised.

7.2 Annealing experiments and relaxation

In chapter 5 it was concluded that Germanium was a better stabilizer than Gallium and that the $\text{Ge}_x\text{Sb}_{100-x}$ had better properties to be used in of non-volatile memory applications. Increasing amounts of Germanium led to increasing growth rates, while this seemed not to be the case for the samples containing Gallium, see Figures 5.4 and 5.5. However, in section 6.2 Figure 6.15 gave rise to the hypothesis that increasing the amount of Gallium also causes an increasing growth rate for the as-deposited layer, but that this effect is not observed because of relaxation.

The difference in kinetic properties of the as-deposited layers, might therefore not be caused by underlying crystallisation mechanism, but by their creation method. If an increase in Germanium or Gallium causes an increase in tensile stress in the layer, but it is difficult to relax the Germanium layer. This would explain the observed difference in kinetic properties as well. In the search for materials that are useful in non-volatile memory applications it stands to reason that a layer needs to be as relaxed as possible, since repeated switching causes relaxation anyway, and therefore it has no purpose to get overly excited about the kinetic properties of a stressed layer. A definite conclusion whether Gallium or Germanium is a better stabilizer can only be made if the kinetic properties of the most relaxed state of both layers is found.

In this report it was assumed that the crystallisation mechanism relies on predetermined nuclei, but this might not be the case. Since it is known from literature, that growth activation energy and nucleation activation energy are linked [21], it stands to reason that it is useful to know the actual crystallisation mechanism. For example: a decrease in the difference between E_G and E_n , might cause an increase in device performance, since rate with which V goes from zero to one depends on both E_G and E_n . A proper understanding of the underlying crystallisation mechanism is necessary to determine whether this is possible or not.

7.3 TEM experiments for crystal structure analysis and layer excitation

Knowing the structure of the crystals formed in the different samples provides information whether stabilisation by Germanium or Gallium causes, inhibition of the growth of Antimony crystals or if they are an essential part of the crystal structure, which in turn provides information if the superior stability observed for the Germanium samples is stress induced or structural.

It might also be possible to use the electron beam as a way to get the amorphous layer to a higher energy state, by means of electronic excitation, thus increasing the Gibbs free energy difference between the amorphous state and the crystalline state, and in that way increase the probability to successfully cause explosive crystallisation. Although on the other hand it is known that the electron beam can also lead to relaxation of the material[26].

Chapter 8

Conclusions

8.1 Sample preparation

The creation of thick layers with uniform composition throughout their thickness is not possible using single target e-beam evaporation. With perfection of the evaporation technique it is possible to accurately predict sample composition on the basis of target composition and target weight. An observable relaxation effect is not desirable in the analyses of the isothermal crystallisation process. Using e-beam evaporation as a means of sample preparation for isothermal growth analyses is only advisable when the layer deposition rate is 0.2nm/s or lower and the layer is not very thick as to minimise the difference in composition between the top and the bottom of the layer. In the creation of samples for researching explosive crystallisation a high layer deposition rate is advisable.

8.2 Annealing experiments

Comparison between the $\text{Ge}_x\text{Sb}_{100-x}$ samples and the $\text{Ga}_x\text{Sb}_{100-x}$ samples showed that the $\text{Ge}_x\text{Sb}_{100-x}$ samples showed more stable amorphous phases for the same addition (At%) of Ge or Ga and therefore might possess superior properties for memory applications. The principle difference between the two being that E_G increases with increasing amount of Germanium for the $\text{Ge}_x\text{Sb}_{100-x}$ samples, while such a definite statement could not be made for the $\text{Ga}_x\text{Sb}_{100-x}$ samples, nor could the opposite statement be made that Gallium had no effect on E_G . It was not possible to describe the amorphous to crystalline transformation process of the $\text{Ga}_x\text{Sb}_{100-x}$ samples by standard Avrami equations. It was revealed that this was due to the fact that growth rate increased exponentially with time. This exponential increase in growth rate was caused by relaxation of the layer. Determination of the growth rate properties of the layer at time $t = 0$ before any relaxation had taken place, indicates that Gallium might influence the deposited layer in the same way

as Germanium, but that this effect is not observed due to relaxation. An adjusted Avrami equation was able to describe the crystallisation process to a much higher degree of accuracy, but indicated that relaxation also influenced nucleation probability. The assumption that nucleation is affected in the same manner as growth rate by nucleation led to a near perfect fit, but this assumption stills needs to be validated. Future research should focus on the question whether an increase in Germanium or Gallium leads to an increase in stress in the deposited layer, leading to a change in kinetic properties, since for memory applications, the kinetic properties of a relaxed layer are more interesting.

Acknowledgements

I would like to thank Bart for his continuous patience the during the creation of this report and his support in helping me understand JMAK-theory, numerous theoretical problems, and physical principles underlying the crystallisation process of an amorphous phase-change layer. I would like to thank Gert Eising for patiently explaining to me multiple times how to operate the experimental set-up, how the analysis software works, for creating a usable line profile program that allowed for the analyses of the exponential increasing growth rate and at times prioritising the proofreading of this report above the finalisation of his own thesis. I would like to thank Gert ten Brink for helping me retrieve SEM pictures and composition data using EDX at the first moment available, even when I was stubborn and wanted to double check the same sample again. I would like to thank Johan Holstein for teaching me how to operate the Varian e-beam evaporator and allowing me free use of the machine without supervision, whenever I wanted. I would like to acknowledge the support from Nanolab, the Zernike Institute for Advanced Materials (ZIAM), and Materials to Innovate (M2I), who made the realisation of research possible.

The finalisation of this report marks the end of my Master and study period here in Groningen and I would like to thank my parents, family, and friends for their continuous support. A word of appreciation also goes to my study association T.F.V. 'Professor Francken', which has probably contributed to the extension of the duration of my study period, but were it not for the support of her members in difficult times this thesis might have never seen the light of day.

Bibliography

- [1] M. Wuttig and N. Yamada, “Phase-change materials for removable data storage,” *Nature Materials*, vol. 6, pp. 824–833, november 2007. doi:10.1038/nmat2077.
- [2] A. Olemskoi, A. Khomenko, and V. Koverda, “Explosive crystallization mechanism of ultradispersive amorphous films,” *Physica A*, vol. 284, pp. 79–96, 22 December 1999. doi:10.1016/S0378-4371(00)00180-1.
- [3] S. Roaux, “Phase change materials,” *Annual Review of Materials Research*, vol. 39, pp. 25–47, 2009. doi:10.1146/annurev-matsci-082908-145405.
- [4] C. W. Jr. and J. Poole, “Explosive crystallization in gallium-doped amorphous germanium,” *Materials Letters*, vol. 4, no. 5 6 7, pp. 268–271, July 1986. doi:10.1016/0167-577X(86)90021-2.
- [5] C. Wickersham, G. Bajor, and J. Greene, “Impulse stimulated ”explosive” crystallization of sputter deposited amorphous (In,Ga)Sb films,” *Solid State Communications*, vol. 27, pp. 17–20, 1978. doi:10.1016/0038-1098(78)91041-4.
- [6] R. Koba and C. Wickersham, “Temperature and thickness effects on the explosive crystallization of amorphous germanium films,” *Applied Physics Letters*, vol. 40, no. 8, pp. 672–675, 1982. doi:+10.1063/1.93223.
- [7] C. Wickersham, G. Bajor, and J. Greene, “Optical information storage using explosive crystallization in amorphous films,” *Journal of Vacuum Science & Technology A*, vol. 1, no. 4, pp. 1857–1860, 1983. doi:10.1116/1.572228.
- [8] K. Connors, *Chemical Kinetics*. VCH Publishers, 1990.
- [9] D. Porter and K. Easterling, eds., *Phase Transformations in Metals and Alloys*. 6000 Broken Sound Parkway NW, Suite 300, Boca Raton: CRC Press, 2004.

- [10] M. Avrami, "Kinetics of Phase Change. I: General Theory," *Journal of Chemical Physics*, vol. 7, pp. 1103–1112, December, 1939. doi: 10.1063/1.1750380. doi: 10.1063/1.1750380.
- [11] M. Avrami, "Kinetics of Phase Change. II: Transformation-Time Relations for Random Distribution of Nuclei," *Journal of Chemical Physics*, vol. 8, pp. 212–224, February, 1940. doi: 10.1063/1.1750631. doi: 10.1063/1.1750631.
- [12] J. V. Naidig and J. N. Chuvashov, "Wettability and contact interaction of gallium-containing melts with non-metallic solids," *Journal of Material Science*, vol. 18, pp. 2071–2080, 1983.
- [13] R. Honig, "Vapor pressure data for the more common elements," *RCA Review*, vol. 18, pp. 195–204, 1957.
- [14] I. Greenfield and R. Smith, "Gallium antimony system," *Journal of Metals*, vol. 203, pp. 351–353, February, 1955.
- [15] T. Dekorsy, R. Taubert, F. Hudert, A. Bartels, A. Habenicht, F. Merkt, P. Leiderer, K. Kohler, J. Schmitz, and J. Wagner, "Coherent acoustic phonons in nanostructures (invited speaker, subscriber archive copy)," *Proceedings of SPIE*, vol. 6892, pp. 68920E1–68920E8, 2008. doi:10.1117/12.760395.
- [16] R. Levine and B. Wajdyk, *Standard operating procedures for the electron beam evaporator*. Center for nanoscale science and engineering.
- [17] INFICON, "Density and acoustic impedance Z values," Jan 2013.
- [18] J. L. Oosthoek, B. J. Kooi, J. T. D. Hosson, R. A. Wolters, D. J. Gravesteijn, and K. Attenborough, "Growth rate analysis through automated tem image analysis: Crystallisation studies of doped sbte phase-change thin films," *Microscopy and Microanalysis*, vol. 16, pp. 291–299, 2010. doi:10.1017/S1431927610000176.
- [19] D. Muller, "Scanning electron microscopy," August 2013.
- [20] W. Martienssen and H. Warlimont, eds., *Springer Handbook of Condensed Matter and Materials Data*. Heidelberg: Springer, 2005.
- [21] G. Ruitenbergh, A. Petford-Long, and R. Doole, "Determination of the isothermal nucleation and growth parameters for the crystallization of thin $\text{Ge}_2\text{Sb}_2\text{Te}_5$ films," *Journal of Applied Physics*, vol. 92, no. 6, pp. 3116–3121, July 2002. Doi:10.1063/1.1503166.
- [22] G. Eising, A. Pauza, and K. B.J., "Stress-induced crystallization of ge-doped sb phase-change thin films," *Crystal Growth Des.*, vol. 13, no. 1, pp. 220–225, 2013. DOI:10.1021/cg3013848.

- [23] H. Windischman, “Intrinsic stress in sputter-deposited thin films,” *Critical Reviews in Solid State and Materials Sciences*, vol. 17, no. 6, pp. 547–596, 1992. DOI:10.1080/10408439208244586.
- [24] I. Ozen and M. Gulgun, “Residual stress relaxation and microstructure in ZnO thin films,” *Advances in Science and Technology*, vol. 45, pp. 1316–1321, 2006.
- [25] M. R. Society, “Symposium r: Phase-change materials for memory and reconfigurable electronics applications,” July 2013.
- [26] C. Afonso, J. Solis, K. Amanda, Petford-long, and R. Doole, “In situ studies on the crystallization kinetics in Ge-Sb films,” *Journal of Applied Physics*, vol. 77, pp. 607–613, 1994.